

**AUTOMATED SINGLE-CELL ELECTROPORATION AND  
SUBCORTICAL WHOLE-CELL RECORDING IN VIVO**

A Dissertation  
Presented to  
The Academic Faculty

by

William Andrew Stoy

In Partial Fulfillment  
of the Requirements for the Degree  
Doctor of Philosophy in Biomedical Engineering

Georgia Institute of Technology  
Emory University  
May 2019

**COPYRIGHT © 2019 BY WILLIAM STOY**

# **AUTOMATED SINGLE-CELL ELECTROPORATION AND SUBCORTICAL WHOLE-CELL RECORDING IN VIVO**

Approved by:

Dr. Craig R. Forest, Advisor  
George W. Woodruff School of  
Mechanical Engineering  
*Georgia Institute of Technology*

Dr. Jun Ueda  
George W. Woodruff School of  
Mechanical Engineering  
*Georgia Institute of Technology*

Dr. Garrett B. Stanley  
Coulter Department of Biomedical  
Engineering  
*Georgia Institute of Technology*

Dr. Albert Lee  
Janelia Research Campus  
*Howard Hughes Medical Institute*

Dr. Todd Sulchek  
George W. Woodruff School of  
Mechanical Engineering  
*Georgia Institute of Technology*

Date Approved: December 3, 2018

## ACKNOWLEDGEMENTS

First, I would like to thank my advisor, Craig, who has set the initial conditions for my success in the Precision Biosystems Lab from our very first phone call. The excitement, entrepreneurial spirit, and engineering rigor that I sensed in our first meeting was present throughout my tenure in the lab. I have grown as a scientist and engineer with your guidance and have learned to focus my efforts towards important and challenging goals.

To my committee members, Garrett Stanley, Todd Sulchek, Jun Ueda, and Albert Lee, thank you for the insightful discussions and guidance- it is greatly appreciated.

Thank you to all of the members of the Precision Biosystems Lab, past present and future! Special thanks to Chris Phaneuf, Mel Li, Suhasa Kodandaramaiah, Greg Holst, Caitlin Austin, Tim Li, and Corey Landry. You all are wonderful friends and talented engineers and I look forward to collaborating and hanging out with you in the future. An extra special thanks goes out to Bo Yang, who helped me with surgical preparation, without your help these experiments would not have been possible. Special thanks to my fellow graduate students, Jiu Jitsu practitioners, and friends, Colby Lewallen and Mighten Yip. Whether we're on the mats, at a competition, in the lab, or just hanging out, you have supported me through thick and thin. Another special thank you goes to my roommate, partner-in-crime, collaborator, and true friend, Ilya Kolb. As you said, we have had too many adventures to enumerate, but I can say that I count among the best moments of my life our late nights spent talking politics, science, and solving existential mysteries.

To my friends, Peter Borden, Dwight Chambers, and Alex Ortiz, thank you for all of the late nights watching *The Expanse*, playing board games, and the late nights over beer talking about careers, data, and quantum entanglement.

I would also like to thank my Jiu-Jitsu coach, Sam Joseph for teaching me mental toughness, the interplay between tactics and technique, and the confidence to hone my skills every day. For me, Jiu-Jitsu has been a thrilling journey and a metaphor for the PhD itself. Each move can be studied, improved, and strung together with other moves into a chain in an infinitely customizable way. You can spend a lifetime learning the science of the brain and you can spend a lifetime learning on the mats. I intend to do both.

A big thank you to my undergraduate research collaborators, Ali Kight, Sophia Switzer, Erin Rousseau, Daughtry St. John, and Amanda Felouzis. You have all contributed greatly to both my research and to the culture of the lab. I hope that your experience working in the Precision Biosystems Lab has inspired you to pursue research or has given you new tools to succeed at whatever you go on to do in life.

I also would not be where I am today without the love and support of Laura Mast. She has taught me to focus on gratitude every day, which, more than anything, has buoyed my spirits when times are dark. I am a better person for having met you and I am grateful to you every day for your love and support. Thank you.

Finally, the completion of a Doctor of Philosophy degree represents not just the hard work and effort that have gone into the study of project at hand, but the encouragement, support, and preparation in countless moments that have come before. In this respect, I would like to thank my parents, Gail and Steve Stoy and my brother David Stoy for their unwavering support. Mom and Dad, you have guided my curiosity from Day 1 and I would not be the man I am today without the lessons that you taught me and opportunities you provided for me. Thank you.



# TABLE OF CONTENTS

<b>ACKNOWLEDGEMENTS</b>	<b>iii</b>
<b>LIST OF TABLES</b>	<b>vii</b>
<b>LIST OF FIGURES</b>	<b>viii</b>
<b>LIST OF SYMBOLS AND ABBREVIATIONS</b>	<b>xv</b>
<b>SUMMARY</b>	<b>xvi</b>
<b>CHAPTER 1. Introduction</b>	<b>1</b>
1.1 Motivation	1
1.2 Overview of Electrophysiological Methods	4
1.2.1 Patch clamp	4
1.2.2 Scanning Ion Conductance Microscopy	7
1.3 Project Motivation	7
1.4 Assessment of the likelihood of project success	8
1.5 Literature review of <i>in vivo</i> and <i>in vitro</i> patch clamp electrophysiology	11
1.6 Engineering design by methodological comparison	13
1.6.1 Quality metrics	14
1.6.2 Methods comparison	15
1.7 Automation	17
<b>CHAPTER 2. Automated Extracellular Patch Recording and Delivery of Genetic Material Via Electroporation</b>	<b>20</b>
2.1 Introduction	20
2.2 Methods	22
2.2.1 Animals	22
2.2.2 Hardware	23
2.2.3 In vitro testing	24
2.3 In vivo testing	27
2.3.1 Surgical preparation	27
2.3.2 Data analysis	33
2.4 Results	33
2.4.1 In vitro electrophysiology and electroporation	33
2.4.2 In vivo electrophysiology and morphology	35
2.5 Discussion	36
<b>CHAPTER 3. Robotic Navigation to Subcortical Neural Tissue for Intracellular Electrophysiology in vivo</b>	<b>41</b>
3.1 Introduction	41
3.2 Methods	44
3.2.1 Acute in vivo and in vitro preparation	44
3.2.2 Pipette fabrication	44
3.2.3 Electrophysiology	45
3.2.4 Blood vessel penetration	46

3.2.5	Scanning Ion Conductance Microscopy in vitro	47
3.2.6	Regional pipette localization in vivo	48
<b>3.3</b>	<b>Results</b>	<b>52</b>
3.3.1	RPL using linear trajectory	52
3.3.2	Observations of obstacles	54
3.3.3	Selection of navigation parameters	56
3.3.4	RPL using robotic navigation	57
<b>3.4</b>	<b>Discussion</b>	<b>61</b>
<b>CHAPTER 4. Feedforward Synchronization of Pipette Tip to Membrane Motion in vivo</b>		<b>67</b>
<b>4.1</b>	<b>Introduction</b>	<b>67</b>
<b>4.2</b>	<b>Methods</b>	<b>70</b>
4.2.1	Acute in vivo preparation	70
4.2.2	HEK293T cell preparation	71
4.2.3	Hardware and setup	71
4.2.4	Cardiac and respiratory physiological recordings	73
4.2.5	Patch clamp system	73
4.2.6	Software	75
4.2.7	Measurement of in vitro relationship between gigaseal yield and pipette-membrane distance	80
4.2.8	Application of high yield autpatching techniques to an investigation of the thalamocortical pathway	81
<b>4.3</b>	<b>Results</b>	<b>85</b>
4.3.1	Effect of pipette-membrane distance on gigasealing yield in vitro	85
4.3.2	Synchronization of pipette-membrane distance	87
4.3.3	Effect of thalamic synchrony and sensory background on barrel cortex neuronal activity	92
<b>4.4</b>	<b>Discussion</b>	<b>99</b>
<b>CHAPTER 5. Discussion</b>		<b>105</b>
<b>5.1</b>	<b>Major contributions</b>	<b>106</b>
<b>5.2</b>	<b>Future work</b>	<b>108</b>
<b>APPENDIX A.</b>		<b>111</b>
<b>A.1</b>	<b>Effect of pipette angle on clogging</b>	<b>111</b>
<b>A.2</b>	<b>Improvement of <i>in vitro</i> patch clamp yield</b>	<b>114</b>
<b>A.3</b>	<b>Improvements to pipette cleaning methods</b>	<b>116</b>
<b>A.4</b>	<b>Estimation of the impulse response with the least-squares method</b>	<b>118</b>
<b>A.5</b>	<b>On the use of conscious creatures for biomedical research</b>	<b>119</b>
<b>REFERENCES</b>		<b>122</b>

## LIST OF TABLES

Table 1	Comparison of <i>in vivo</i> and <i>in vitro</i> whole-cell patch clamping methods	15
Table 2	Results of 5 whisker responsive whole-cells recorded in the mouse barrel cortex. Whisker and optical stimulation were performed with various conditions listed in the column headers. In all cells, the peak of the subthreshold response to the punctate whisker stimulus (“feature”) was delayed when the feature was embedded in a noise background, also known as an adapting stimulus. Additionally, as a result of the noise background, the amplitude of the response and the width of the response (here, the full-width-at-half-max (FWHM)), increased (except in Cell 5). Notably, cells that had presynaptic thalamocortical inputs that were responsive to optogenetic stimulation did not exhibit a significant shift in the time-to-peak when the light pulse was embedded in a noise background. Similarly, the width of the subthreshold response was not significantly different in either case.	95
Table 3	Comparison of electrode-based motion compensation methods. Note: total computation time in Michale Fee’s work was determined by extrapolating from results in the text. The cardiac FIR filter is computed and then the respiratory FIR filter is computed. Each computation requires 2-4 seconds and is iteratively updated at least once, sometimes up to 3 times. This results in a total recording / computation time of 8-24 seconds.	101
Table 4	Enumeration of debris sources for intracellular electrodes	112

## LIST OF FIGURES

Figure 1	Schematic of proposed dual-patch recording in the thalamus and cortex that motivated the methodological improvements in this work. Figure adapted from (Diamond, von Heimendahl, Knutsen, Kleinfeld, & Ahissar, 2008)	8
Figure 2	Whole-cell recordings are desirable but difficult to perform below the cortex <i>in vivo</i> . A total of 148 papers that performed the whole-cell technique <i>in vivo</i> and <i>in vitro</i> in mice and rats were analyzed to determine the yield of whole-cell recordings as a function of depth. Reports of whole-cell recordings were significantly rarer below 3mm from the pial surface (5% of all whole cell recordings). However, in brain slices, where pipettes do not have to travel through millimeters of tissue do not show a strong preference for physiological superficial tissue.	12
Figure 3	In vitro dual patch recordings to confirm electrophysiology and morphology of single cells can be recovered using cell-attached pipettes. Red trace: patch pipette in current clamp mode. Current was injected to bring the membrane to threshold and fire action potentials. Blue trace: the action potentials were recorded on the cell-attached patch pipette. Following the electrophysiological recording, slight positive pressure was applied to the cell-attached patch pipette and then current was injected via the current-clamp head stage (10x 20ms pulses at -20 nA).	26
Figure 4	Graphical User Interface (GUI) of the automated electroporator program with example recordings. GUI includes controls for the user to override aspects of the automated operation, as well as an experiment log that is saved to disk for future processing, and a resistance monitor to inspect the progress of the neuron hunting stage. Stimulation and identification of nearby neurons is performed manually. The user manually scales and applies brief current pulses to elicit action potentials in current clamp mode using the Multiclamp Commander control panel. An example of this process is seen above. The initial current injection of 50 nA for 20 ms did not elicit action potentials, but the second current injection shown here at 150 nA did elicit action potentials, marked with arrows.	30
Figure 5	Results of log file data from autoelectroporator experiments (n=26). A) Neuron hunting distance (mean = 124 $\mu$ m). B) Cleft resistance calculated after a 'hit' was detected during neuron hunting. Cleft resistance was calculated as the 'hit' resistance $R_{hit}$ subtracted from the resistance when the pipette was switched to atmospheric pressure, $R_{atm}$ (M $\Omega$ ) Shaded region indicates resistances less than 0 M $\Omega$ , indicative of pipette clogs, which were rejected (n=27). Rejected pipettes were retracted to the surface of the brain. C) Recording times following cell-attached patch formation. Red boxes recordings where visual stimulus was presented (n=10)	36

- Figure 6 Automated electroporation results. A-C: The system was used to identify and classify neurons in the mouse visual cortex (V1). In this case, the cell was encountered 598  $\mu\text{m}$  below the pial surface, visual drifting gratings were presented, and EGFP plasmids were delivered via electroporation. A) The timeline of events. First, the cell was stimulated with increasing current injection pulses until action potentials were detected. Then visual stimulus was triggered and delivered for approximately 12 minutes. Finally, the cell was electroporated using the Axoporation via the custom headstage switch described in 2.3.1.4 (red trace is current injection). B) Orientation tuning plot for the recorded neuron. The cell is maximally responsive at  $225^\circ$ . C) EGFP fluorescence recovered following a 4-day recovery period. D) Another example neuron recorded, electroporated, and imaged by the author. E) EGFP fluorescence from a recorded neuron with background DAPI staining (blue) to test for cell health following a 4-day recovery period. F) DAPI stain of distal region from recording site. No chronic damage or necrosis is observed by the operations of the automated electroporator. Scale bars: 100  $\mu\text{m}$ . Data in A-C and E,F were collected by collaborator Ben Ouellette using the software and hardware designed by the author. 39
- Figure 7 Comparison of pipettes used for thalamic patching (top) with conventional cortical patch clamp pipettes (bottom) 45
- Figure 8 Lateral navigation around obstructions prevents persistent pipette resistance increase caused by penetration of blood vessels *in vitro*. A) Resistance trace as a function of distance as a pipette pierces a blood vessel under high positive pressure. A residual resistance increase of 3.7 M $\Omega$  remains after the vessel is punctured. B) IR DIC images showing the pipette encountering and deforming the blood vessel (scale bar, 50  $\mu\text{m}$ ). C) Schematic of Scanning Ion Conductance Microscopy (SICM) mapping of a blood vessel proceeds from a central point. Samples are collected randomly from a grid area 20 x 20  $\mu\text{m}$  at 2  $\mu\text{m}$  resolution D) The entire blood vessel and surrounding milieu is shown under IR DIC (scale bar, 20  $\mu\text{m}$ ) E) Resistances mapped as a function of grid position, clearly showing increased resistance when the pipette is above the blood vessel (scale bar, 10  $\mu\text{m}$ , 2x interpolation) 47
- Figure 9 Robotic navigation algorithm for avoiding blood vessels during regional pipette localization *in vivo*. A) Schematic showing vascular avoidance preparation. Brain outline from the Allen Mouse Brain Atlas (Lein et al., 2007). B) Visual algorithm of vascular avoidance [1] Obstruction (here, a blood vessel) is detected by an increase in pipette resistance. [2] The pipette is retracted to z-dodge, [3] moved laterally, and [4] advanced to the original z-obstruction. If the difference in resistance at z-obstruction and the resistance at z-dodge is < 200 k $\Omega$ , [5] the pipette is advanced through z-obstruction and [6] the pipette is moved back to the original x and y axis. C) The pipette is navigated around a blood vessel with sequential steps sampling from a spiral pattern. Blood vessel in A and B shown in isometric 49

view. Blood vessel in C shown in top view (top) and cross section (bottom).

- Figure 10 Increased yield of RPL during whole-cell patching *in vivo* with robotic navigation. In vivo whole-cell recording is a serial process consisting of Regional Pipette localization, Neuron Hunting, Gigaseal Formation, and Break-In. Whole-cell recording yield (Total) is a linear product of previous success rates. During traditional, linear localization, cortical (top row) and thalamic pipettes (middle row) are clogged in 1/5 insertions and 3/4 insertions respectively, preventing further steps. Gray box indicates procedures presented in this study. The percentage of pipettes that successfully performed regional pipette localization increased from 25% to 82% and total whole-cell yield increased from 1% to 10% when robotic navigation was performed. (top row data reproduced from Kodandaramaiah et al., 2012) 52
- Figure 11 Pipette tip resistance increases during regional pipette localization *in vivo* due to accrued debris, preventing whole cell recordings. Robotic navigation prevents this debris from accruing. A) Recordings of change in pipette resistance during regional pipette localization reveal that obstructions are encountered throughout the insertion path. B) When an obstruction is cleared by continuing linear pipette advancement, debris may still be present at the pipette tip, reflected by the persistent resistance increase of the pipette by 0.200 MΩ. C) Using a robotic navigation algorithm, pipette debris is prevented from accruing on the pipette tip, shown by the return of the pipette resistance to the baseline. Arrows indicate locations of robotic navigation event. D) Detail of a single robotic navigation event. A-D) initial pipette resistance was subtracted to show changes in resistance. Initial pipette resistances ranged from 4-7 MΩ. E) The final resistance of the pipette is significantly lower after insertion to 3mm below the pial surface when the robotic navigation algorithm to localize the pipette was used. F) The maximum resistance measured during robotic navigation is not significantly different between trials that gigasealed successfully (n=17) and trials that failed to seal (n=71), Wilcoxon rank sum test (p=0.19). G) The number of navigation events was not significantly different between trials that gigasealed successfully (n=17) and trials that failed to seal (n=71), Wilcoxon rank sum test (p=0.96) H) Histogram showing number of navigation events as a function of depth. Note the slight increase in navigation events around 0 μm and 2500 μm from the pial surface, where the pia and ventricular meninges were encountered, respectively. 54
- Figure 12 Neurons recorded in whole-cell configuration were of good quality. A) Example of spontaneous activity from a neuron recorded 3.2 mm below the pial surface with detail of spontaneous burst (arrow indicates burst shown in detail to the right). B) Example whole-cell traces recorded in the thalamus for 3 different neurons. Note the sag in membrane potential following hyperpolarizing current injection 59

(representing activity of Ih, as described in (Leist et al., 2016)) and after-hyperpolarization rebound bursting in each trace, indicative of thalamic neurons. Current injections lasted 0.5 sec and ranged from - 50 pA (first recording) to - 100 pA (second and third recording). C) Following hyperpolarizing current injection, rebound bursts exhibited after depolarization (ADP, see arrow) , consistent with ventrobasal thalamic nucleus cells (X. Wang et al., 2010b). Current injection was -150 pA.

- Figure 13 Schematic of motion compensation system for whole-cell patch clamp electrophysiology. Cardiac signals are recorded with an EKG and respiratory signals are captured with a piezo pickup under the animal's chest. These physiological signals are amplified and thresholded on an FPGA. Simultaneously, current fluctuations, indicative of a nearby cell moving with respect to the pipette tip are amplified on the patch amplifier and recorded along with the physiological signals on the DAQ. When enough data has been collected, the desktop computer computes the impulse responses and sends them to the Realtime computer. The real-time computer convolves the cardiac and respiratory impulse responses with the appropriate thresholded physiological signals, scales the resulting signal, producing a command signal for the piezo amplifier. The command signal is then amplified and is used to drive the piezo stack in the piezo linear stage. This results in the measurement of a stable resistance on the pipette electrode, indicating that the relative motion between the pipette tip and the cell is reduced. 72
- Figure 14 Spectral analysis of current modulation and the piezo stage. The amplitude spectrum of a recording of 10 seconds of current modulation by respiratory and cardiac motion (blue) is shown along with the magnitude response of the piezo stage used in this study to a sinusoidal frequency sweep at 1 Vpp (corresponding to 10  $\mu$ m peak-to-peak). The resonant peak of the piezo stage is at 47 Hz. 74
- Figure 15 Optimization of impulseest parameters. Various training data lengths and model orders were selected. Each combination of parameters was run 10 times. A) The quality of the fit (SSE, lower is better), and B) total time to calculate impulse response are plotted. Total time to calculate impulse response is the sum of training data length and the impulse response calculation time. Diagonal line in lower graph is the unity line. Inset: example of cardiac and respiratory filters (order: 128, training data length: 8 s) convolved with corresponding pulse trains. The result of the convolution is plotted (green) over corresponding current trace (gray). 79
- Figure 16 Alignment of intrinsic signal optical imaging (ISOI) signal with vasculature. Intrinsic images were captured 3 days prior to electrophysiology experiment. Here, the C1 whisker was rapidly stimulated and images were captured under red light (650 nm) before and after the stimulation and averaged over several trials. Darker regions indicate local consumption of blood oxygen, a proxy of activity. A co-registered blood vessel image is taken under 550 nm 83

light. A) Cortical vasculature can be seen through the thinned skull preparation under perfusion of saline. B) Blood vessel map is shifted, rotated and deformed to match it with the vasculature observed on the experiment day. C) The co-registered activity map indicates the region of activity for the C1 whisker and can easily be targeted by performing a craniotomy over the location of the dark spot seen in the center of the image.

- Figure 17 Compensation of angular difference between pipette axis and ISOI normal. The pipette axis is  $12.5^\circ$  from the axis normal to the ISOI image plane. The location of the barrel of interest is determined with respect to the pipette axis by trigonometry. The pipette (shown in blue here) is then brought to the surface of the brain in the center of the area of activity determined by the ISOI session and then moved approximately  $89\ \mu\text{m}$  medial to ensure that the pipette passes through the barrel of interest (red rectangle). 84
- Figure 18 Measurement of the relationship between pipette-membrane distance and gigaseal probability. A pipette was slowly lowered vertically onto a plated HEK293T cell. At a resistance increase of  $0.1\ \text{M}\Omega$ , the pipette is determined to be at the surface of the cell. The pipette is then moved into a random position between  $3\ \mu\text{m}$  above and  $7\ \mu\text{m}$  below the surface of the cell and a gigaseal is attempted. A) shows a schematic of this process. B) Gigaseal yield as a function of pipette position with respect to the membrane. Yield was calculated as the number of gigaseals / total number of attempts within a sliding  $2\ \mu\text{m}$  window. Pipettes  $2.5\ \mu\text{m}$  or more above the cell will never form a gigaseal with the pipette. There is a clearly optimal location to perform a gigaseal attempt ( $1\text{--}2\ \mu\text{m}$  below the surface of the cell). C) Pipette resistance increases as the pipette is stepped down into the cell. The cell surface is defined as the location where the pipette resistance increases  $0.1\ \text{M}\Omega$  above its initial resistance in the saline bath far above the cell. D) Number of trials at each depth (calculated with a  $2\ \mu\text{m}$  sliding window). 86
- Figure 19 Representative result of motion compensation on current amplitude modulation. Top trace: the pipette current is a proxy for the distance to a cell. The current modulation is indicative of a nearby cell moving with respect to the pipette tip. The current signal, along with the EKG signal and respiration signals, is used as input to MATLAB's `impulseest` function, which nonparametrically computes the contribution of each cardiac and respiratory event on the current signal. The resulting impulse responses are convolved with the thresholded EKG and respiration signals and used as the command signal for the piezo stage. The user manually scales the output of the convolved signal until the current modulation is minimized and then triggers the gigasealing attempt. After the arrival of the next respiratory event (typically the largest contributor to cellular micromotion by amplitude), the system waits  $0.5\ \text{s}$  and then applies gentle suction to rapidly form a gigaseal. In this instance, the series resistance increases to approximately  $400\ \text{M}\Omega$  before the arrival of 89



	the next respiratory event. At high series resistance, the seal is mechanically stable, so the motion compensation is turned off, and the break-in attempt can be performed to perforate the membrane and achieve a whole-cell configuration. Note that when the pressure is released, the resistance measurement square wave is applied.	
Figure 20	Results from whole-cell patch clamp experiments <i>in vivo</i> with various improvements. Gray rows indicate experiments conducted for this chapter. Green box indicates that the gigaseal formation stage is being optimized in this chapter. First row: Cortex and hippocampus recordings performed by Suhasa Kodandaramaiah in 2012. The remaining rows were performed by the author. As a result of the motion compensation described in this chapter and robotic navigation during RPL described in the previous chapter, thalamic whole-cell recordings can be performed with 24% yield (approximately 1 in 4 pipettes inserted into the brain will achieve a whole-cell state).	91
Figure 21	Representative data from a whole-cell recorded in the cortex demonstrating the effect of whisker stimulus and light stimulus of pre-synaptic terminals. This cell, labelled Cell 4 in this manuscript, was held for 35 mins. The resting membrane potential was -77 mV. Each sub figure contains a peri-stimulus time histogram with spike rate in spikes/s, a raster plot with square boxes indicating action potentials, baseline-corrected membrane potential fluctuations recorded in current clamp mode, and whisker and light stimulus recordings. Membrane potential was baseline corrected by calculating the histogram of voltage values for each trial and subtracting the most common value from the membrane potential for the trial. A) Punctate whisker stimulus with no whisker noise and no light stimulus. B) Light stimulus of thalamo-cortical axons in the mouse whisker barrel cortex. No whisker stimulus delivered. C) Whisker punctate stimulus embedded in whisker noise. Note that there is a slight increase in subthreshold activity due to the whisker noise and a significant subthreshold response in response to the punctate stimulus. However, there is no increase in spike rate above baseline. D) Light stimulus embedded in whisker noise.	96
Figure 22	Subthreshold response to whisker and light stimuli from five whisker responsive cells in the mouse barrel cortex. Cells 4 and 5 were strongly responsive to light stimulus of presynaptic neighbors. Cells 6 and 7 were less responsive to light stimulus. In each cell, the peak of the subthreshold response to punctate whisker stimulus embedded in noise was delayed with respect to the punctate whisker stimulus alone (Cell 4: 14.7 ms, Cell 5: 6.6 ms, Cell 6: 5.4 ms, Cell 7: 18.4 ms). Cells 4 and 7 showed a concomitant reduction in amplitude of the peak response and broadening of the subthreshold response to punctate whisker stimulus when the stimulus was embedded in noise.	98
Figure 23	Example of debris in pipette following an <i>in vivo</i> experiment	112

Figure 24 Improvement in yield of *in vitro* HEK293 patching. Each line represents the average number of whole-cells acquired after a given number of attempts. Sequential recordings were performed with the same pipette, totaling 30 or more attempts (except for Saline controls which were aborted after 15 failed attempts). Note the improvement in long-term yield when the cleaning agent changed from Alconox to Tergazyme. Note the further improvement gained by advancing the pipette 1 additional micron into the cell (application of results obtained in Chapter 4 of this work).

115

## LIST OF SYMBOLS AND ABBREVIATIONS

ACSF	Artificial Cerebrospinal Fluid
AFM	Atomic Force Microscope
BRAIN Initiative	Brain Research through Advancing Innovative Neurotechnologies Initiative
CCD	Charge Coupled Device
ChR2	Channelrhodopsin
DAPI	4',6-diamidino-2-phenylindole
DAQ	Data Acquisition Device
DIC	Differential Interference Contrast microscopy
DNA	Deoxyribonucleic Acid
DPDT	Double-Pole Double-Throw
FSM	Finite State Machine
GFP	Green Fluorescent Protein
GUI	Graphical User Interface
HEK	Human Embryonic Kidney
IACUC	Institutional Animal Care and Use Committee
ISOI	Intrinsic Signal Optical Imaging
LCD	Liquid Crystal Display
MEM	Minimum Essential Medium
PFA	Paraformaldehyde
PLA	Poly Lactic Acid
RPL	Regional Pipette Localization
S1	Primary Somatosensory Cortex
SDBS	Sodium dodecylbenzenesulfonate
SICM	Scanning Ion Conductance Microscopy
SSE	Sum of Squared Errors
USB	Universal Serial Bus
V1	Primary Visual Cortex
VPL	Ventral Posterior Lateral (thalamic nucleus)

## SUMMARY

One of the most foundational ideas in neuroscience is the neuron theory. It established the neuron as the irreducible unit of the brain and set in motion a hundred years of research into the morphology, chemistry, electrophysiology, genetic properties, and responses to physiological stimuli of single cells in the living brain. Myriad techniques have been developed to probe these axes of measurement from golgi staining to cyclic voltammetry, extracellular recording to genetic manipulation. With these tools, neuroscientists seek to better understand how individual cells, their properties, and the circuits that they are embedded in produce sensory perception, behavior, and consciousness, and what the underlying differences are between healthy brains and those of organisms with neurological disorders.

Similar to the human genome project completed in the early 2000's, one goal shared by many neuroscientists is to generate a single cell atlas of hundreds to thousands of cell types (Lein et al., 2007) throughout the brain by simultaneously capturing data on several axes at once. One technique that is well suited for this work is the whole-cell patch clamp technique, which provides stable intracellular access to cells in the living brain. This access is acquired by docking the tip of a glass pipette onto the surface of a single cell, sealing a portion of the membrane to the interior of the pipette, and then rupturing a small portion of the membrane so that the fluid in the pipette forms a bridge between the single cell and a recording amplifier. This connection permits the recording of exquisitely detailed transmembrane voltages and currents and provides excellent isolation so that only the electrical activity of the attached cell is recorded.

This process, however, is exceptionally laborious and has a prohibitively low success rate, especially in regions of the living brain several millimeters below the cortex. For a successful investigation of the brain that results in a multimodal cell types database, including responses to physiological input, it is imperative to perform these highly valuable patch clamp recordings at high yield throughout the brain. This work presents three techniques to open the door for such an investigation. The first technique is the application of automated patch clamping technology to the cell-attached configuration and delivery of genetic material to single cells through electroporation, allowing electrophysiological and morphological recordings to be performed on single cells *in vivo*. The second technique is an algorithm for the active avoidance of blood vessels during the localization of pipettes to the thalamus which prevents clogging of the pipette tip. The third technique is the on-line compensation of physiological micromotion between the cell and the pipette tip. This compensation greatly increases the success rate of gigaseal and whole-cell formation in the thalamus.

The second and third techniques were deployed along with other innovations to the patch clamping method described in appendix Sections APPENDIX A, A.2, and A.3 to acquire high-yield cortical recordings in the thalamo-cortical circuit. The success rate in these experiments was 40% (n=8 whole cells, 12 gigaseals, 20 attempts), and we were able to record from cells for 15-30 minutes with minimal human intervention.

Together these techniques represent a suite of tools for neuroscientists that open the door for high-throughput, multi-modal measurements throughout the living brain.

# CHAPTER 1. INTRODUCTION

## 1.1 Motivation

The human brain is composed of 86 billion neurons, each connected to its neighbors by thousands of synapses (Herculano-Houzel, 2009; Pakkenberg et al., 2003). It is the activity of this collection of neurons, and the wiring diagram that interconnects it, that generates our consciousness. An understanding of this complex tissue is paramount to combatting neurological disorders of aging such as Parkinson's and Alzheimer's diseases and diseases of the mind such as depression and psychopathy. This understanding will require new tools of measurement, modification, and modeling to probe the brain at higher resolution than is currently possible. The development of these tools will require a highly collaborative, coordinated effort from thousands of scientists. Inspired by the success of the Human Genome Project in the 90's, the United States and Europe have recently set goals to map the cells and circuitry from the entire brain (Bargmann, Newsome, Anderson, & Brown, 2014; The Human Brain Project, 2012).

The Human Genome Project was a 13 year, multi-billion dollar effort in the United States to produce the first, complete, reference human genome consisting of 3.3 billion base pairs (Collins, Morgan, & Patrinos, 2003). In 1993, three years after the inception of the project, scientists argued that the point of the project was not just the 'single map' that would officially mark completion of the project, but rather the tools that we built along the way would give us the ability to sequence entire genomes faster and faster. (Sawicki, Samara, Hurwitz, & Passaro, 1993) This in turn would produce ancillary tools for gene therapy, disease identification, and gene editing for the production of novel structures. Indeed, 15

years after the declaration of the project completion in 2003, exciting new insights into the genetic basis of diseases are being produced not by reference to the initial atlas, but by high-throughput creation and comparison of individual genomes (Gonzaga-Jauregui, Lupski, & Gibbs, 2012). Similarly, new tools for genetic therapeutics have been developed and deployed in human cells (Shalem et al., 2014). The success of these comparative studies and the development of therapeutic tools is primarily based on the decreasing cost of genome sequencing. This decrease in cost (nearly \$100M in 2001 to nearly \$1k in 2017) is itself a result of new methods that have vastly increased the speed and reliability of whole-genome sequencing (Wetterstrand, 2017). A similar increase in throughput and decrease in cost will be required to record data from thousands to millions or billions of cells in the living brain.

The atomic unit of the brain is the neuron, a branching, tree-like cell that can perform computations with fluctuations in the electrical potentials across its membrane and communicate to its neighbors with chemical signals. In the early 20<sup>th</sup> century, Santiago Ramon y Cajal pioneered a histological procedure to reveal a sparse population of these neurons in the dense, webbed network of the brain (Cajal, 1899). Not only did he draw the myriad of structures he saw, revealing cells of vastly different sizes and arborizations, but he connected them with arrows into networks, decades before the first signals were recorded from individual neurons.

Recently, scientists have developed techniques to reveal not only the fine structure of these neurons but record the subtleties of their electrical activity. The simultaneous classification of these neurons into cell types by electrical activity, morphology, genetic expression, and connectivity throughout the brain is a major thrust of the Brain Research through

Advancing Innovative Neurotechnologies (BRAIN) Initiative (Bargmann, Newsome, & Anderson, 2014a), a multi-billion dollar federal effort to develop new tools to study the brain announced by President Obama in 2014.

Patch clamp recordings are a gold-standard technique for probing the electrophysiology and morphology of single cells in the living brain and are therefore uniquely positioned for the classification of neuronal cell types. While valuable, the performance of these experiments *in vivo* is time consuming, highly manual, and suffers from low yield. *In vivo* patch clamping also presents unique challenges, including the identification, acquisition, and maintenance of single-cell contact, often without visual guidance in moving tissue.

To improve the throughput and reduce the barrier to entry for these high value experiments, the Forest lab recently developed the Autopatcher, a robot that automatically performs whole-cell recordings in the living mouse brain by algorithmically detecting and recording from individual cells. Towards the goal of the BRAIN Initiative to develop tools to, “enable novel automated and scalable analyses of single neurons *in situ*,” and enable high-throughput cell typing throughout the living brain, I propose to (1) automate cell-attached recording and single cell labeling *in vivo*, (2) develop an algorithm to enable whole-cell electrophysiology far below the cortical surface, and (3) improve the yield of gigasealing in subcortical regions *in vivo*. The development of this system will open the door for a host of high-value experiments throughout the brain, including rapid cell type categorization along electrophysiological and morphological axes.



## 1.2 Overview of Electrophysiological Methods

### 1.2.1 *Patch clamp*

Patch clamping refers to the act of docking the aperture of an electrode, typically  $\sim 1\ \mu\text{m}$  in diameter onto the surface of a single cell. During this docking process, a small portion of the cell's membrane (the patch) is pulled into the aperture by the application of gentle suction and may seal onto the interior surface of the electrode. This seal may be a high resistance or gigaohm seal, as in the case of the whole-cell patch clamp or it may be a low resistance seal as in the case of the cell-attached patch clamp. In both cases, the presence of the membrane within the electrode blocks the flow of current out of the aperture to ground, and the resistance to current is a result of the tightness of the seal of the membrane with the interior surface of the electrode. Finally, this electrode can take one of several configurations. It may be a micron-scale hole in a flat glass surface or it may be the tip of a conical glass electrode. In this manuscript, the conical glass electrode is discussed exclusively.

Patch clamp pipettes are formed by heating a glass tube (typically 1-1.5 mm OD, 0.5-0.8 mm ID) in the middle with a heat source (flame, heated filament, or laser) until the glass transition temperature is reached. At this point the glass has begun to melt and is pulled axially until the heated region can be drawn out into a cone. When the middle portion of the electrode separates, two needle-like conical glass electrodes are produced.

In the physiological experiments used throughout this thesis, the glass tube is filled with an electrolyte solution, often formulated to match the specific salt composition of the intracellular space. This electrode is then inserted into a pipette holder which contains a silver-silver chloride wire that connects the saline in the electrode with the electronics in

the amplifier. The pipette holder also contains a port for pneumatic access, which allows the user to select a positive or negative pressure to place on the pipette. This pressure is changed throughout the experiment, depending on the stage. For example, when a pipette is being advanced rapidly through brain tissue, it is typically placed under high positive pressure to prevent ingress of contaminating cellular debris. When the pipette is near a cell, however, the pressure is released to permit a small portion of the membrane to enter the pipette tip and form a low resistance seal in the case of the cell-attached patch or a high resistance seal in the case of the whole-cell patch clamp configuration.

#### 1.2.1.1 Whole cell patch clamp

The formation of high-resistance seals has been crucial for the discovery of mechanistic processes in individual neurons. The single channel patch clamp process, originally published in the early 1970's, earned Bert Sakmann and Erwin Neher the 1991 Nobel prize (Sakmann, 2013). This technique relied on a gigaohm seal, or gigaseal ( $> 1 \text{ G}\Omega$ ), to reduce electrical noise and permit the recording of ionic currents flowing through individual channels (on the order of single picoamps). Today, this technique is used to discover the response of wild type and mutant channel types to pharmaceuticals, discover and screen new microbial opsins, and investigate the physiological properties of individual cells and local networks in brain tissue, among many other uses. Patch clamping was extended in 1981 to include several other configurations of the membrane-pipette interface that could be achieved with various applications of suction and pipette retraction. These configurations included the cell-attached or loose-seal configuration, inside out, outside

out, and importantly, the whole-cell configuration (Hamill, Marty, Neher, Sakmann, & Sigworth, 1981).

The whole-cell configuration is achieved, following the formation of a gigaseal, by rupturing the patch of membrane in the pipette and creating a continuous fluid connection, or salt bridge, between the cell's cytosol and the amplifier electrode. This connection not only enables the recording of sub and suprathreshold currents and voltages that comprise the somatic response to incoming synaptic transmissions, but also enables the exchange of fluid between the electrode and the cytosol. This intracellular access enables single cell labelling for morphology, the transfection of genetic constructs, and the recovery of mRNA transcripts for genetic expression profiling (Jiang et al., 2015).

#### 1.2.1.2 Cell attached patch clamp

It is possible to form a seal with a neuron and record well-isolated activity from across the cell membrane without forming a gigaohm seal. Cell attached patch clamp seals are typically between 5-50 M $\Omega$ . One drawback of this low-resistance seal is that the pipette does not have intracellular access to the cell, and as such is not able to record subthreshold activity nor is it possible to clamp the voltage of the cell. However, the cell-attached patch configuration confers some benefits over the whole-cell configuration. Primarily, following the conclusion of recording from a single cell, the pipette can be retracted and reused without exchanging the glass electrode or cleaning it. Second, it is possible to open a transient pore in the patched membrane by the application of a voltage large enough to cause dielectric breakdown of the cell membrane.

### *1.2.2 Scanning Ion Conductance Microscopy*

Scanning Ion Conductance Microscopy (SICM) is one of a family of techniques involving scanning probe microscopes, including Atomic Force Microscopy (AFM), where a physical probe is moved across a surface to create a very high-resolution image. In the case of SICM, a glass electrode, typically with resistances on the order of 100 M $\Omega$  (though in this manuscript, the electrode is a patch pipette with resistance between 5-10 M $\Omega$ ) is scanned over a surface and the resistance is measured as a function of position (Rheinlaender & Schäffer, 2013; Shevchuk et al., 2001; Takahashi et al., 2010; Tognoni, Baschieri, Ascoli, Pellegrini, & Pellegrino, 2016). When the tip of the glass electrode is brought near a surface or biological sample, the presence of a non-conductive surface within approximately 1 radius of the pipette tip impedes the flow of ionic current to ground. The degree to which the current is impeded is a function of the distance of the pipette tip to the surface under analysis.

## **1.3 Project Motivation**

While this work focuses primarily on the development and demonstration of tools for recording from single cells throughout the brain with high success rate, this work originally began as a collaborative scientific investigation of the thalamocortical pathway using simultaneous dual whole-cell recordings in the thalamus and cortex. With the recording of dual, synaptically connected cells in this pathway, an investigator can answer fundamental questions about the nature of subthreshold membrane potential on sensory information encoding in the thalamus, how this resting membrane potential changes with changes in

stimulus type (novel stimuli vs. repetitive stimuli), and if or how the synaptic strength is modulated as a function of membrane potential or stimulus modality.

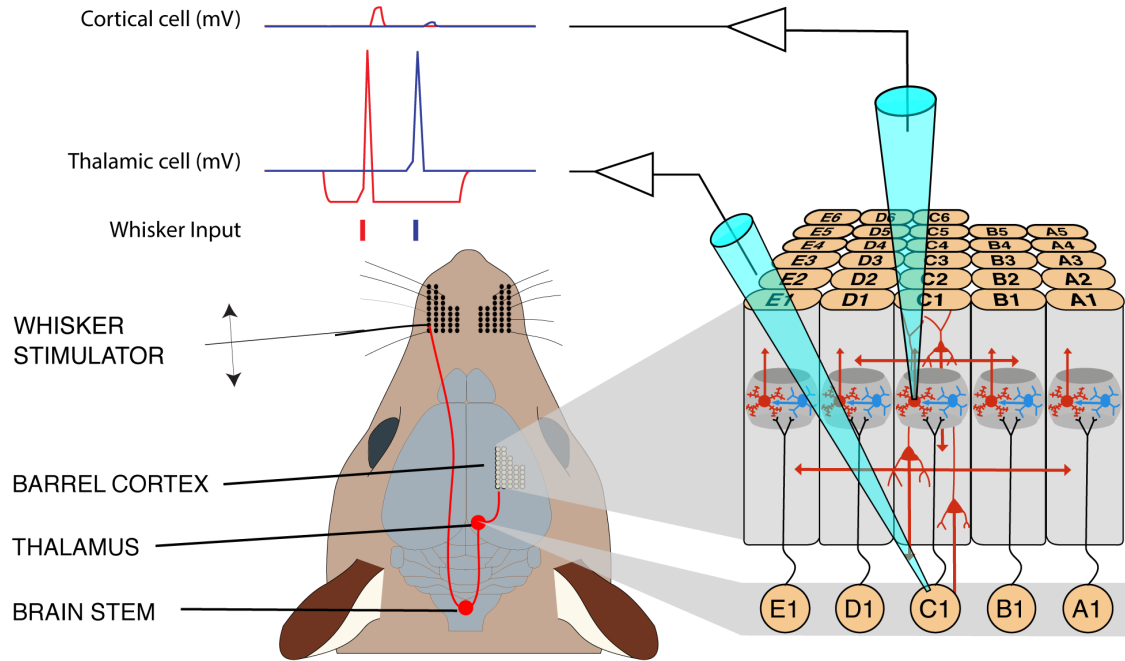


**Figure 1:** Schematic of proposed dual-patch recording in the thalamus and cortex that motivated the methodological improvements in this work. Figure adapted from (Diamond, von Heimendahl, Knutsen, Kleinfeld, & Ahissar, 2008)

The first-pass approach to address these scientific questions was to directly apply the robot developed by Kodandaramaiah and others in 2012 in a linear fashion to dual recordings. The reported yield in the cortex in the original paper was approximately 30%, so we reasoned we could expect an approximately 9% chance of achieving simultaneous recordings in the thalamus and cortex. However, a preliminary study with only thalamic patching resulted in only a single whole-cell recorded in 95 attempts. It became clear that a new approach would be required to permit cortical and subcortical patch clamping at high success rates to begin to address ambitious scientific goals such as this.

#### 1.4 Assessment of the likelihood of project success

When a car is built on an assembly line, a series of processes is performed to the chassis, some of which depend on the successful installation or modification of a part in a previous step. For example, the installation of the wheels depends on the previous proper installation of the hub, which is dependent on the successful installation of the axle, and so forth. The installation of each part is considered a success or failure depending on its positional tolerance, among other factors. If a part is out of tolerance, the entire chassis may be pulled off of the line and require extra attention. On an assembly line, this extra attention costs time and money, and so process engineers have developed methods for reducing the overall number of failures. These techniques include process parallelization where possible, and a thorough investigation of failure modes within processes when serialization is required.

Several years ago, my colleague, Suhasa Kodandaramaiah reduced the patch clamping process to an algorithm and implemented the process using computer control of micromanipulators, pressure regulators, and data acquisition hardware. This work identified four steps in the process of acquiring a whole-cell *in vivo*, 1) Regional Pipette Localization, 2) Neuron Hunting, 3) Gigaseal Formation, and 4) Break-in. These processes are necessarily performed in serial. Similarly, the acquisition of synaptically connected whole-cell pairs in somatotopically aligned thalamocortical regions can be reduced to a serial algorithm. Namely, 1) Whole-cell recording in the VPM, 2A) Whole cell recording in the cortex, 2B) somatotopic alignment of barrel (cells in the same discrete thalamocortical pathway, i.e. a thalamic cell in the C2 whisker barreloid and a cortical cell in the C2 whisker barrel), and 3) Synaptic connection of both whole-cells.

Using previously published data from Kodandaramaiah et al 2012, we can estimate that the cortical whole-cell success rate is 30%. Based upon our pilot studies, the whole-cell yield

for neurons 3+ mm below the pial surface is approximately 1% ( $n=1/95$ ). Additionally, because the precise location of the VPM is not known *a priori*, and varies from animal to animal, we must attempt to hit the VPM using stereotaxic coordinates or extracellular mapping studies from other animals of the same age. It is difficult to put a number to the success rate of acquiring somatotopically aligned whole-cell recordings, but we will be generous and assign it a probability of 50%. Finally, even with somatotopic alignment of two whole cells in the thalamocortical circuit, the probability of a synaptic connection between these neurons has been estimated by our collaborators to be 25% from previous histological studies. Because these are serial processes, we can assign an overall success rate to the acquisition of two synaptically connected cells in the thalamocortical circuit of a mouse by multiplying each probability together:  $30\% * (1\% * 50\%) * 25\% = 0.0375\%$ . This is a 1 in 2667 chance of recording a cell on any given trial. However, we do not need just one recording. Similar studies that have reported whole-cell recordings in the thalamus have reported, on average,  $28 \pm 15$  whole cells (Groh et al., 2014; Margrie, Brecht, & Sakmann, 2002; Oberlaender, de Kock, et al., 2012; Oberlaender, Ramirez, & Bruno, 2012). Again, let's be generous and require only 10 synaptically connected pairs.

We can now calculate the likelihood of obtaining at least  $k$  such recordings with an individual probability  $p$  after  $n$  trials using the binomial distribution's cumulative distribution function:

$$F(k; n, p) = \Pr(X \geq k) = 1 - \Pr(X < k) = 1 - \sum_{i=0}^{k-1} \binom{n}{i} p^i (1-p)^{n-i}$$

Where

$$\binom{n}{i} = \frac{n!}{i!(n-i)!}$$

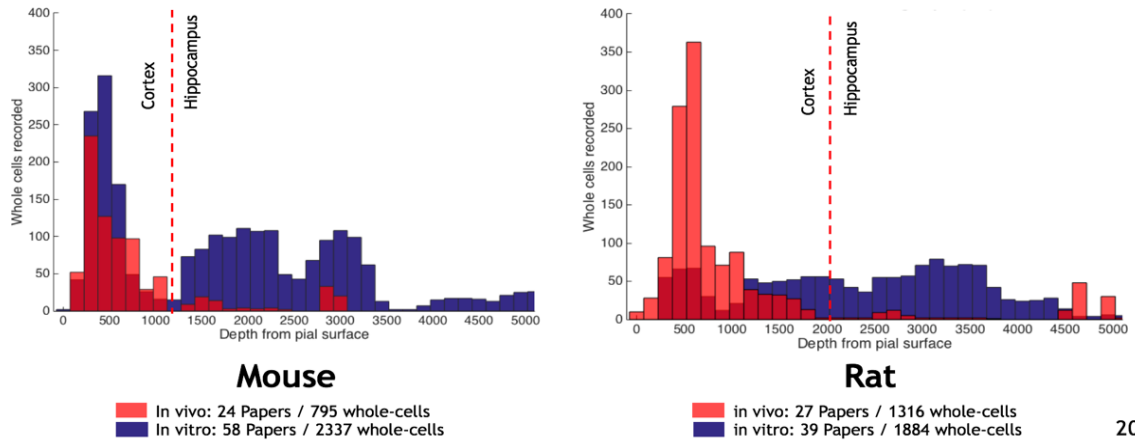
For example, if we perform 20,000 trials with this success rate, there is only a 22% chance that we will achieve 10 pairs of whole-cells. Twenty thousand trials would be approximately 2,000 mice, which would take nearly 5 ½ years (working 365 days a year) to perform. To enable the study of this system as set forth in the previous section, new tools and methods need to be developed that improve the yield of each step in this process.

### 1.5 Literature review of *in vivo* and *in vitro* patch clamp electrophysiology

Before beginning to improve well-established protocols such as the *in vivo* whole-cell patch clamp method, it is necessary to thoroughly examine the literature to determine the prior art. This is especially helpful for ensuring that the methods used are as optimized as possible. When performing method development, this is also a useful process for extracting data and uncovering hidden patterns in the field of interest. In this case, I used Google Scholar and the NeuroElectro database (neuroelectro.org) to build a list of the 51 most cited papers that performed *in vivo* whole-cell recordings and the 97 most cited papers that performed *in vitro* whole-cell recordings. In total there are 6,232 whole cells in the papers that have been analyzed here. For *in vivo* recordings, locations of recorded cells are typically listed either as precise depths, mean depth  $\pm$  sd, or a range of depths. For *in vitro* recordings, the subcortical nucleus, brainstem nucleus, cerebellar nucleus, or cortical layer are typically reported. The ‘depth’ of *in vitro* recordings is estimated by measuring the shortest distance to the pial surface using the Allen Institute’s Mouse Brain Reference Atlas



(brain-maps.org). A range of depths was computed from the nearest to the furthest part of the nucleus from the pial surface. For each  $n$  cells reported in a particular brain region, the cells were evenly distributed over the specified range and a histogram of the depths was generated for each species (mouse or rat) and each preparation (*in vivo* or *in vitro* slice).



20

**Figure 2:** Whole-cell recordings are desirable but difficult to perform below the cortex *in vivo*. A total of 148 papers that performed the whole-cell technique *in vivo* and *in vitro* in mice and rats were analyzed to determine the yield of whole-cell recordings as a function of depth. Reports of whole-cell recordings were significantly rarer below 3mm from the pial surface (5% of all whole cell recordings). However, in brain slices, where pipettes do not have to travel through millimeters of tissue do not show a strong preference for physiological superficial tissue.

The results indicate that the number of *in vivo* whole-cells reported in literature is highly depth-dependent. That is, there are significantly fewer reports of whole-cell recordings below the cortex than there are in the cortex. This pattern is consistent across mice and rats; however, the pattern is not consistent across preparations. When slices of tissue are cut from an animal's brain, they are often placed under a microscope for electrophysiological recording. In this configuration, tissue that was once deep in an animal's brain is accessible to electrodes under visual guidance. In this way, slice preparations are a kind of coordinate transform of the brain tissue. With easy access to tissue, researchers record from all brain

regions with approximately the same frequency. This is reassuring- it may have been the case that subcortical nuclei simply did not contain cells that were scientifically interesting!

This analysis has uncovered that, while cells and circuits below the cortex are ripe for study, they are, for one reason or another, inaccessible to researchers when they are in the *in vivo* preparation. We now have a problem statement for subcortical neuroscience *in vivo*: whole-cell recordings in the living brain are either difficult to achieve or maintain, or they are of low quality. It is now clear that in order to have success in the dual-patching project, we must first develop new tools to allow us to overcome the limitations that are holding back the field from accessing this scientifically valuable tissue.

## **1.6 Engineering design by methodological comparison**

Throughout the majority of this work, I have taken as my goal the improvement of whole-cell electrophysiology outcomes in subcortical structures, deep in the living mouse brain. The first step in improving this process is to identify the appropriate quality metrics to quantify what it means to have a successful patch clamp trial. Second, we can identify failure modes in our desired method and compare the steps in which they occur to analogous steps in similar methods. Finally, we can design solutions from first principles to address the identified need by altering the conditions of the method so that we achieve our desired outcome with a higher success rate. As an example from this work, I identified the low gigaseal formation success rate in the thalamus, determined that a key difference in this step between the *in vivo* and *in vitro* preparations was the presence of cardiac and respiratory motion, and designed a feedforward system to compensate for that physiological motion and dramatically improve the gigaseal rate in the thalamus.

### *1.6.1 Quality metrics*

The overall success of these experiments depends principally on the trial-by-trial success rate, or yield of gigaseal formation, and the quality of the recordings produced by each successful whole-cell configuration, measured by the access resistance and the longevity of the recording.

The longevity of the whole-cell configuration, when a scientific experiment is performed, should be sufficient to record many replicates of each stimulus presentation. In the case of this work, in Chapter 4, I present whole-cell recordings in the cortex where 2 optical conditions and 2 whisker stimulus conditions are combined. This produces 4 outputs, each 5.5 seconds long. Approximately 50 replicates of each stimulus would be sufficient for this study, therefore each whole-cell recording will be considered successful if it is maintained with low access resistance for at approximately 18 minutes.

The access resistance of the patch measures the resistance of the very tip of the pipette after achieving a whole-cell configuration. Lower access resistance is desirable because it enables the experimenter to measure the true membrane potential of the cell in current clamp mode, as well as to precisely clamp the membrane potential in voltage clamp mode. Additionally, low access resistance whole-cell recordings are essential to allow dyes or genetic material to diffuse into the intracellular space for later histological analysis of the cell's morphology. Specifically, in this work, we define a quality whole-cell recording as one with an access resistance below 50 M $\Omega$ . These quality parameters ensure that recorded cells can be used for experiments to elucidate their role in local microcircuits, sensory input systems, or understand their morphology and intrinsic electrophysiology. In short, we want

to ensure that when we have a cell, it can be used to gather useful data for scientific exploration.

### 1.6.2 Methods comparison

The process by which I have identified appropriate areas for improvement of the subcortical whole-cell patch clamping method have mainly resulted from a careful comparative analysis of the relative yields and methods *in vivo* and *in vitro* slice and HEK293 patch clamping studies.

	<i>in vivo</i>	<i>in vitro</i> (slice and HEK293)
Tissue Traversal	Overlying tissue must be traversed (100's to 1000's of $\mu\text{m}$ )	Cells are recorded within 50 $\mu\text{m}$ of the slice surface
Cell Motion	Motion due to cardiac and respiratory events	No Motion
Tip placement with respect to the cell soma	No control over placement of pipette tip with respect to the soma	Pipette tip is visually guided to a precise position with respect to the soma

**Table 1:** Comparison of *in vivo* and *in vitro* whole-cell patch clamping methods

First, patch clamp recording requires direct, physical access to the cell of interest. For cells deep in the brain, this requires a long, conical glass electrode to be plunged through overlying brain tissue, which directly damages cells, disrupts passing axons and dendrites, and can damage blood vessels, disrupting perfusion of downstream tissue. As more and more pipettes are inserted into the brain, the tissue becomes increasingly damaged. This has negative implications for both the physiological relevance of the tissue and because it

reduces the yield of subsequent trials (Kodandaramaiah, Franzesi, Chow, Boyden, & Forest, 2012). Additionally, the movement of electrodes through brain tissue permits the ingress of fragments of cell membranes into the pipette tip. This ingress can increase the access resistance of whole cell recordings deep in the brain (Margrie et al., 2002) but it can also prevent the formation of gigaseals. In contrast, patch pipettes do not have to traverse more than a few 10's of  $\mu\text{m}$  of tissue under visual guidance in slice electrophysiology preparations. As a result, clog formation while moving the pipette is near the cell of interest (regional pipette localization) is almost non-existent. This process has an effectively 100% yield *in vitro*.

Cell movement with respect to the pipette tip is another distinguishing feature of *in vivo* experiments. Neuronal soma (cell bodies) are approximately 10  $\mu\text{m}$  in diameter. Movement in biological tissues *in vivo* (under anaesthesia) is predominantly due to rhythmic motion from cardiac and respiratory function. It has been hypothesized that this motion is transmitted through the brain via the spinal cord and brain stem, or that it is caused by the local expansion and contraction of vasculature during the cardiac cycle (Sungon Lee, Courties, Nahrendorf, Weissleder, & Vinegoni, 2017). This motion has been estimated to be between 1 and 30  $\mu\text{m}$  peak-to-peak (Fee, 2000; Gilletti & Muthuswamy, 2006; Sungon Lee et al., 2008), or up to 3x the cell diameter. Finally, although all mice were anesthetized for the work presented in this thesis, awake animals present further, voluntary, and aperiodic sources of motion artifacts which must be taken into account when designing experiments. *In vitro*, there is no source of physiological motion, and gigaseals readily form in slices of brain tissue with  $\geq 70\%$  yield (Kolb et al. manuscript under review).

Finally, the tip placement with respect to the cell soma in slice preparations is controlled manually (or under computer guidance, (Desai, Siegel, Taylor, Chitwood, & Johnston, 2015; Wu 吴秋雨 et al., 2016)). Desai et al. have shown an interesting gradient-ascent approach to finding a good location on the soma to form a gigaseal, although they did not perform rigorous experiments to demonstrate the optimality of patching on the center of the cell. In the living brain, however, the movement discussed in the previous paragraph prevents high precision placement of the pipette with respect to the membrane. Additionally, for cells below approximately 800  $\mu\text{m}$  in the cortex, visual guidance is not possible with current non-invasive microscopy techniques. I do not address this potential improvement to the patch clamping method in this thesis. Rather, I assume that the plume of fluid being ejected from the patch pipette pushes away cells that are not aligned with the pipette and selects for cells centered with respect to the pipette axis.

## **1.7 Automation**

There are three main benefits to automation of patch clamp electrophysiology. The first benefit is that for an automated or semi-automated platform, the user can either walk away from the preparation (Kolb et al., 2016) or the user can potentially operate multiple rigs at once, scaling the output of their efforts. The second benefit is that automation improves the repeatability of this previously manual and highly variable process. By reducing the variability, the process can be optimized through a series of iterative tests. We have employed this procedure to improve walk-away *in vitro* whole-cell recordings with a new pipette cleaning chemical discovered with hypothesis-based testing (See Sections A.2 and A.3). Finally, automation enables the algorithmic improvement of the success rate or yield

of the process. With high success rates, the brain tissue can remain intact with minimal pipette insertions and high-value experiments can be performed in regions of the brain that were previously inaccessible.

Improvements to patch clamping in the past have focused on the integration of heuristics of humans. For example, the original Autopatcher integrated a suite of patch clamping best practices (i.e. wait 10 seconds after detecting a neuron before patching, check resistances before and after moving the pipette to the region of interest). Further improvements of the *in vitro* case have focused on identification and tracking of cells in slices of brain tissue (Wu 吴秋雨 et al., 2016). Identification and tracking of cells *in vivo* has also proceeded as an adaptation of human heuristics (Suk et al., 2017).

A similar approach has been taken here by incorporating heuristics from previous methods such as the navigation of pipettes around blood vessels while moving the pipette to the region of interest (D. Lee, Shtengel, Osborne, & Lee, 2014). The automated electroporation system described in Chapter 2 comprised of the reduced to algorithm of previous *in vivo* manual electroporation methods. However, there are improvements to the patch clamp process that can be performed in an automated fashion but that cannot be performed by a human. For example, we developed a method to synchronize the position on a micrometer scale with the surface of a cell *in vivo*. This synchronization is something that absolutely could not have been done manually by a human and would require automation.

Additional improvements may include the detection and identification of cells in proximity to the pipette by electrical impedance spectroscopy or another electrical measure so that a determination of a suitable whole-cell target can be made prior to the gigaseal attempt. For

example, in Li et al 2016, we determined that there there was a 90% chance that a neuron detection event was caused by a neuron rather than glia or a blood vessel.



## **CHAPTER 2.     AUTOMATED EXTRACELLULAR PATCH RECORDING AND DELIVERY OF GENETIC MATERIAL VIA ELECTROPORATION**

Portions of the results described in this chapter have been previously published in (Li et al., 2017)

### **2.1    Introduction**

The Allen institute for Brain Science is a Seattle-based research institute founded in 2003 dedicated to creating large-scale maps of the brain, in increasingly higher resolution, and releasing them for the public to use. Their inaugural project, the Allen Brain Atlas, was released in 2006 and was a 3-dimensional map of genetic expression in the brain. This map was produced by colorimetric in-situ hybridization of 22,000 genes across the entire mouse brain (Lein et al., 2007). The scale of this project required the creation of ‘pipelines’, or sets of personnel, equipment, and standardized procedures that would handle individual components of the project, such as mouse breeding, brain fixation, hybridization, slide preparation, microscopy, and data processing. In a subsequent atlas project, a similar method of pipelining for large-scale neuroscience was used to map connected regions by viral injection of fluorescent reporters in hundreds of stereotyped locations throughout the brain. These two axes, connectivity and gene expression are each individually useful to scientists all over the world- the freely accessible website that they are listed on is visited millions of times a year.

However, a central question of the brain that is left unanswered, even by collections of atlases of various descriptions, is the identity of individual cell types on multiple axes. That

is, what is the correspondence between the intrinsic electrophysiology, the morphology, and the response to physiological stimuli? It remains one of the ambitions of the Allen Institute, and specifically our collaborators Lu Li and Hongkui Zeng, to unify the activity-structure relationship on a large scale.

The production of such a data set would require a technique to resolve and record the activity of single cells and a method to deliver contrast to the recorded cell for later imaging. Additionally, this method must be applicable throughout the intact mouse brain, including the cortex, thalamus, olfactory bulb, brain stem, and cerebellum. Although highly scalable, optical methods are typically restricted to superficial layers. Methods that permit recording of subcortical nuclei typically rely on removal of the cortex or the insertion of prisms into the tissue (Andermann et al., 2013). Intracellular glass electrodes are uniquely positioned to achieve the unity of this multidimensional data because well isolated electrical recordings can be made, and dye or other contrast agents can be allowed to diffuse into the intracellular space. However, for whole-cell recordings, the requirement of the gigaseal drastically reduces the yield of recordings. Cell-attached recordings, on the other hand, permit good isolation and enable recordings of single action potentials with a seal resistance of only a few megaohms (Pinault, 1996). Additionally, the patch of membrane within the pipette can be temporarily electrically perforated, or electroporated using a series of brief, high-amplitude, voltage pulses (Kitamura, Judkewitz, Kano, Denk, & Häusser, 2008).

Unfortunately, electroporation only permits the exchange of a small volume of fluid between the pipette and cell, so fluorescent dye or biocytin are unlikely to fully label recorded cells, although this has been previously attempted (Kanjhan & Vaney, 2008;

Pinault, 1996). Further confounding the use of these contrast agents, they are readily taken up by cells from the extracellular space and are often the cause of non-specific or off-target staining. We instead opted to deliver DNA plasmids via electroporation, as others have done previously (Haas, Sin, Javaherian, Li, & Cline, 2001; Oyama et al., 2013).

The unification of these types of data has been previously performed in the mouse brain (Joshi & Hawken, 2006; Kitamura et al., 2008; Oyama et al., 2013), however the results of each paper have not been replicated in further studies (Dempsey, Turner, Le, Sun, Bou Farah, et al., 2015). Here, I take as my goal the automation and standardization of electrical recording and genetic manipulation via electroporation of single cells in the living mouse brain. I report the design and results of the robot, which is based, in part, on the previously published Autopatcher technology (Kodandaramaiah et al., 2012). I also demonstrate that the patch headstage of a traditional electrophysiology rig can be used to record from and electroporate single cells *in vitro*, which lowers the barrier to entry for the use of this method, beyond what we have previously published (Li et al., 2017). Together this provides a unified method for high-throughput fusion of morphological and electrophysiological data from single neurons in the living brain.

## **2.2 Methods**

### *2.2.1 Animals*

In vivo and *in vitro* experimental procedures were in accordance with NIH guidelines and approved by the Institutional Animal Care and Use Committee (IACUC) of the Allen Institute for Brain Science and the Georgia Institute of Technology, respectively. Forty-

seven adult C57BL/6J wild-type mice (2–5 months old, both genders) were used in the *in vivo* study. Of the 47 mice, 20 mice were used for the development of the robot. Two male C57BL/6J mice were used for *in vitro* (brain slice) testing.

### 2.2.2 Hardware

The robot contains the following major hardware components:

- (1) electrophysiological data acquisition equipment, including a headstage (CV-7B, Molecular Devices) connected with a patch-clamp amplifier (MultiClamp 700B, Molecular Devices, USA) and digitizer (1440A, Molecular Devices, USA)
- (2) An electroporation headstage (AP-1A, Molecular Devices) and voltage source (Axoporation 800A, Molecular Devices, USA)
- (3) A microstepping piezo-motor and linear stage (PZA12, Newport, USA)
- (4) A pressure control box with resistance-measuring DAQ (Neuromatic Devices, USA)
- (5) An electrode holder (1-HL-U, Molecular Device) coupled with a custom-made electrode holder adapter (3D printed in PLA) to accommodate the switch relay (a double pole, double throw relay, Digikey, USA)

The headstage, electrode holder with adapter and linear step motor are assembled together and mounted onto a MP-285 3-axis manipulator (Sutter, USA) for initial pipette positioning. All hardware components are controlled by a custom developed, LabView-based software through analog and digital commands sent from the Autopatcher's

embedded DAQ (switches, resistance measurement), and via USB (Newport and Sutter stages / manipulators). The control software features a graphical user interface and integrates parameter setting, experiment logging and operation visualization including pipette advancement, neuron detection/verification and electroporation.

### 2.2.3 *In vitro testing*

Dual patch experiments were performed on single cells in mouse brain tissue slices. One pipette was used in a whole-cell configuration to assess the quality and health of the cell and a second patch pipette was used in a cell-attached configuration to record extracellular action potentials and deliver a fluorescent dye.

Acute brain slices were prepared from adult (P50-P180) C57BL/6 mice using the protective recovery method described in detail elsewhere (Ting, Daigle et al. 2014).

Briefly, animals were heavily anesthetized with isofluorane and perfused trans-cardially with NMDG solution containing (in mM): 93 N-methyl-D-glucamine (NMDG), 2.5 KCl, 1.2 NaH<sub>2</sub>PO<sub>4</sub>, 30 NaHCO<sub>3</sub>, 20 HEPES, 25 Glucose, 5 Na-ascorbate, 3 Na-pyruvate, 10 MgSO<sub>4</sub>·7H<sub>2</sub>O, 0.5 CaCl<sub>2</sub>·2H<sub>2</sub>O (pH titrated to 7.3-7.4, osmolarity: 300-310). Mice were quickly decapitated, the brain was extracted, embedded in 2% agarose and cut into 300 µm coronal slices using a VF200 compresstome (Precisionary Instruments) in the cutting solution. The slices were incubated at 34 °C in the cutting solution for 10-12 minutes. They were then transferred to a recovery solution containing (in mM) 92 NaCl, 2.5 KCl, 1.2 NaH<sub>2</sub>PO<sub>4</sub>, 30 NaHCO<sub>3</sub>, 20 HEPES, 25 Glucose, 5 Na-ascorbate, 2 Thiourea, 3 Na-pyruvate, 2 MgSO<sub>4</sub>·7H<sub>2</sub>O, 2 CaCl<sub>2</sub>·2H<sub>2</sub>O (pH: 7.3-7.4, osmolarity: 300-310) for at least

60 minutes prior to beginning recording. Recordings were performed at room temperature (25 °C) in an open bath chamber (RC-29, Warner Instruments) with standard recording solution containing (in mM): 124 NaCl, 2.5 KCl 1.2 NaH<sub>2</sub>PO<sub>4</sub>, 24 NaHCO<sub>3</sub>, 5 HEPES, 12.5 Glucose, 2 MgSO<sub>4</sub>·7H<sub>2</sub>O, 2 CaCl<sub>2</sub>·2H<sub>2</sub>O. The liquid junction potential was corrected in the bath above the cell.

Whole-cell patch-clamp electrodes were pulled from filamented borosilicate glass tubes (BF150-86-10, Sutter Instruments) using a P-1000 micropipette puller (Sutter Instruments) to a resistance of 4-8 MΩ. Internal solution contained (in mM): 20 KCl, 100 Na-gluconate, 10 HEPES, 4 MgATP, 0.3 Na<sub>2</sub>GTP, 7 phosphocreatine-Tris, with pH adjusted to 7.4 and osmolarity adjusted to 290 mOsm.

Cell-attached electrodes were pulled from the same stock glass as whole-cell patch-clamp electrodes and filled with standard recording solution including 4% w/v Alexa Fluor 594 (A-10438, Life Technologies) to visualize the results of electroporation.

Brain slices are visualized using low-magnification (4×) and high-magnification (40×) water-immersion objectives. Manual guidance of the pipettes to the cell of interest was accomplished by inspection of the output of CCD camera (Rolera E-MC<sup>2</sup>) using the Micro-Manager (also μManager) software plugin for the ImageJ suite. A motorized three-axis microscope stage and three-axis patch-clamp pipette manipulator (Scientifica SliceScope Pro 1000; Scientifica Ltd.) were used to position the cell and pipettes under the field of view of the objective. A pipette holder is connected to the headstage of a patch-clamp amplifier (Multiclamp 700B). A headstage is mounted on each of the pipette manipulators. A data acquisition board (e.g., Digidata 1550A; Molecular Devices) relays the electrical signal from the amplifier to the computer for processing and storage. Resistance

measurement was performed using an embedded DAQ and pressure control was performed using a series of pneumatic regulators inside of an Autopatcher box (Neuromatic Devices)

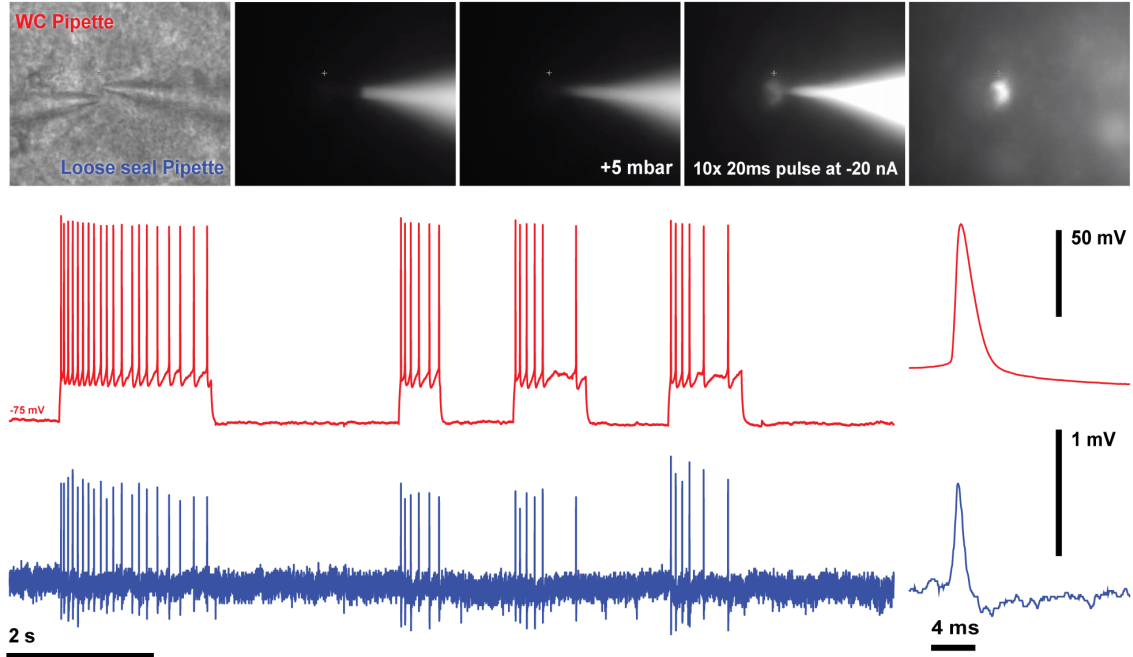


**Figure 3:** In vitro dual patch recordings to confirm electrophysiology and morphology of single cells can be recovered using cell-attached pipettes. Red trace: patch pipette in current clamp mode. Current was injected to bring the membrane to threshold and fire action potentials. Blue trace: the action potentials were recorded on the cell-attached patch pipette. Following the electrophysiological recording, slight positive pressure was applied to the cell-attached patch pipette and then current was injected via the current-clamp head stage (10x 20ms pulses at -20 nA).

Both patch pipettes were first visualized and brought to a region above the cortex of the brain slice under 4X magnification. They were then brought above the cell of interest under 40X magnification. First, the whole-cell pipette was brought into contact with the cell, as indicated by a dimple on the membrane, caused by the low-positive pressure expulsion of intracellular solution, which was visible on the video, an increase in pipette resistance of 0.1 M $\Omega$  or greater. A gigaseal was formed by release of positive pressure and application of gentle suction (-30 mbar) using a custom-built pressure control VI, which interfaced

with the Autopatcher control box. Break-in was performed by rapidly switching between high-vacuum (-340 mbar) and atmospheric pressure for brief periods of time (50-100 msec). When a whole-cell configuration was established on the first pipette, the second, cell-attached patch pipette was carefully positioned on the surface of the same cell and positive pressure was released as before, however no suction was applied to increase the seal resistance.

Current was injected in current-clamp mode using the whole-cell pipette to induce the firing of a series of action potentials, which were detected on the cell-attached pipette. The fluorescence of the Alexa-594 was then imaged to visualize the progress of the electroporation. A 1s current pulse train (10x -20nA pulses at 20 ms pulse width) was applied to the cell-attached patch pipette to induce the dielectric breakdown of the cell membrane via electroporation, and the ingress of the fluorescent dye into the cell was observed. The cell-attached patch pipette was retracted in 2 $\mu$ m steps to prevent damage to the cell. When the cell-attached pipette was removed, the whole-cell pipette was used to measure the membrane resistance, an indicator of cell health.

## **2.3 In vivo testing**

### *2.3.1 Surgical preparation*

All experiments were performed in accordance with the Institutional Animal Care and Use Committee (IACUC) guidelines at the Allen Institute for Brain Science and Georgia Tech.

Mice were anesthetized with Isoflurane (1–1.5% in O<sub>2</sub>) and placed onto a stereotaxic device (Kopf). Body temperature was monitored and maintained at 37 °C with a feedback-



controlled animal heating pad (Harvard Apparatus, USA). With aseptic surgical procedures, a circular craniotomy (~1 mm in diameter) was performed over the primary visual cortex (V1) centered on 1.25 mm anterior and 2.25 mm lateral to the Lambda. The dura was carefully retracted using a 31-gauge needle to facilitate the penetration of the glass micropipettes. Then the craniotomy was covered with sterile ACSF. A thin layer of low-melting point agarose (1%, Sigma-Aldrich) was applied over the craniotomy. The mouse was transferred to the experiment set-up for electrophysiology/electroporation. During the entire course of imaging/recording, animals were kept warm and appropriately anesthetized. Depth of anesthesia was monitored with periodic application of a toe pinch. If a foot withdraw reflex was observed, anesthesia was increased until it was no longer present.

#### 2.3.1.1 Clog check

Patch pipettes were suitable for re-use after trials if they were not clogged. Clogs were identified by a step resistance increase from the initial pipette resistance measured on the first trial with a given pipette. Another indicator of a clogged pipette was the absence of a visible plume of Alexa Fluor 594 (visible under low magnification with a stereoscope) when the pipette was retracted above the brain surface and placed under high positive pressure at the end of each trial. Clogged pipettes were manually replaced.

#### 2.3.1.2 Regional pipette localization

The region of interest for this study was layer 5 of the mouse visual cortex (V1). Pipettes were positioned vertically above the craniotomy at the beginning of each trial. Penetrations were done in a grid with sufficient spatial separation ( $\sim 200\ \mu\text{m}$ ) between attempts to facilitate the identification of labelled neurons. Pipette resistances were measured and rejected if they were outside of a range set by the user (here, 4-8  $\text{M}\Omega$ ). Rejected pipettes were retracted from the craniotomy and replaced manually. Pipettes that passed this initial resistance check were inserted into the brain at  $250\ \mu\text{m/s}$  under high positive pressure (500-800 mbar) to a depth set by the user (here,  $600\ \mu\text{m}$ ). Following insertion to the region of interest, the pressure in the pipette was reduced to low positive pressure (30 mbar) and pipettes were again checked for clogs. Clogged pipettes were defined by a pipette resistance increase of  $250\ \text{k}\Omega$ . Clogged pipettes at this stage were retracted to the brain surface and manually replaced. Trials with unclogged pipettes proceeded to the neuron hunting stage.

#### 2.3.1.3 Cell-attached formation

Similar to our previously published work, the robotic platform searched linearly for cell soma in  $2\ \mu\text{m}$  steps. Following each step, the resistance was measured and the presence of a cell proximal to the pipette tip (a neuron detection event) was defined as a monotonic increase in pipette resistance of  $0.2\ \text{M}\Omega$  over 3 steps. The forward motion of the pipette was then stopped, and the resistance of the pipette was measured for 10 seconds. If the pipette resistance decreased during the 10 second wait time, the pipette would return to the neuron hunting stage. If the pipette resistance did not decrease, the formation of a cell-

attached configuration was attempted. The pipette pressure was switched from low positive pressure to atmospheric pressure. After 30 seconds, the pipette resistance was measured, and the seal resistance was determined by subtracting the initial pipette resistance. Following the formation of a cell-attached patch, the activity of a cell could generally be recorded. During the recording period, putative cell type could be determined by an injection of current (50, 100, 150, 200 nA) for 5 ms. If no action potentials were elicited at a given current level, the current was increased until action potentials were elicited. The membrane potential was monitored to confirm that break-in did not occur during the recording procedure.

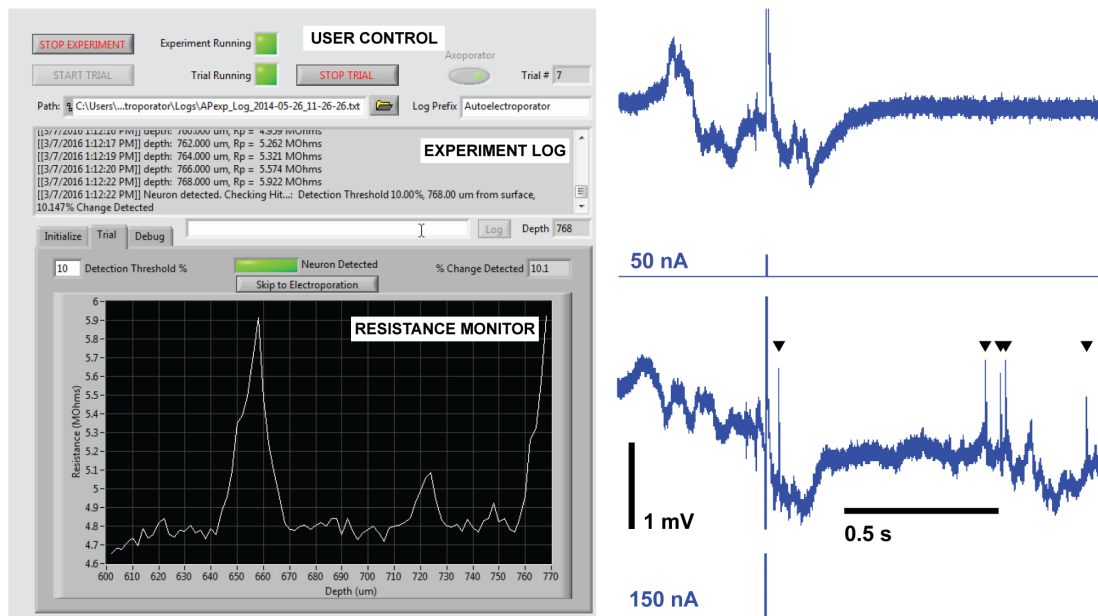


**Figure 4:** Graphical User Interface (GUI) of the automated electroporator program with example recordings. GUI includes controls for the user to override aspects of the automated operation, as well as an experiment log that is saved to disk for future processing, and a resistance monitor to inspect the progress of the neuron hunting stage. Stimulation and identification of nearby neurons is performed manually. The user manually scales and applies brief current pulses to elicit action potentials in current clamp mode using the Multiclamp Commander control panel. An example of this process is seen above. The initial current injection of 50 nA for 20 ms did not elicit action potentials, but the second current injection shown here at 150 nA did elicit action potentials, marked with arrows.

#### 2.3.1.4 Delivery of genetic material to single cells

Our initial design for a robotic platform to perform both electrophysiology and electroporation of single cells *in vivo* included a both a patch-clamp head stage and electroporation headstage. Connection between these headstages and the pipette electrode was controlled with a double-pole, double-throw (DPDT) switch mounted to the pipette holder and energized by a digital output from the embedded DAQ in the Autopatcher box. We demonstrated the use of this headstage switch to electroporate cells in the living brain and deliver DNA plasmids encoding GFP (details below). When the switch was triggered, the Axopatch was used to deliver 500  $\mu$ s pulses at 50 Hz for 0.3–2 s duration at various amplitudes between -10 and 12 V.

#### 2.3.1.5 Visual stimulus

For visually evoked responses, whole-screen drifting gratings were presented with a calibrated LCD monitor on the contralateral side showing 8 orientations (45° increment), 3 spatial frequency (0.02, 0.04 and 0.08 cycle per degree) and 1 temporal frequency (2 Hz).

#### 2.3.1.6 Retraction of the pipette

Following recording and electroporation, the pipette was slowly retracted (2  $\mu$ m/s) under low positive pressure (40 mbar) for 100  $\mu$ m to ensure that the cell and its processes would not be disturbed. The pipette was then rapidly retracted to the surface of the brain (250  $\mu$ m/s) and another trial was attempted.

#### 2.3.1.7 Histology and imaging

At the conclusion of the experiment, the craniotomy was covered with silicone (Kwik-cast) and mice were permitted to recover from anesthesia. The recovered animals incubated the electroporated plasmids for 4–7 days before they were sacrificed for histological analysis. The animal was transcardially perfused with 4% paraformaldehyde (PFA) in chilled saline and the brain was removed from the skull. The brain was post-fixed overnight in 4% PFA then transferred to 10% sucrose until it sank. Coronal sections (100  $\mu$ m) were prepared using a microtome. Sections were mounted using VectaShield and imaged using a Leica SP8 confocal microscope. Native fluorescence image Z-stacks were collected with either a 10  $\times$ , 0.4 NA dry, 20  $\times$  0.85 NA oil-, 40  $\times$ , 1.3 NA oil- or 63  $\times$ , 1.4 NA oil-immersion objective at 2  $\mu$ m step size. For revealing morphological detail, Z-stacks were tiled to cover the dendritic arbour across adjacent slices. These stacks were stitched using an ImageJ stitching plug-in and aligned with the Vaa3d software ([www.vaa3d.org](http://www.vaa3d.org)). Images of the larger field of view were taken with a 10  $\times$ , 0.4 NA dry objective.

The health of electroporated neurons was assessed by histology. In brief, brain tissue containing labelled neurons was carefully inspected for possible tissue damage, as we have shown in Figure 6, and 4',6- diamidino-2-phenylindole (DAPI) staining was conducted to examine the brain slices for possible neuronal necrosis.

### 2.3.2 *Data analysis*

For each experiment, we extracted the time, depth, pipette resistance ( $R_p$ ), and type of operation from the corresponding data log.

For electroporation only experiments, because no neuron verification by current injections was done, the success rate was calculated for each experiment as the ratio between the number of penetrations with a neuron recovered and total number of penetrations.

For electroporation + ephys experiments, the success rate was calculated for each experiment as the ratio between the number of penetrations with a neuron recovered and the number of penetrations with a neuron verified (action potentials detected following current injection).

Brains showing signs of damage or infection were excluded from the analysis.

## 2.4 **Results**

### 2.4.1 *In vitro electrophysiology and electroporation*

In a pilot experiment, we determined that regular patch pipettes could be used in a cell-attached configuration to record from spiking neurons and deliver material to the intracellular space through patch headstage-mediated electroporation.

Electroporation in this experiment was performed by brief application of current injections in current-clamp mode. The initial pipette resistance ( $R_p$ ) was 6 M $\Omega$  and the cleft resistance ( $R_c$ ) was 12 M $\Omega$ . The voltage potential at the surface of the cell can be found using Ohm's

law where,  $V_{surface} = I_{inj}R_c$ . For a current injection of -20 nA, the surface potential at the cell is -0.24 V. This is approximately the voltage that has been shown to induce electroporation *in vitro* previously (Akinlaja & Sachs, 1998).

When the electroporating current pulse was applied, dye visibly diffused into the cell, as shown in Figure 3. We therefore expect that similar application of current would enable the delivery of small molecules and plasmids to the recorded cell, and permit electrophysiological and morphological measurements using standard patch clamp equipment.

Finally, To determine the feasibility of cell-attached recording for *in vivo* recordings of visually evoked activity and cell identification, we calculated the SNR of the cell-attached recording obtained *in vitro*, similar to Kim and McNames (S. Kim & McNames, 2007):

$$SNR = \frac{\sigma_s^2 - \sigma_n^2}{\sigma_n^2}$$

where  $\sigma_s^2$  is the variance of spike segments in the recording and  $\sigma_n^2$  is the variance of noise segments of the recordings. Spike segments are defined as the portions of the recordings between 1 ms prior to and 6 ms after each spike peak. These segments contain both the spikes and the background noise. Noise segments are defined as the remaining portions of the signal with only background noise. The SNR of the recording was 19.5 ( $\sigma_s^2 = 0.0827$ ,  $\sigma_n^2 = 0.004$ ), similar to cell-attached recordings in literature, even in *in vivo* preparations (Gong et al., 2015).

#### 2.4.2 *In vivo electrophysiology and morphology*

In this study, 9–15 attempts per animal were conducted per mouse in the primary visual cortex, V1. Neurons detection events were triggered quickly ( $5 \pm 3$  min), measured from the beginning of the trial with the pipette above the brain. On average, the robot searched for 124  $\mu\text{m}$  before triggering a neuron detection event (neuron hunt distance was roughly poisson distributed, see Figure 5). In 86% of the neuron detection events, spontaneous or current evoked spikes were observed following a neuron detection event ( $n=269/311$ ). A visual stimulus of drifting gratings was delivered during the recording of 10 cells, which were held in a cell-attached state for  $17.0 \pm 3.8$  min on average. Overall, 31 neurons were labeled in this work, 11.5% of all successful neuron detection events (Figure 6). Electroporation attempts were considered successful if a neuron was detected during the histological procedures by native fluorescence. This success rate is comparable to yields reported by manual electroporation labeling experiments *in vivo* (Dempsey, Turner, Le, Sun, Bou Farah, et al., 2015; Joshi & Hawken, 2006; Oyama et al., 2013). The brain tissue immediately surrounding the recording and electroporation site was determined to be healthy following recovery from surgical and experimental procedures. In one experiment, the brain slice containing the natively fluorescing neuron was stained with DAPI and compared to a distal region. There was no necrosis observed around the recording site.



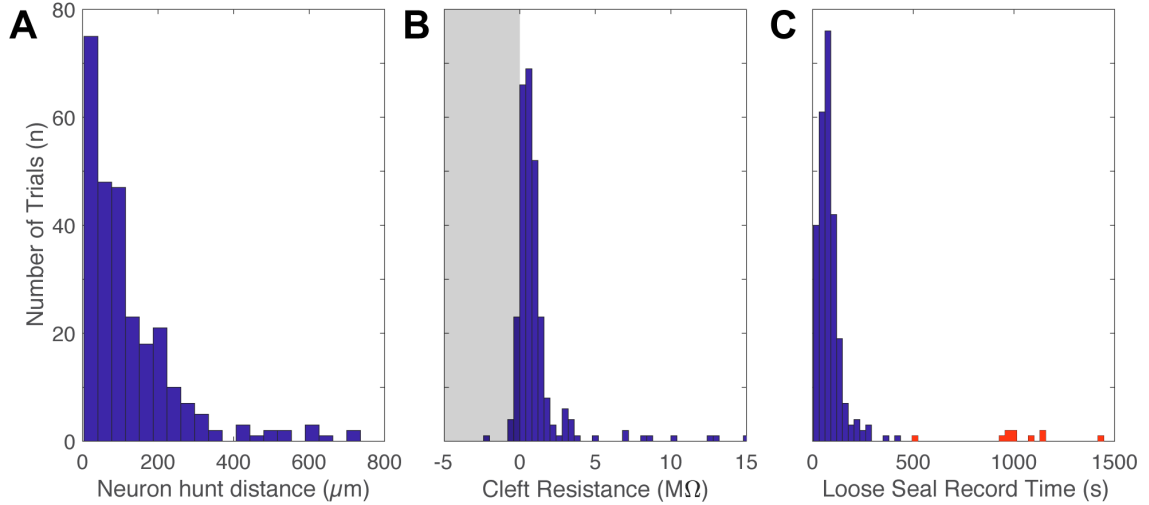


**Figure 5:** Results of log file data from autoelectroporator experiments (n=26). A) Neuron hunting distance (mean = 124  $\mu\text{m}$ ). B) Cleft resistance calculated after a ‘hit’ was detected during neuron hunting. Cleft resistance was calculated as the ‘hit’ resistance  $R_{\text{hit}}$  subtracted from the resistance when the pipette was switched to atmospheric pressure,  $R_{\text{atm}}$  (M $\Omega$ ). Shaded region indicates resistances less than 0 M $\Omega$ , indicative of pipette clogs, which were rejected (n=27). Rejected pipettes were retracted to the surface of the brain. C) Recording times following cell-attached patch formation. Red boxes recordings where visual stimulus was presented (n=10)

## 2.5 Discussion

The work presented here demonstrates that it is possible to perform rapid, automated, and standardized experiments to collect data from single cells in the living brain on a number of axes (electrical, physiological or sensory response, and morphological) using the cell-attached patch clamp configuration. This configuration confers several benefits over whole-cell patch clamping. The first benefit is that it does not require a gigaseal, and is therefore easier to perform, even deep in the cortex (up to 1200  $\mu\text{m}$  in this study, (Rancz et al., 2011)). Because the pipette does not need to form a gigaseal to record suprathreshold activity, it may be rapidly reused without the need to replace or clean the electrode after each seal attempt (irrespective of the successful formation of the gigaseal), as is required for whole-cell trials. The second benefit is that the cell-attached patch does not require

rupturing the membrane, the failure of which is deleterious to the cell health. Third, we have shown that manual (and, presumably, automated) identification of putative cell type by inspection of evoked action potential patterns is possible, which allows for the user to bypass a patched cell in search of a specific cell type he or she desires. Additionally, this configuration confers benefits over visually guided methods in that it does not require prior labeling of cells (Margrie et al., 2003a), nor does it require expensive two-photon optical systems (Judkewitz, Rizzi, Kitamura, & Häusser, 2009; Kitamura et al., 2008). Rather, we demonstrate *in vitro* that cells can be recorded and electroporated using headstages and amplifiers already present in most electrophysiology labs. Finally, because optical methods are restricted to superficial brain regions, this method is uniquely positioned to record from and label cells in subcortical nuclei.

Another benefit of this system over similar methods that have previously demonstrated the acquisition of electrophysiology and morphology from single cells *in vivo* (Dempsey, Turner, Le, Sun, Bou Farah, et al., 2015; Joshi & Hawken, 2006; Kitamura et al., 2008; Oyama et al., 2013; Rancz et al., 2011) is that it does not require a skilled operator and can be run semi-autonomously. At this point, the user's input is only required to determine if the pipette is clogged at the beginning of the trial and to identify the putative cell type following cell-attached acquisition (a procedure that may be automated in the future, see below). Additionally, there is great benefit conferred by the standardization of patch clamp trials. There are many anecdotes surrounding this technique for pipette pulling and inspection, cell detection and approach, etc., each differing lab-to-lab. Reducing this process to an algorithm removes variability introduced by humans and allows results to be directly comparable between labs. A demonstration of this standardization is present in the Allen Institute's Allen Cell Types Database, (<http://celltypes.brain-map.org>). Although this

data was collected manually through considerable effort, the standardized method used to produce the database allows electrophysiologists anywhere in the world to reproduce their results, or confidently compare their own results to the database.

One important contribution of this work has been the development of automated patch clamping algorithm with a finite-state machine (FSM) architecture. The original Autopatching software platform (available at <http://autopatcher.org>) utilizes a flat structure that, while successful at its original task, is difficult to extend with new capabilities. This work and other work from the Forest lab (Kodandaramaiah et al., 2016; Kolb et al., 2016; Li et al., 2017; Stoy et al., 2017; Wu 吴秋雨 et al., 2016), utilizes this updated architecture. This architecture lends itself well to the patch clamping process, which consists of stages such as regional pipette localization, pipette checking, neuron hunting, seal formation, breaking in, recording, etc. Because each step is encapsulated in an FSM, new states can be easily added and the logic that links states together is easily updated. This enabled close collaboration of Lu Li, Ben Ouellette and me to iteratively re-design the system to best suit the needs of the Allen Institute.

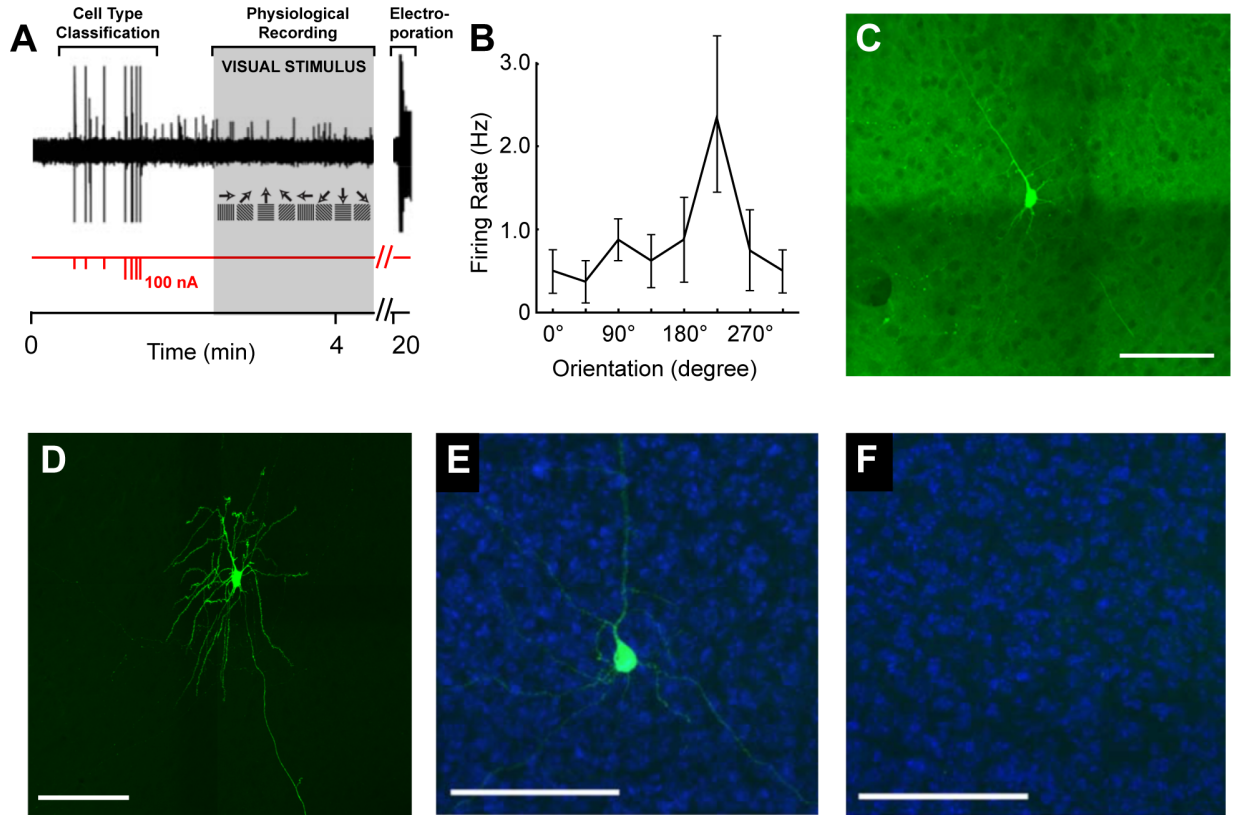


**Figure 6:** Automated electroporation results. A-C: The system was used to identify and classify neurons in the mouse visual cortex (V1). In this case, the cell was encountered 598  $\mu\text{m}$  below the pial surface, visual drifting gratings were presented, and EGFP plasmids were delivered via electroporation. A) The timeline of events. First, the cell was stimulated with increasing current injection pulses until action potentials were detected. Then visual stimulus was triggered and delivered for approximately 12 minutes. Finally, the cell was electroporated using the Axoporation via the custom headstage switch described in 2.3.1.4 (red trace is current injection). B) Orientation tuning plot for the recorded neuron. The cell is maximally responsive at 225°. C) EGFP fluorescence recovered following a 4-day recovery period. D) Another example neuron recorded, electroporated, and imaged by the author. E) EGFP fluorescence from a recorded neuron with background DAPI staining (blue) to test for cell health following a 4-day recovery period. F) DAPI stain of distal region from recording site. No chronic damage or necrosis is observed by the operations of the automated electroporator. Scale bars: 100  $\mu\text{m}$ . Data in A-C and E,F were collected by collaborator Ben Ouellette using the software and hardware designed by the author.

Future work could be devoted to full automation of this platform by algorithmic cell type identification. Specifically, the pattern of evoked action potentials recorded on the cell-attached patch pipette could be cross-referenced to the suprathreshold activity recorded in the Allen Institute's Cell Types Database. Additional experiments would need to be performed to confirm correspondence of activity evoked via current injection from the whole-cell and loose-patch configurations. If no correspondence is possible, a similar database of putative cell types can be constructed by *in vitro* targeted loose-patch recordings of visually identified cells. As we have demonstrated, the signal to noise ratio of cell-attached patch recordings is very high (~20). At signal-to-noise ratios in this range, we imagine that detection of neurons and their putative cell type will be possible in a closed loop fashion. Specifically, one could iteratively increase the amplitude or duration of positive current pulses using the ActiveX control for the Multiclamp Commander amplifier control panel until spikes are automatically detected using well-established methods (S. Kim & McNames, 2007; Lewicki, 1998; Obeid & Wolf, 2004).

# **CHAPTER 3.     ROBOTIC NAVIGATION TO SUBCORTICAL NEURAL TISSUE FOR INTRACELLULAR ELECTROPHYSIOLOGY IN VIVO**

Note: Portions of this chapter have been previously published (Stoy et al., 2017)

## **3.1 Introduction**

In vivo patch clamp recording is one of the most important and versatile techniques in neuroscience. Whole-cell recordings have enabled stable investigation of subthreshold activity to identify cell types and circuits in the intact brain. This technique is also uniquely positioned to enable concurrent measurements of intrinsic and sensory evoked electrophysiology in either voltage- or current-clamp modes (Constantinople & Bruno, 2013; Harvey, Collman, Dombeck, & Tank, 2009), morphology (Margrie et al., 2002), and the genetic profile of single neurons (Cadwell et al., 2016), as well as the ability to introduce foreign genetic material into the cell (Rancz et al., 2011; Vélez-Fort et al., 2014). There is growing interest in multimodal cell type classification (electrophysiological, morphological, and/or genetic, etc.) throughout the brain, a major goal of the BRAIN Initiative (Bargmann, Newsome, & Anderson, 2014). Though recently developed genetic voltage indicators have been used with some success to measure activity both from individual neurons and populations (Lin & Schnitzer, 2016), the heterogeneous tissue of the brain acts as a scattering medium, limiting recordings to superficial cortical layers in the mammalian brain. Sharp intracellular recording techniques similarly have sub-threshold resolution, but suffer from short recording times (Fee, 2000) and are unsuitable for voltage-clamp recordings due to high electrode impedance.

While whole-cell patch clamping is the gold standard for *in vivo* electrophysiology, it requires skill to perform and has thus been more extensively used for *in vitro* experiments. Recent efforts to automate it have been productive, yet sub-cortical recording with whole-cell patch clamping remains a low yield endeavor. Published papers are scant (Brecht & Sakmann, 2002; Groh et al., 2014; Margrie et al., 2002), but whole-cell recordings in deep subcortical nuclei are difficult to obtain and are known to suffer from increased access resistance (Margrie et al., 2002). In a literature review of the 60 most cited papers that reported low access resistance, blind, whole-cell recordings *in vivo*, only 5% of all 2350 recorded cells were recorded at depths exceeding 3 mm from the pial surface in rodents. Several other studies have demonstrated recordings in the cat thalamus *in vivo* (several centimeters below the pial surface), but report high access resistance of the electrodes (Xin Wang et al., 2007; Xin Wang, Vaingankar, Sanchez, Sommer, & Hirsch, 2011).

To investigate these subcortical nuclei *in vivo*, researchers have used extracellular, juxtosomal, cell-attached, or sharp intracellular recordings (Friedberg, Lee, & Ebner, 2004; Higley & Contreras, 2007; Petersen et al., 2008; Polack & Charpier, 2006; Q. Wang, Webber, & Stanley, 2010; Yu, Xiong, Chan, & He, 2004b, 2004a), indicating that deep whole-cell recordings, while valuable and desirable, are exceedingly difficult to obtain. In order to enable this important technique to be used throughout the brain, we identify a need to improve both the yield and quality of deep whole-cell recordings.

It is well known that a pipette must be clean, with a good tip geometry, to enable formation of a gigaseal with a target cell (Neher, 1995). Since deep recording requires traversing through several millimeters or centimeters of heterogeneous tissue (e.g., blood vessels, glial cells, membranes) to reach a region of interest during regional pipette localization

(RPL), the pipette invariably encounters, and is clogged by debris from this tissue. Effort to date to mitigate this problem have had limited success. In their 2002 study, Margrie et al. suggested that increasing pipette pressure or advancing the pipette through a guide tube may reduce access resistance (or equivalently, increase quality) (Margrie et al., 2002). However, Brecht and Sakmann subsequently noted that neither higher pressures nor a guide tube reduced the access resistance of thalamic recordings (Brecht & Sakmann, 2002).

We set out to investigate the relationship between this troublesome first stage of patch clamping, regional pipette localization, and high access resistance, low yield whole-cell experiments. By attempting whole-cell trials in the mouse thalamus, a deep brain structure of wide interest (Kelly et al., 2014; Llinás & Steriade, 2006; Sherman, 2005), we observed that transient high amplitude fluctuations in resistance that occur during regional pipette localization are often followed by residual, permanent increases in pipette tip resistance, preventing successful whole-cell recordings, and that these obstructions could be avoided with a series of small lateral movements, confirming previous observations by Lee et al. 2014 (D. Lee et al., 2014). By visualizing this process using slices of brain tissue on a microscope, we show that pipette penetration of blood vessels and the residue left on pipette tips is the likely cause these resistance changes, along with meninges (dura, pia, and hippocampal meninges). Lateral steps enabled navigation around blood vessels and other obstacles without a residual increase in resistance and meninges were penetrated with short, rapid plunges with the pipette. We developed an efficient algorithm for laterally moving around obstructing blood vessels during regional pipette localization *in vivo* and compared its effectiveness to linear localization. We found that whole-cell trials performed 3 mm deep could be localized with the same yield as we had previously demonstrated in



the cortex (up to 1 mm) with direct linear localization and in addition, had comparable access resistances to whole-cell recordings performed previously in the cortex.

## **3.2 Methods**

### *3.2.1 Acute in vivo and in vitro preparation*

All experiments were performed in accordance with the Georgia Tech Institutional Animal Care and Use Committee (IACUC) guidelines. For *in vivo* preparation, all mice (n=19) were prepared for acute experimentation as we have done previously (Kodandaramaiah et al., 2012). Briefly, young male C57BL/6 mice (p35–p49) were anesthetized with isoflurane and headfixed to a titanium headplate with C&B-Metabond dental cement (Parkell, Edgewood, NY). Craniotomies (1 mm diameter) and duratomies were performed above the Ventral Posteromedial nucleus (VPM) of the thalamus (1.75 mm Rostral, 1.75 mm Lateral, 3 mm below the pial surface) using stereotaxic coordinates from the Paxinos and Franklin mouse brain atlas (Paxinos & Franklin, 2012).

For *in vitro* preparation, acute brain slices of mouse visual area VI were prepared from male C57BL/6 adult mice (aged P30-P60) using the protective recovery method described in detail elsewhere (Wu 吴秋雨 et al., 2016).

### *3.2.2 Pipette fabrication*

Long taper patch pipettes (e.g., 7 mm) were pulled using fire-polished borosilicate glass (BF150-86-10HP, Sutter Instrument, Novato, California) on a P-1000 electrode puller with

a 4.5 mm wide box filament (Sutter Instrument). The long taper is achieved with an initial high-velocity step (heat = Ramp + 10, velocity = 40), with subsequent steps used to develop the taper to  $\sim 1 \mu\text{m}$  (3-4 pulls of heat = Ramp – 10, velocity = 20).

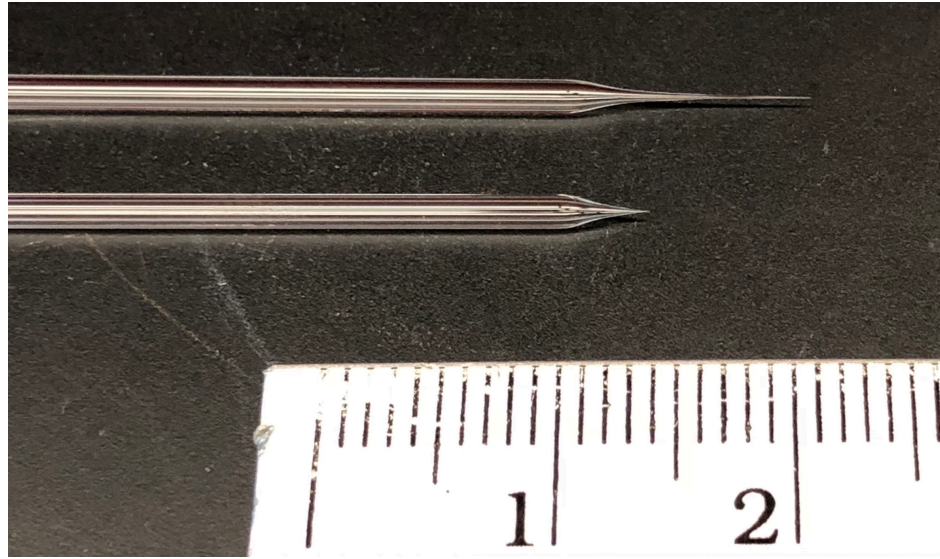


**Figure 7:** Comparison of pipettes used for thalamic patching (top) with conventional cortical patch clamp pipettes (bottom). Ruler is in centimeters.

### 3.2.3 Electrophysiology

Whole-cell patch clamping was performed as described previously (Kodandaramaiah et al., 2016). In brief, an Autopatch 1500 (Neuroromatic Devices, Atlanta GA) was used to provide computer-controlled pressure and measure resistance for both *in vitro* and *in vivo* experiments. Both *in vitro* and *in vivo* experiments used Multiclamp 700B amplifiers (Molecular Devices, Sunnyvale, CA) and signals were digitized at 20kHz using National Instruments DAQs (*in vivo* DAQ: cDAQ-9174 and NI 9215, *in vitro* DAQ: NI USB-6221, National Instruments, Austin, TX) and recorded in PClamp 10 (Molecular Devices). A Slicescope Pro 1000 (Scientifica, Essex, UK) was used to perform *in vitro* recordings and

an MP-285 micromanipulator (Sutter Instrument) with PT1-Z8 Motorized Translation stage (Thorlabs, Newton, New Jersey) was used for positioning the electrode for *in vivo* patch clamping.

Resistance measurements were performed throughout pipette translation, rather than only before and after translation as in our prior work (Kodandaramaiah et al., 2016, 2012). During pipette translation, starting from ACSF on the surface of the tissue, resistance was recorded by applying a 20 mV amplitude, 128 Hz square wave (50% duty cycle) to the pipette, and calculating the resistance using Ohm's law. The resistance was computed as a moving average of four measurements (low pass filter with four sample rectangular window). Thus, filtered resistances were saved to an array, called the resistance array.

#### 3.2.4 *Blood vessel penetration*

In addition to mapping a blood vessel in neural tissue using SICM, we measured the resistance changes encountered as the pipette was translated *through* a blood vessel *in vitro*. The pipette was filled with ACSF and pressured to high positive pressure (1000 mbar) to replicate typical parameters for *in vivo* pipette localization (Kodandaramaiah et al., 2016). For this penetration experiment, the pipette was positioned above a blood vessel visually, at 35° relative to the image plane. The pipette was manually lowered until the tip resistance increased by 12.5% above initial pipette resistance, and then retracted 15  $\mu\text{m}$  to a starting position. Resistance was recorded while the pipette was manually advanced for 200  $\mu\text{m}$  as described above. Images were captured at relative depths indicated using the optical system (See Figure 8b).

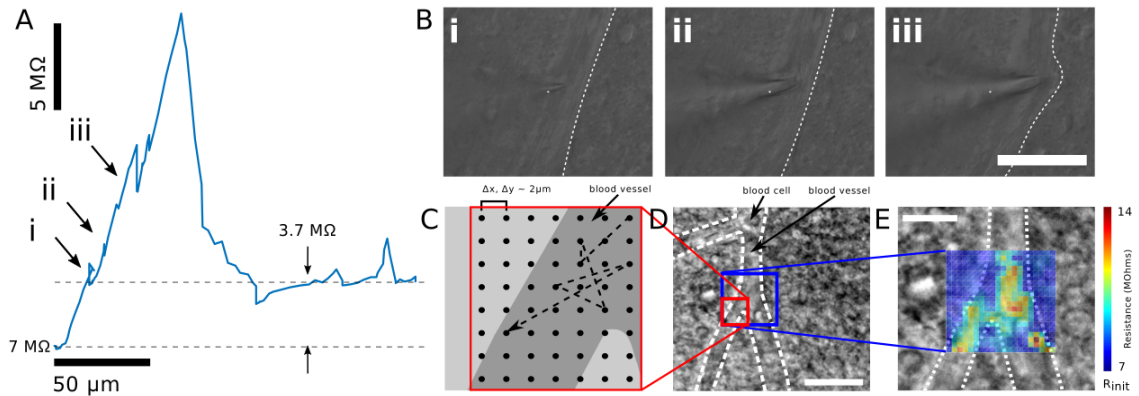


**Figure 8:** Lateral navigation around obstructions prevents persistent pipette resistance increase caused by penetration of blood vessels *in vitro*. A) Resistance trace as a function of distance as a pipette pierces a blood vessel under high positive pressure. A residual resistance increase of 3.7 MΩ remains after the vessel is punctured. B) IR DIC images showing the pipette encountering and deforming the blood vessel (scale bar, 50 μm). C) Schematic of Scanning Ion Conductance Microscopy (SICM) mapping of a blood vessel proceeds from a central point. Samples are collected randomly from a grid area 20 x 20 μm at 2 μm resolution D) The entire blood vessel and surrounding milieu is shown under IR DIC (scale bar, 20 μm) E) Resistances mapped as a function of grid position, clearly showing increased resistance when the pipette is above the blood vessel (scale bar, 10 μm, 2x interpolation)

### 3.2.5 Scanning Ion Conductance Microscopy *in vitro*

We mapped blood vessels in neural tissue (*in vitro*) by performing scanning ion conductance microscopy (Sánchez et al., 2008). The pipette was filled with Artificial Cerebrospinal Fluid (ACSF) and pressurized to low positive pressure (30 mbar). First, the pipette was centered above a blood vessel of interest and visualized using differential interference contrast (DIC) optical system (Olympus, Center Valley, PA). The pipette was manually lowered until the tip resistance increased by 12.5% above initial pipette resistance. The pipette was then retracted 15 μm and moved laterally to a new, random “grid position.” At this new position, the pipette was then moved down 15 μm and the tip

resistance was measured again. This process was performed repeatedly until all grid positions were measured. A grid is defined as a square  $20\text{ }\mu\text{m} \times 20\text{ }\mu\text{m}$  comprising 100 “grid positions” with  $2\text{ }\mu\text{m}$  pitch, centered on the initial pipette axial position. The resulting map of resistances as a function of lateral pipette position (at constant depth) was linearly interpolated to  $1\text{ }\mu\text{m}$  pitch for visualization and displayed in MATLAB (Natick, MA) as a surface plot (See Figure 8c).

### *3.2.6 Regional pipette localization in vivo*

Regional pipette localization (Kodandaramaiah et al., 2012) refers to the act of lowering a pipette into neural tissue to a desired region of interest (e.g., thalamus) under high positive pressure. In our experiments, we performed regional pipette localization using two different methods: an uninterrupted, direct, linear trajectory as we have previously described (Kodandaramaiah et al., 2012) and a novel robotic navigation method to avoid obstructions. The method of localization was randomly selected prior to each trial. A maximum of 10 electrode penetrations were performed per experimental preparation. Pipettes were initially placed on the brain surface under stereoscopic guidance in a region

free of large blood vessels.

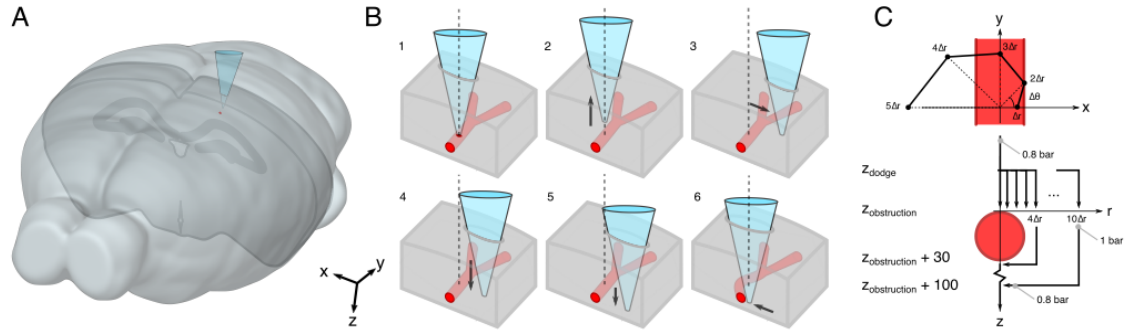


**Figure 9:** Robotic navigation algorithm for avoiding blood vessels during regional pipette localization *in vivo*. A) Schematic showing vascular avoidance preparation. Brain outline from the Allen Mouse Brain Atlas (Lein et al., 2007). B) Visual algorithm of vascular avoidance [1] Obstruction (here, a blood vessel) is detected by an increase in pipette resistance. [2] The pipette is retracted to  $z_{dodge}$ , [3] moved laterally, and [4] advanced to the original  $z_{obstruction}$ . If the difference in resistance at  $z_{obstruction}$  and the resistance at  $z_{dodge}$  is  $< 200 \text{ k}\Omega$ , [5] the pipette is advanced through  $z_{obstruction}$  and [6] the pipette is moved back to the original  $x$  and  $y$  axis. C) The pipette is navigated around a blood vessel with sequential steps sampling from a spiral pattern. Blood vessel in A and B shown in isometric view. Blood vessel in C shown in top view (top) and cross section (bottom).

### 3.2.6.1 RPL using linear trajectory

Linear regional pipette localization has previously been utilized by us (Kodandaramaiah et al., 2012) and others (Desai et al., 2015) for whole-cell electrophysiology *in vivo*. We used similar parameters; briefly, we applied high positive pressure (1000 mbar) and translated the pipette at a rate of  $500 \text{ }\mu\text{m/s}$ . Resistance was recorded during localization as described above, so the resistance array could be displayed and analyzed, at a pitch of  $500 \text{ }\mu\text{m/s} / 128 \text{ Hz} = 3.9 \text{ }\mu\text{m/sample}$ .

### 3.2.6.2 RPL using robotic navigation

For RPL using robotic navigation, high positive pressure (800 mbar) was applied and the pipette was translated at a rate of 200  $\mu\text{m/s}$ , unless otherwise stated. Resistance was recorded during localization as described above. At the square wave frequency of 128 Hz, resistance array measurements were spaced 1.6  $\mu\text{m}$  apart. The pipette was inserted along its initial axis,  $z$ , at  $x,y = (0,0)$  and moved in  $x$ ,  $y$ , and  $z$  to navigate around obstacles.

As shown in Figure 9, if an obstruction was detected during localization, motion was halted at depth  $z_{\text{obstruction}}$ , with a pipette resistance of  $R_{\text{obstruction}}$  (note Figure 9b1,c). An obstruction detection was defined as follows: pipette resistance increase of at least of 12.5% above baseline resistance. Baseline resistance,  $R_{\text{baseline}}$ , was computed as the minimum resistance of the previous 800  $\mu\text{m}$  (512 samples from the resistance array, 4 sec). With an initial pipette resistance of 4-7  $\text{M}\Omega$ , 12.5% increase resulted in a minimum  $R_{\text{obstruction}}$  of 4.5-7.9  $\text{M}\Omega$ .

After halting the motion of the pipette upon obstruction detection, the pipette is moved in a series of steps in an attempt to navigate around the obstruction. First, the pipette is retracted along the pipette axis ( $z$ ) by a distance  $z_{\text{dodge}}$  (See Figure 9b2,c). The distance  $z_{\text{dodge}}$  is located relative to  $z_{\text{obstruction}}$  within the previous 50  $\mu\text{m}$  (32 samples) at which a minimum pipette resistance,  $R_{\text{dodge}}$ , was recorded. At depth  $z_{\text{dodge}}$ , the pipette is moved laterally to dodge, or navigate around, the obstacle that was encountered (See Figure 9b3,c). Lateral movements, centered on the initial pipette axis are calculated to form a spiral (See Figure 9c), as follows:

$$m(n) = n\Delta r \cos(n\Delta\theta - \pi/4) \mathbf{i} + n\Delta r \sin(n\Delta\theta - \pi/4) \mathbf{j}$$

Where  $\Delta r = 5 \text{ } \mu\text{m}$ ,  $\Delta\theta = \pi/4$ , and  $n$  is the step index  $\{1, 2, 3, \dots\}$ . Each step,  $n$ , yields a lateral movement vector,  $m$ , along which the pipette is moved. The pipette is then lowered back to  $z_{\text{obstruction}}$  (See Figure 9b4,c). At  $z_{\text{obstruction}}$ , the resistance is measured again, termed  $R_n$ . If  $R_n - R_{\text{dodge}} \geq 200 \text{ k}\Omega$ , the obstacle is still in the proximity of the pipette tip and has not been avoided. The pipette is then retracted to  $z_{\text{dodge}}$ , the step index  $n$  is incremented, and another lateral movement occurs. This is repeated until  $R_n - R_{\text{dodge}} < 0.2 \text{ M}\Omega$  or until  $n=10$ , resulting in a maximum lateral distance of  $50\mu\text{m}$ .

If  $R_n - R_{\text{dodge}} < 200 \text{ k}\Omega$ , the obstacle has been successfully avoided. The pipette is advanced  $30 \text{ } \mu\text{m}$  beyond  $z_{\text{dodge}}$  to ensure the obstacle has been passed (See Figure 9b5,c), and then the pipette is moved laterally in a straight line from  $x,y = (m_i(n), m_j(n))$  to return to the initial pipette axis,  $x,y = (0,0)$  (See Figure 9b6,c).

Alternatively, if  $n=10$  and  $R_n - R_{\text{dodge}} \geq 200 \text{ k}\Omega$ , the obstacle was not avoided. In this case, a pulse of high positive pressure (1000 mbar, 1 sec) is applied while the pipette is advanced 100 microns at  $200 \text{ } \mu\text{m/s}$  to attempt to dislodge the obstruction from the tip of the pipette. The pipette is then moved laterally in a straight line to return to the initial pipette axis,  $x,y = (0,0)$  (See Figure 9c).

Localization is continued until the region of interest is reached and the pipette resistance is less than  $0.2 \text{ M}\Omega$  above the baseline resistance,  $R_b$ . If the obstruction is not cleared before the end of the region of interest, pipette localization is halted and the pipette is retracted to the surface and replaced.

Following successful regional pipette localization, the software compensates for pipette capacitance, which is expected to change due to the depth of the recordings discussed here.



### 3.3 Results

#### 3.3.1 RPL using linear trajectory

We have previously developed an automated patch clamping system, the Autopatcher, and deployed it in the cortex and hippocampus. The results for regional pipette localization, and yield are shown in Figure 10, top row, for depths less than 1 mm, reproduced from Kodandaramaiah et al. 2012.

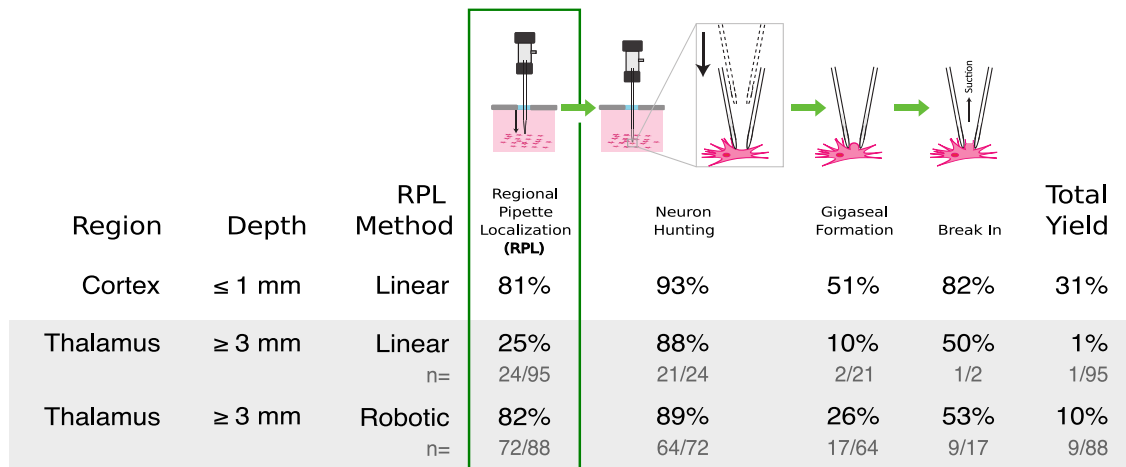


**Figure 10:** Increased yield of RPL during whole-cell patching *in vivo* with robotic navigation. In vivo whole-cell recording is a serial process consisting of Regional Pipette localization, Neuron Hunting, Gigaseal Formation, and Break-In. Whole-cell recording yield (Total) is a linear product of previous success rates. During traditional, linear localization, cortical (top row) and thalamic pipettes (middle row) are clogged in 1/5 insertions and 3/4 insertions respectively, preventing further steps. Gray box indicates procedures presented in this study. The percentage of pipettes that successfully performed regional pipette localization increased from 25% to 82% and total whole-cell yield increased from 1% to 10% when robotic navigation was performed. (top row data reproduced from Kodandaramaiah et al., 2012)

To explore the feasibility of using the Autopatcher for whole-cell recording in deep subcortical nuclei we targeted the ventral posteromedial (VPM) nucleus and surrounding nuclei of the thalamus. The resulting yield of whole-cell patching was far below what we

observed in our previous cortical patching efforts (See Figure 10, top and middle rows). In 95 trials, one successful whole-cell recording was achieved. Further, in 75% of trials (71/95), the pipette reached a depth of 3 mm with a tip resistance above the threshold for removal and replacement. Thus 75% of trials were aborted without attempting gigaseal formation.

To understand what was occurring during linear localization, we modified the Autopatcher so that, as described in the Methods, resistance measurement was performed throughout pipette translation, rather than only before and after translation as in our prior work. Consequentially, during linear localization multiple high amplitude fluctuations of the resistance were revealed, occasionally greater than 25 M $\Omega$  (Figure 11a,b). As the pipette advanced, resistance would often return near, but not exactly back to baseline, indicating that the event was transient. Final pipette resistance (at the depth of regional pipette localization) was on average 0.73 M $\Omega$  greater than the initial resistance measured above the pial surface (Figure 11e). High amplitude fluctuations were observed in 91% of linear localization trials (n=86/95) (Figure 11a).

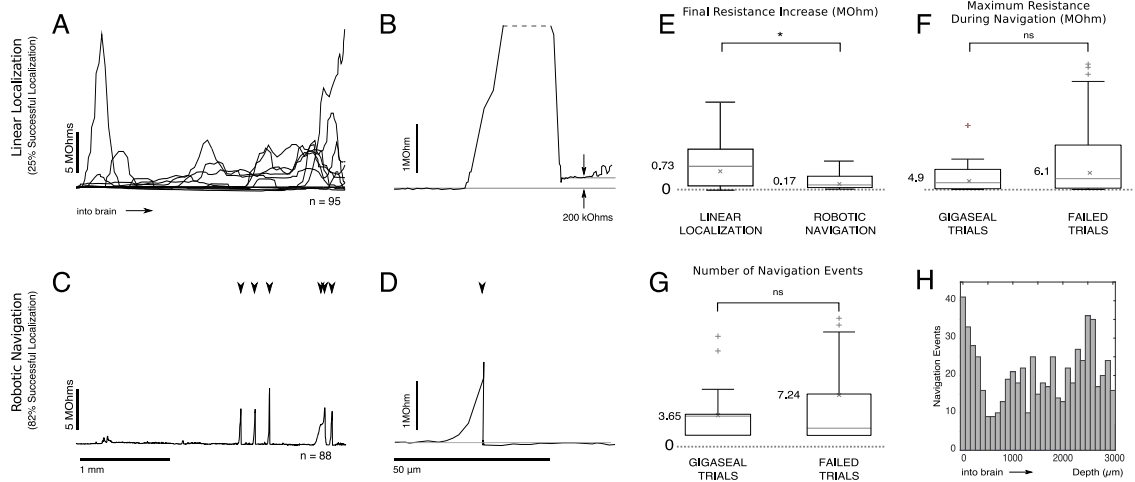


**Figure 11:** Pipette tip resistance increases during regional pipette localization *in vivo* due to accrued debris, preventing whole cell recordings. Robotic navigation prevents this debris from accruing. A) Recordings of change in pipette resistance during regional pipette localization reveal that obstructions are encountered throughout the insertion path. B) When an obstruction is cleared by continuing linear pipette advancement, debris may still be present at the pipette tip, reflected by the persistent resistance increase of the pipette by 0.200 MΩ. C) Using a robotic navigation algorithm, pipette debris is prevented from accruing on the pipette tip, shown by the return of the pipette resistance to the baseline. Arrows indicate locations of robotic navigation event. D) Detail of a single robotic navigation event. A-D) initial pipette resistance was subtracted to show changes in resistance. Initial pipette resistances ranged from 4-7 MΩ. E) The final resistance of the pipette is significantly lower after insertion to 3mm below the pial surface when the robotic navigation algorithm to localize the pipette was used. F) The maximum resistance measured during robotic navigation is not significantly different between trials that gigasealed successfully (n=17) and trials that failed to seal (n=71), Wilcoxon rank sum test (p=0.19). G) The number of navigation events was not significantly different between trials that gigasealed successfully (n=17) and trials that failed to seal (n=71), Wilcoxon rank sum test (p=0.96) H) Histogram showing number of navigation events as a function of depth. Note the slight increase in navigation events around 0 μm and 2500 μm from the pial surface, where the pia and ventricular meninges were encountered, respectively.

### 3.3.2 Observations of obstacles

To understand the nature of these high amplitude resistance fluctuations, we investigated them *in vitro* where we could visualize the interaction of the pipette tip with the neural tissue under a microscope. After applying the requisite high positive pressure (1000 mbar) to a patch pipette, we advanced its tip through the tissue. We noted that the high positive

pressure easily displaced neurons and glia, but some blood vessels remained in the path of the pipette. Shown in Figure 8a, as the pipette encountered one of these blood vessels during manual, axial translation at approximately 15  $\mu\text{m}/\text{sec}$ , the pipette resistance was measured at 10 Hz. The pipette resistance, initially 4.3  $\text{M}\Omega$ , increased to 26  $\text{M}\Omega$  within 35  $\mu\text{m}$  as the pipette deformed the blood vessel (Figure 8b). The resistance then quickly decreased as the pipette pierced and passed through the blood vessel. However, a residual blockage was noted, causing an increase in pipette resistance of 3.7  $\text{M}\Omega$  that persisted until the end of the tissue slice was reached (approximately 200  $\mu\text{m}$ ). The resistance signature of an obstruction *in vitro* appears qualitatively similar to resistance fluctuations encountered *in vivo* (Compare Figure 8a and Figure 11b)—a rapid increase in resistance, followed by a rapid decrease, resulting in a residual resistance offset.

The previous result showed the uniaxial ( $z$ ) signatures of a blood vessel encountered with a pipette. We also mapped blood vessels in neural tissue laterally ( $x,y$ ) by performing scanning ion conductance microscopy. As shown in Figure 8c-e, pipette resistance increases were observed over a region that overlapped with the microscopy image of the blood vessel. Concomitantly, regions of tissue adjacent to the blood vessel, populated by neural cells and glia, showed only negligible resistance increases. Additionally, without impaling the blood vessel, no residual increase in resistance was noted even after 100 consecutive resistance measurements. Thus, we gained confidence that a blood vessel was the predominant obstacle to pipette insertion in neural tissue and that it could be avoided by moving the pipette laterally even after initial contact if the vessel was not impaled.

### 3.3.3 Selection of navigation parameters

We used SICM to further optimize the parameters for encountering, and navigating around obstacles. We set a threshold for obstacle encounters of 12.5% (approximately 500 k $\Omega$ ); this is greater than the amplitude of baseline resistance variation during localization (100 k $\Omega$ ) but much less than observed during blood vessel impalement (See Figure 8a).

To determine the axial retraction distance necessary to attempt to dodge an obstacle,  $z_{\text{dodge}}$ , we first noted that the pipette can drag cells and blood vessels if it is positioned too close to an obstacle. We moved the pipette above a blood vessel and determined the minimum axial retraction distance required to allow a pipette to move laterally without dragging an obstruction to be 15  $\mu\text{m}$  (data not shown). We set a retraction distance of up to  $z=50 \mu\text{m}$  *in vivo* to ensure that the pipette was safely away from the obstacle before lateral motion, given that the *in vivo* environment is less predictable than *in vitro*.

We next attempted to optimize the axial advancement distance necessary to bypass an obstacle after lateral movement. Others have performed a rigorous study of blood vessels in the mouse brain, showing sizes of 10-60  $\mu\text{m}$  ((Santisakultarm et al., 2012), Figure 8c). From their data, we compute a mean blood vessel diameter of  $28.1 \pm 1.9 \mu\text{m}$ . In our observations, capillaries 15  $\mu\text{m}$  diameter and smaller were easily displaced under high positive pressure. We set a distance of 30  $\mu\text{m}$  to advance the pipette beyond the blood vessel location ( $z_{\text{obstruction}}$ ) to ensure the obstacle had been passed.

Whereas we used 1000 mbar for RPL during linear localization, we chose a lower pressure (800 mbar) for pipette insertion during robotic navigation to reduce the volume of ejected intracellular solution during the longer time needed to perform RPL.

To minimize damage to the tissue *in vivo*, we designed the vessel avoidance algorithm to make the smallest lateral and radial movements possible. Radial movement was defined as the distance between the pipette position  $(x_n, y_n)$  and the original pipette location at  $x, y = (0,0)$ . Lateral distance traveled was defined as the sum of the distances traveled between each point. Movements were made in small increments to minimize radial distance,  $r$ , traveled. Additionally, because the orientation of the blood vessel's major axis with respect to manipulator's  $x$  and  $y$  axes is unknown, we incremented the angle,  $\theta$  with each step resulting in a spiral search pattern. Similar search patterns have been shown to minimize path length when searching for a line in a 2D plane, analogous to finding the edge of a blood vessel in a plane (Finch & Zhu, 2005).

#### 3.3.4 RPL using robotic navigation

Using robotic navigation algorithm to avoid obstructions during regional pipette localization greatly improved the yield of successfully localized pipettes. In 88 trials, 82% of pipettes were localized successfully to a depth of 3000  $\mu\text{m}$  when the dodging algorithm was active (when compared to linear localization,  $n=95$ ,  $p=7.8448\text{e-}15$ , Fisher's exact test). This high yield for RPL using robotic navigation for the thalamus is comparable to rates achieved with RPL using linear trajectories in the cortex.

In addition, the final resistance increase (170  $\text{k}\Omega$ ,  $n=88$ ) was significantly lower than when the pipette was localized without the algorithm (730  $\text{k}\Omega$ ,  $n=95$ ,  $p=0.0142$ , Wilcoxon rank sum test) (See Figure 11de). During robotic navigation, obstructions were encountered in 95% of trials, and on average the dodging algorithm attempted to avoid 6.7 obstructions during each localization (See Figure 11c). At a depth of 3000  $\mu\text{m}$ , obstructions were

therefore encountered every  $3000/6.7=445$   $\mu\text{m}$  on average. Each obstruction that was successfully avoided in  $n=3.5$  steps, resulting in a radial distance of  $17.5$   $\mu\text{m}$  on average. Regional pipette localization under algorithmic guidance was completed in an average of  $75 \pm 23$  sec, significantly longer than 6 sec (3 mm at  $500$   $\mu\text{m/s}$ ) using the traditional localization method, due to the increased time to avoid obstacles and the lower localization speed. Advantageously, this slow localization may allow tissue to relax before attempting to patch.

The number of robotic navigation events did not have a significant effect on the success of gigasealing. Trials that resulted in a gigaseal ( $n=17$ ) underwent 3.65 navigation events on average, while trials that failed to result in a gigaseal ( $n=71$ ) underwent 7.24 navigation events on average ( $p=0.961$  Wilcoxon rank sum test). Additionally, the maximum resistance increase experienced by pipettes during localization did not have an effect on the success of gigasealing. Trials that resulted in a gigaseal ( $n=17$ ) had an average maximum resistance during localization of  $4.9$   $\text{M}\Omega$ , while trials that failed to result in a gigaseal ( $n=71$ ) had an average maximum resistance during localization of  $6.1$   $\text{M}\Omega$  ( $p=0.19$ , Wilcoxon rank sum test).

Vertical descent to the thalamus requires penetration of the ventricular meninges, large, relatively planar membranes that cannot be avoided using the algorithm described here. The meninges were routinely detected at approximately  $2.5$  mm from the pial surface (See Figure 11h). The meninges were penetrated using, on average, 2.3 successive dodge attempts (each resulting in a rapid  $100$   $\mu\text{m}$  advancement of the pipette).

The yield of whole-cell recordings in thalamus improved when regional pipette localization was performed using robotic navigation. In trials where whole-cell recordings were

attempted following RPL with robotic navigation, 10% of trials (n=9/88) resulted in successful whole-cell recordings. In trials performed using RPL with linear localization, 1% of trials (n=1/95) resulted in whole-cell recordings (p=0.0076, Fisher's exact test).

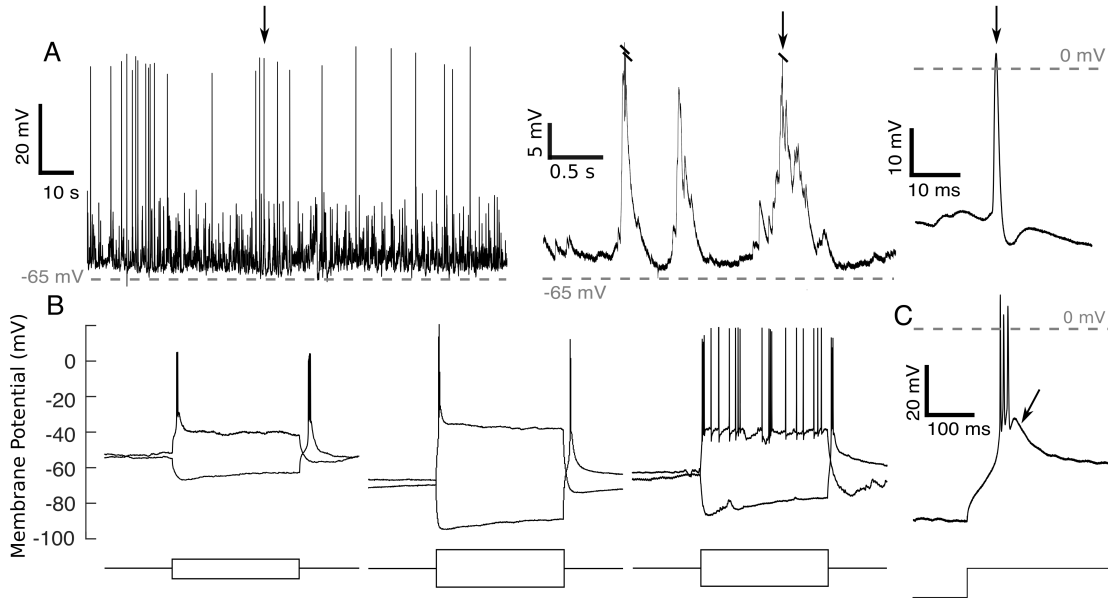


**Figure 12:** Neurons recorded in whole-cell configuration were of good quality. A) Example of spontaneous activity from a neuron recorded 3.2 mm below the pial surface with detail of spontaneous burst (arrow indicates burst shown in detail to the right). B) Example whole-cell traces recorded in the thalamus for 3 different neurons. Note the sag in membrane potential following hyperpolarizing current injection (representing activity of  $I_h$ , as described in (Leist et al., 2016)) and after-hyperpolarization rebound bursting in each trace, indicative of thalamic neurons. Current injections lasted 0.5 sec and ranged from - 50 pA (first recording) to - 100 pA (second and third recording). C) Following hyperpolarizing current injection, rebound bursts exhibited after depolarization (ADP, see arrow), consistent with ventrobasal thalamic nucleus cells (X. Wang et al., 2010b). Current injection was -150 pA.

Whole-cell recordings performed in the thalamus with robotic navigation were of comparable quality to those previously performed in the cortex using linear localization (See Figure 12, (Kodandaramaiah et al., 2012; Margrie et al., 2002)). Our thalamic recordings had similar access resistances ( $32.0 \pm 4.1 \text{ M}\Omega$ ) to cortical recordings reported by Margrie et al. 2002 as well as our prior work, all in the range of 10-50  $\text{M}\Omega$



(Kodandaramaiah et al., 2012; Margrie et al., 2002). Similarly, our thalamic recordings had holding currents ( $-50.8 \pm 8.9$  pA) at -65 mV holding voltage and resting membrane potentials ( $-62.9 \pm 2.0$  mV) that were not significantly different from our previous cortical work, respectively,  $-23.5 \pm 12.9$  pA ( $p=0.1982$ , Wilcoxon rank-sum test) and  $-61.54 \pm 1.05$  mV ( $p=0.1148$ , Wilcoxon rank-sum test).

Recorded neurons had electrophysiological properties consistent with ventrobasal thalamic nucleus neurons (VB), consisting of the ventral posteromedial nucleus (VPM) and the ventral posterolateral nucleus (VPL). In response to hyperpolarizing current injection, sag potentials were observed (hyperpolarization induced depolarization, indicative of H currents,  $I_H$  ((Kuisle et al., 2006; Leist et al., 2016), see Figure 12b). Following release of hyperpolarizing currents, burst firing was observed indicative of T-type calcium channel activity, often followed by after (spike) depolarization (Kuisle et al., 2006; X Wang et al., 2010) (see Figure 12c arrow).

Comparison of whole-cell recordings in the thalamus with robotic navigation to those previously reported in the thalamus using linear localization is difficult. There are few reports of successful whole-cell thalamic recordings (Brecht & Sakmann, 2002; Margrie et al., 2002; Mease, Sumser, Sakmann, & Groh, 2016b; Oberlaender, de Kock, et al., 2012) and the quality metrics are not reported consistently. However, Margrie et al. 2002 reports that, “Despite the thalamic recordings being carried out on a younger sample of animals the access resistance was consistently greater than that observed for more superficial recordings.” In addition to numerous conversations with other labs performing whole-cell recordings *in vivo* (personal communication), we assume that the scarcity of published whole-cell recordings far below the cortex *in vivo* suggest that they are very difficult to

achieve. In our hands, the single cell that was recorded using linear localization during RPL was of lower quality with an access resistance of 72 M $\Omega$ , resting membrane potential of -45 mV, and holding current of -150 pA.

### 3.4 Discussion

Here, we describe a method to robotically navigate whole-cell patch pipettes through neural tissue *in vivo* in a way that significantly reduces clogging of the tips that occurs commonly when blood vessels are pierced. Pipettes localized without robotic navigation frequently encounter (91% of the trials) and impale obstructions during localization, as others have previously noted (Brecht & Sakmann, 2002; A. K. Lee, Epsztein, & Brecht, 2009; Margrie et al., 2002). This is tolerable for cortical recordings, but as we have shown obstacles are encountered on average every 370  $\mu\text{m}$  and therefore make deep, sub-cortical recordings *in vivo* impractically low yield and quality.

Previous studies have noted the existence and detrimental effect of permanent resistance increases during RPL (D. Lee et al., 2014; Margrie et al., 2002), speculating that electrode penetration of the vasculature was the cause (D. Lee et al., 2014). We have shown, through *in vitro* studies, that these obstructions are very likely caused by encounters with blood vessels larger than 15  $\mu\text{m}$ . Following these encounters, vascular membrane residue adhering to the pipette tip obstructs the tip and increases residual resistance. An efficient spiral navigation algorithm to find the edge of the blood vessel with minimal tissue displacement (17.5  $\mu\text{m}$  on average) enables high yield regional pipette localization.

Robotic navigation enables one to localize pipettes in deep structures (e.g., mouse thalamus at 3 mm) with yields similar to those reported in the cortex using linear localization. Pipettes were successfully localized with robotic navigation to a depth of 3 mm below the pial surface in 82% of trials (n=72/88), comparable to linear localization in the cortex from our previous study (81%, n=128/158,  $p=1$ , Fisher's exact test, (Kodandaramaiah et al., 2012)).

For whole-cell recording yield, there are large ranges of reported yields that make comparison more challenging. Whole-cell yield for blind in-vivo patching has been reported between 20-50% (A. K. Lee et al., 2009; Margrie et al., 2002), while the yield for two photon targeted patching in mice *in vivo* is between 10-20% (Margrie et al., 2003b). For blind, automated whole-cell recording in the mouse cortex, we have previously reported a yield of 31% (Kodandaramaiah et al., 2012). Others have reported yields of 17% (Desai et al., 2015) in mice using similar automation. Our yield of 10% in the mouse thalamus makes recording there practical, although somewhat lower yield than cortical whole-cell recording. Additionally, we believe that all subcortical nuclei are now accessible using this method, as electrodes inserted to the VPM must traverse white and gray matter. However, there may still be regions of the brain that may be difficult to access due to their proximity to the ventricles. In this work, we did not address the penetration of the thick ventricular membranes as such membranes are likely impossible to navigate around and would release CSF into the brain if punctured. Penetration of such membranes remains a problem for maintaining the cleanliness of the electrode, but might be mitigated with the application of a reversible, protective coating (Singh, Zhu, & He, 2004). The advent of further automation strategies such as pipette cleaning (Kolb et al., 2016) may further improve the throughput of these experiments.

The whole-cell recording yield is the product of the yield of the four stages of the patch algorithm (See Figure 10). We note a decrease in gigaseal formation yield with deep patching that is irrespective of localization method, linear or robotic. We have observed higher amplitude heartbeat modulation during the preceding stage, neuron hunting, for the thalamus relative to the cortex, which may indicate greater mechanical disturbances at these depths affecting gigaseal yield. Identifying and overcoming gigaseal yield issues would further advance deep whole-cell patch clamping efforts and motivate further investigation.

One possible opportunity for improved gigaseal yield is to use the lateral steps performed during SICM to map target cells prior to gigaseal attempt to optimize the tip placement with respect to the soma, both *in vivo* and *in vitro*. Blind *in vitro* whole-cell recordings suffer from low yield (generally 50-80% *in vitro*, (Blanton, Loturco, & Kriegstein, 1989)) when compared to image guided *in vitro* studies (> 80%) (Stuart, Dodt, & Sakmann, 1993). Notably, *in vitro* resistance measurements alone are not sufficient to identify cell membrane dimpling and cell shape, visual identifiers commonly used to align pipettes with target cells for successful gigaseals (Desai et al., 2015). Further, local membrane stiffness, a potential proxy for membrane dimpling, can be estimated by modulating pressure and measuring the difference in tip resistance (Sánchez et al., 2008). The combination of pressure modulation and scanning ion conductance microscopy may improve pipette placement on cell membranes and thereby increase the yield of single cell experiments *in vivo* and *in vitro*.

Leakage of biocytin-containing intracellular solution into the surrounding tissue during RPL may cause background and off-target staining. Intracellular solution in the

extracellular space is also undesirable due to the osmotic pressure it places on neurons. This problem may be compounded by the extended time ( $75 \pm 23$  sec vs 6 sec) spent navigating the pipette through tissue under high positive pressure towards the region of interest. Intracellular solution leakage could be reduced by decreasing the positive pressure during RPL. We hypothesize that a lower pipette pressure during RPL will lead to an increase in obstacle detections as less debris, cells, and blood vessels are displaced by the pipette pressure, however the optimal pipette pressure was not investigated in this work. Alternatively, cellular contrasts that are not taken up by cells from the extracellular space, such as DNA plasmids, may reduce off-target labeling (Vélez-Fort et al., 2014).

The average number of navigation events (detected obstacles) for trials that eventually successfully formed a gigaseal (3.65) was lower than for trials that eventually failed to form a gigaseal (7.24). While we found that this difference was not statistically significant, we believe the difference in the means is due to the skew of the navigation event distribution. That is, several failed trials resulted from RPL where successive obstacle detections were triggered throughout their descent, either because they were clogged from internal debris or because accrued debris was not successfully dislodged during the navigation events. Although the pipette resistance ultimately returned to baseline in these trials, we suspect that the tip of the pipette may have become contaminated, but not measurably clogged. Trials with high numbers of successive obstacle detections may indicate unsuccessful navigation and the overall success rate may improve by rejecting these trials.

Intracellular recording has remained as the gold standard electrophysiology technique because of its high quality, mechanical stability, and resolution. Margrie et al. hypothesized

that pipette contamination results in higher access resistances, and thus lower quality thalamic recordings. Previous efforts to reduce the access resistance of recordings performed deep in the brain using higher pressures in the pipette or a guide tube have not been successful (Brecht & Sakmann, 2002). Here, we demonstrate that robotic navigation around blood vessels *in vivo* results not only in higher yield than with linear localization but also higher-quality recordings. Critically, we demonstrate that robotic navigation during regional pipette localization produces whole-cell recordings 3 mm below the pial surface with access resistances similar to those measured from cells in the cortex (Kodandaramaiah et al., 2012; Margrie et al., 2002). Other factors may contribute to differences in yield and access resistance, namely pipette shape and tip geometry, but these parameters are rarely reported or quantified, making comparison difficult. Other parameters were also comparable to previous recordings in cortex, including holding current (voltage clamp, used to keep the cell at -65mV) and resting membrane potential (Kodandaramaiah et al., 2012). Thus, we are confident that *in vivo* whole-cell recording quality is improved from previous efforts to perform whole-cell recordings in the thalamus and are of equivalent quality to recordings in the cortex.

There are very few published studies that show *in vivo* whole-cell recordings at depths 3 mm or greater. In fact, to our knowledge, only 7 such studies have been published to date (Brecht & Sakmann, 2002; Groh et al., 2014; Kuo & Wu, 2012; Margrie et al., 2002; Mease, Sumser, Sakmann, & Groh, 2016a; Oberlaender, de Kock, et al., 2012; Oberlaender, Ramirez, et al., 2012). In contrast, *in vitro* whole-cell recordings in deep subcortical nuclei are abundant (Benavides et al., 2007; Guo et al., 2012; Hu, Nasif, Zhang, & Xu, 2008; Kase, Inoue, & Imoto, 2012; Neuhoff, Neu, Liss, & Roeper, 2002; Porcello, Ho, Joho, & Huguenard, 2002; Sosulina, Graebnitz, & Pape, 2010). This indicates that

there is interest in performing high-yield subcortical whole-cell recordings *in vivo*, while recording depth is an impediment for whole-cell studies in these nuclei. Additionally, the whole-cell patch clamp technique is uniquely positioned to investigate the structure-function-gene relationship (Cadwell et al., 2016). This study opens the door for whole-cell electrophysiology coupled with genetic or morphological profiling throughout the entire brain, which is the focus of worldwide effort (Arkhipov et al., 2016; Cadwell et al., 2016; Oberlaender, Ramirez, et al., 2012; Vélez-Fort et al., 2014) and a major goal of the Brain Research through Advancing Innovative Neurotechnologies (BRAIN) Initiative (Bargmann, Newsome, Anderson, et al., 2014).

## CHAPTER 4.     FEEDFORWARD SYNCHRONIZATION OF PIPETTE TIP TO MEMBRANE MOTION IN VIVO

### 4.1   Introduction

Physiological motion in tissues in the body presents a significant barrier to reliable measurement of *in vivo* neural phenomena. Optical measurements of neuronal activity suffer from motion blur if there is movement in the image during the exposure period. Similarly, intracellular probes are sensitive to the precise position of cells with respect to the pipette tip. For example, although sharp intracellular recordings were developed in 1949 by Gerard and Ling, recordings longer than several seconds were very difficult to obtain, due primarily to micromotion from the heartbeat and respiration of the animal (Britt & Rossi, 1982). This resulted in only a handful of papers describing the use of sharp intracellular recordings *in vivo* in over half a century since its development (Bazhenov, Timofeev, Steriade, & Sejnowski, 1999; U. Kim & McCormick, 1998; Lampl, Reichova, & Ferster, 1999; Ylinen et al., 1995), relegating the method primarily to *in vitro* use. Whole-cell patch clamping partly solves this problem with the robust mechanical stability of the gigaseal, however micromotion can still present a challenge for the initial formation of this configuration, “excessive movement hindered gigaohm seal formation between pipette and neuron” (Margrie et al., 2002).

Reports of the amplitude of this physiological micromotion vary. Lee et al report 1  $\mu\text{m}$  peak-to-peak for cardiac induced motion, and 10  $\mu\text{m}$  for respiratory induced motion (S Lee, Nakamura, & Yamane, 2008). Gilletti and Muthuswamy report 5-10  $\mu\text{m}$  average for breathing motion and 2-3  $\mu\text{m}$  average for heartbeat (Gilletti & Muthuswamy, 2006).



Michael Fee reports an approximately 2 and 4  $\mu\text{m}$  peak to peak average for cardiac and respiratory motion respectively (Fee, 2000).

A variety of strategies have arisen to measure and compensate for this motion in real-time, including laser interferometry and laser triangulation (Fee, 2000; Sungon Lee et al., 2017), visual feedback control (Sungon Lee et al., 2008), and physical probe insertion (Kursu, Tuukkanen, Rahkonen, & Vähäsöyrinki, 2012; S Lee et al., 2008; Vähäsöyrinki, Tuukkanen, Sorvoja, & Pudas, 2009), however none of these methods are applicable throughout the brain, especially at the depth of the thalamus. Still others have suggested invasive surgical procedure to reduce respiration and cardiac motion artifacts *in vivo*, such as draining the spinal fluid or opening the chest cavity (Britt & Rossi, 1982; Matsumoto, Takahara, Matsuki, & Ikegaya, 2011). The optimal solution would preserve the physiological relevance of the preparation and be applicable to intracellular recording in deep subcortical nuclei.

Accordingly, in this chapter, I have developed system to compensate for the micromotion of cells with respect to the pipette tip that uses the electrical resistance of the pipette tip as the measurement of cell-membrane distance. With this system, no external measurements of brain motion need to be utilized and no invasive surgical procedures are required.

I first characterize the sensitivity of the gigaseal formation to the pipette-membrane distance by attempting a gigaseal using a pipette tip at various distances with respect to the surface of plated HEK293 cells *in vitro*. I found that there is a very small window where gigaseal formation is likely (approximately 1-3 microns below the surface).

Next, I set about to record and compensate for micromotion in the brain. The motion due to the heartbeat and breathing moves cells in the brain with respect to the pipette tip. When

cell membranes are near the tip of the pipette, they block the flow of current to the ground electrode in the saline bath above the animal's head. Therefore, the oscillatory modulation of cell's position is detectable as correlated oscillatory modulation of the current measured in voltage clamp mode on the patch amplifier.

I have decided in this work to focus on the applicability of feedforward systems to compensate for this motion. I considered the possibility of using a single frequency sine wave at the primary frequency and phase of the heartbeat, however the heartbeat has considerable power in higher frequency components (harmonics) (Figure 14) and also has slight inter-beat-interval variability. The combination of these two factors would lead to poor approximation of the pipette-membrane distance as a function of time. Rather, the process of heartbeat and respiratory modulation of the brain tissue can be thought of in terms of an impulse response system- that is, there is a brief event (heartbeat: 2 ms, inspiration: 100 ms) that induces relatively long-term motion in distal tissue (100-500 ms). Therefore, I designed a system to use the pipette resistance to measure the distance to the membrane and predict the motion caused by each cardiac and respiratory event by computing the finite impulse response from the cardiac and respiratory events, similar to the work of Michale Fee in anesthetized zebra finches with sharp intracellular electrodes (Fee, 2000). The resulting system is capable of reducing the relative motion of the patch pipette with respect to a nearby cell, which, when suction is applied, greatly increases the probability of achieving a gigaseal and whole-cell state with the cell, both in the cortex and the thalamus.

Encouraged by the improvements in yield of this typically laborious and low-yield process, we designed an ambitious experiment to record from whole-cells in the mouse barrel cortex

and deliver whisker stimulation to the mouse and optogenetic stimulation to thalamocortical projections synapsing onto the recorded cell. In two experiments, we achieved 12 gigaseals, 9 whole-cells, and recorded from 5 of the cells for between 15 and 35 minutes, a sufficient amount of time to gather hundreds to thousands of physiological responses to the stimuli.

## **4.2 Methods**

### *4.2.1 Acute in vivo preparation*

All experiments were performed in accordance with the Georgia Tech Institutional Animal Care and Use Committee (IACUC) guidelines. For *in vivo* preparation, all mice (n=17) were prepared for acute experimentation (Stoy et al., 2017). Briefly, male C57BL/6 mice (p35–p49) were anesthetized with isoflurane and headfixed to a titanium headplate with C&B-Metabond dental cement (Parkell, Edgewood, NY). Craniotomies (1 mm diameter) and duratomies were performed above the Ventral Posteromedial nucleus (VPM) of the thalamus (1.75 mm Rostral, 1.75 mm Lateral, 2.7–3.3 mm below the pial surface). For cortical experiments, craniotomies (0.5 mm in diameter) were performed above the Barrel Cortex (1.8 mm rostral, 2.6 mm lateral, 400  $\mu$ m below the pial surface). In both preparations, stereotaxic coordinates from the Paxinos and Franklin mouse brain atlas (Paxinos & Franklin, 2012) were used. Extracellular solution and intracellular solutions were used as described in Section 3.2.3.

#### 4.2.2 HEK293T cell preparation

Human embryonic kidney (HEK293T) cells (American Type Culture Collection, Manassas, VA) were maintained at 37°C and 5% CO<sub>2</sub> in Eagle Minimum Essential Medium (MEM) supplemented with 5% FBS, 40µM L-glutamine, 100 U/ml penicillin and 0.1 mM streptomycin. Cells were passaged regularly and split when they reached 70% confluency. Cells used for *in vitro* electrophysiology experiments were grown on glass coverslips (12x12mm, No.2, VWR). Patch-clamp experiments were performed in aCSF consisting of (in mM): 161 NaCl, 10 HEPES, 6 D-Glucose, 3 KCl, 1 MgCl<sub>2</sub>, 1.5 CaCl<sub>2</sub> (pH: 7.4). The internal pipette solution consisted of (in mM): 120 KCl, 2 MgCl<sub>2</sub>, 10 EGTA, 10 HEPES (pH: 7.2-7.3, osmolarity: 290-300 mOsm).

#### 4.2.3 Hardware and setup

The hardware setup is shown in Figure 13 and consists of several sub-systems, including the physiology, impulse response calculation, and patch clamp subsystems. The patch clamp subsystem itself consists of manipulator, electrophysiology, and pressure control subsystems.

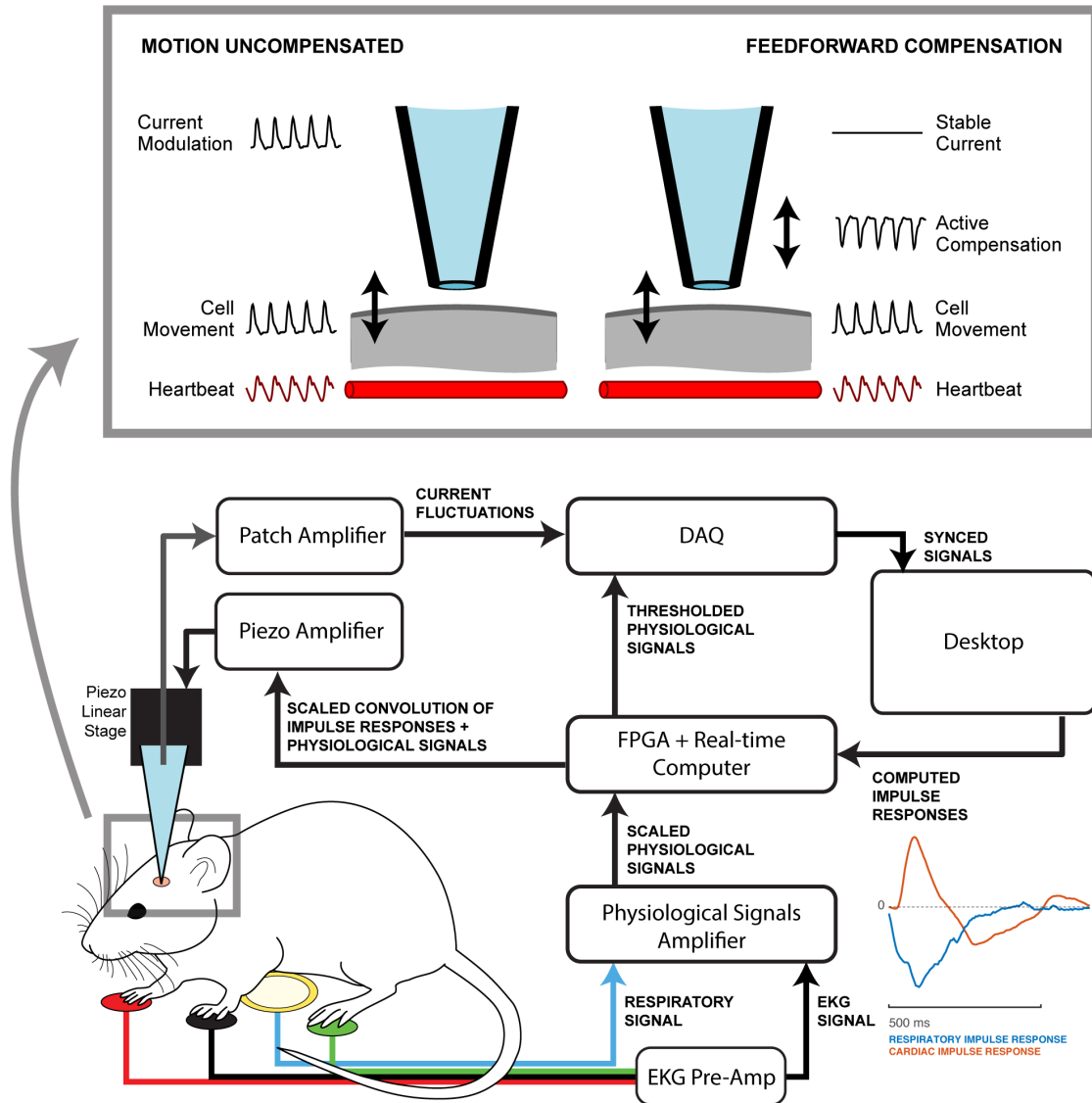


**Figure 13:** Schematic of motion compensation system for whole-cell patch clamp electrophysiology. Cardiac signals are recorded with an EKG and respiratory signals are captured with a piezo pickup under the animal's chest. These physiological signals are amplified and thresholded on an FPGA. Simultaneously, current fluctuations, indicative of a nearby cell moving with respect to the pipette tip are amplified on the patch amplifier and recorded along with the physiological signals on the DAQ. When enough data has been collected, the desktop computer computes the impulse responses and sends them to the Realtime computer. The real-time computer convolves the cardiac and respiratory impulse responses with the appropriate thresholded physiological signals, scales the resulting signal, producing a command signal for the piezo amplifier. The command signal is then amplified and is used to drive the piezo stack in the piezo linear stage. This results in the measurement of a stable resistance on the pipette electrode, indicating that the relative motion between the pipette tip and the cell is reduced.

#### 4.2.4 *Cardiac and respiratory physiological recordings*

The heartbeat was recorded using an EKG preamplifier (C-ISO-256) and a Two Channel Combination Bridge EKG amplifier (ETH-256, iworx). Leads were connected to the animal's front paws and right hind paw via Skintact FS-TB1-5-Gel ECG Electrode (VWR) as shown in Figure 13. The cardiac signal was amplified 10x and a 0.03 Hz – 10 kHz band pass filter was applied. Respiration was recorded non-invasively by placing a 20mm guitar pickup piezo disc element underneath the mouse's chest. The respiratory signal was scaled by 50x and a 0.3 Hz – 10 kHz band pass filter was applied. Cardiac and respiratory signals were thresholded using a Schmitt trigger with a time lockout to prevent triggering on noise in the input signals, implemented on the myRIO FPGA. The thresholded physiological signals and the primary output (patch headstage in voltage clamp mode) from the Multiclamp 700B were recorded for impulse response estimation on an NI USB-6221 BNC DAQ (National Instruments) and also recorded on a Molecular Devices Digidata 1550 digitizer and visualized with PClamp 10 (Molecular Devices, Sunnyvale, CA) for post processing.

#### 4.2.5 *Patch clamp system*

##### 4.2.5.1 Manipulator subsystem

Gross manipulation of the pipette is performed under manual control of the Sutter MP 285 3-axis patch manipulators (Sutter Instruments). Axial movements of the pipette are performed by the one-axis motorized translation stage (PT1-Z8, Thorlabs) is mounted to the z-stage of the Sutter Manipulator at a 45° angle from the vertical (See Section

APPENDIX A for an explanation of this angled stage). A single axis linear piezo flexure stage (P-611.1, Physik Instrumente) with 100  $\mu\text{m}$  travel range mounted parallel to the Thorlabs stage for axial motion synchronization of the pipette tip with respect to the cell membrane. The pipette holder was attached to the piezo stage using a custom water jet milled aluminum bracket.

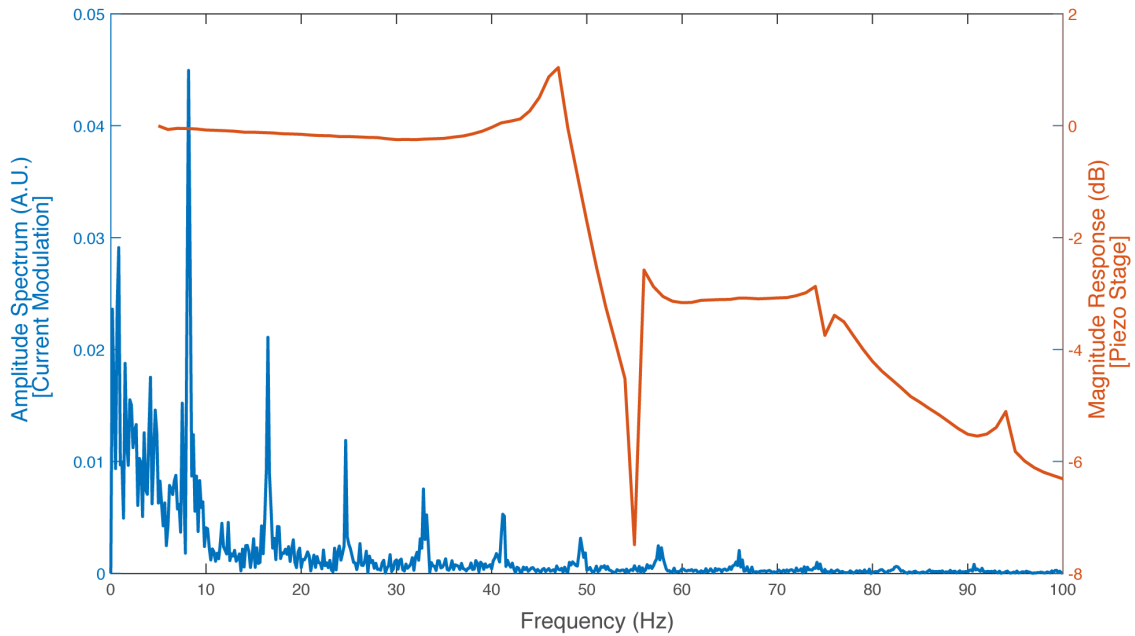


**Figure 14:** Spectral analysis of current modulation and the piezo stage. The amplitude spectrum of a recording of 10 seconds of current modulation by respiratory and cardiac motion (blue) is shown along with the magnitude response of the piezo stage used in this study to a sinusoidal frequency sweep at 1  $V_{pp}$  (corresponding to 10  $\mu\text{m}$  peak-to-peak). The resonant peak of the piezo stage is at 47 Hz.

#### 4.2.5.2 In vivo electrophysiology and pressure control subsystems

Whole-cell patch clamping was performed as described previously (Kodandaramaiah et al., 2016). Briefly, an Autopatcher 1500 (Neuromatic Devices, Atlanta GA) was used to provide computer-controlled pressure and measure resistance for both *in vitro* and *in vivo* experiments. Both *in vitro* and *in vivo* experiments were performed with Multiclamp 700B

amplifiers (Molecular Devices) and signals were digitized at 20kHz (cDAQ-9174, National Instruments), and recorded in PClamp 10.

As in my previous work (Stoy et al., 2017), resistance measurements were performed throughout regional pipette localization, rather than only before and after translation during the RPL stage. Briefly, during regional pipette localization to the region of interest (cortex or thalamus for this study), resistance was recorded starting from ACSF on the surface of the tissue by applying a 20 mV amplitude, 128 Hz square wave at 50% duty cycle and stored as a moving average of 4 cycles. If an obstruction was encountered during RPL (noted by an increase in resistance above a threshold), a sequence of motion and pressure control steps were issued to navigate electrodes efficiently around putative blood vessels, return to the original pipette axis, and continue neuron hunting.

All whole-cells were recorded in current clamp mode.

#### *4.2.6 Software*

##### *4.2.6.1 Synchronization procedure*

Neuron hunting proceeds as discussed in my previous paper (Stoy et al 2017). When a neuron during the neuron hunting step, the synchronization process begins. Forward motion of the pipette (here, 1  $\mu\text{m/s}$ ) is halted, the resistance square wave is stopped, and a -65 mV holding voltage is applied via the Multiclamp commander software panel, enabling high temporal resolution recording of the DC resistance of the pipette. The current from the amplifier (inversely proportional to resistance) and the cardiac and respiration pulse train are recorded in a ring buffer for 8 seconds. The cardiac and respiration pulse train are



used as inputs to the impulse response calculation and were decimated to 200 Hz to improve speed of computation. The impulse response was calculated using the MATLAB function *impzest*. This function can take one or several input arrays and one output array as arguments and will perform a non-parametric impulse response estimation of a given order using a recursive least squares estimation. The resulting cardiac and respiratory impulse responses were delivered to the myRIO embedded real-time system via NI shared variable synchronization over USB. The impulse response kernel was then interpolated to 1 kHz and convolved with the rising edges of the thresholded heartbeat and respiration signals on the real-time system using custom LabVIEW code on the myRIO real-time system. The output was scaled in real time manually by the user by monitoring the fluctuations on the current trace until a suitable reduction in amplitude was observed. The user then selects “Seal at Next Breath” on the vi (LabView virtual instrument) front panel. When the next rising edge from the thresholded respiratory signal arrives, the system waits 0.5 seconds (the typical length of time for most motion artifacts from a single breath to subside, data not shown) and then performs the gigasealing and break-in procedure. During the sealing procedure, if the pipette resistance ( $R_p$ ) crosses a 300 M $\Omega$  threshold, the amplitude of the piezo stage command signal is reduced linearly over 3 seconds to 0 V. If the gigasealing procedure times out or if the user cancels the gigasealing or break-in attempt, the output signal is immediately reduced to 0 V.

#### 4.2.6.2 Gigasealing and break-in procedure

When the gigasealing procedure begins the system restarts the resistance measurement square wave and -40 mbar of suction is applied to the pipette using the Autopatcher box.

After 15 seconds of suction, the pressure is switched to atmospheric and the system will wait for the establishment of a gigaseal, defined as a measurement of total resistance over 1000 M $\Omega$ . Following formation of the gigaseal, the resistance measurement square wave is stopped, and the fast and slow pipette and patch capacitance are neutralized using the Multiclamp software panel.

The break-in procedure is performed by applying a series of up to 15 pulses of suction at -345 mbar for increasing durations. Because the suction pressure is capacitively filtered by the tubing leading from the regulator to the pipette holder, increasing the suction time has the effect of also increasing the maximum pressure that is applied to the patch of membrane in the pipette. The break-in duration is increased by 25 milliseconds prior to each attempt. Following each attempt, the program waits 1.25 seconds and averages the last 10 resistance measurements. If the resistance is above 800 M $\Omega$ , the program will immediately perform another break-in attempt as described above. If the resistance is between 300 M $\Omega$  and 800 M $\Omega$ , the program will wait until the seal has 'recovered' to 800 M $\Omega$  and then perform another break-in attempt. If the resistance is below 300 M $\Omega$ , the program assumes that the patch has been ruptured and returns control to the user. At this point, the user may choose to perform maintenance on the patch (apply slight negative suction to counteract the pressure head from the fluid in the pipette, or attempt to further break into the cell manually, etc.) or the user may proceed onto electrophysiological recording of the whole-cell. After 60 seconds, or manual abort of the break-in process, the pipette is retracted to the surface of the brain to be cleaned as we have described before (Kolb et al., 2016) or exchanged if desired.

#### 4.2.6.3 Optimization of impulseest

Parameters for *impulseest* were tuned to minimize the time to calculate an impulse response and maximize the accuracy of the estimation. This process was performed by selecting segments of pre-recorded data (training data), sampling at 200 Hz, in integer lengths from 4-15 seconds with random offsets and selecting various model orders (64, 128, 256). The cardiac and respiratory impulse responses were calculated 10 times for each combination of parameters. The total time to produce the impulse response estimations was recorded (Total time = recording time + impulse estimation time). Additionally, the quality of fit of the model was assessed on a different set of training data. Specifically, the resulting impulse responses were convolved with the thresholded cardiac and respiratory signals and the sum of squared errors between the convolved signal and the true current trace was calculated.

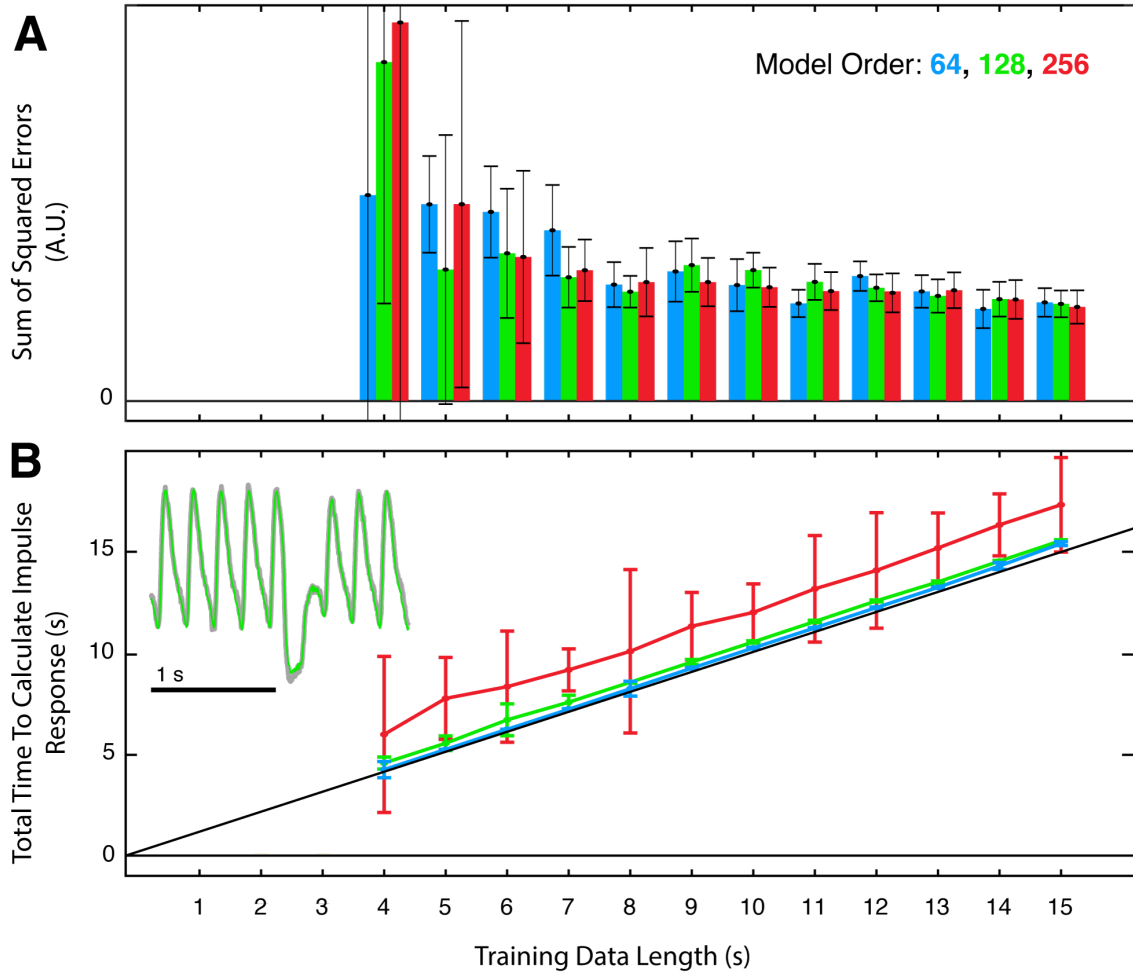


**Figure 15:** Optimization of impulseest parameters. Various training data lengths and model orders were selected. Each combination of parameters was run 10 times. A) The quality of the fit (SSE, lower is better), and B) total time to calculate impulse response are plotted. Total time to calculate impulse response is the sum of training data length and the impulse response calculation time. Diagonal line in lower graph is the unity line. Inset: example of cardiac and respiratory filters (order: 128, training data length: 8 s) convolved with corresponding pulse trains. The result of the convolution is plotted (green) over corresponding current trace (gray).

The results of this optimization can be seen in Figure 15. We chose a model order of 128 instead of 64 because the marginal time required to calculate the impulse response function was negligible and because at a sampling rate of 200 Hz, the impulse response length is 0.65 seconds, which we determined was sufficient to capture all respiratory dynamics (data not shown). Additionally, we chose a training data length of 8 seconds because marginal

increases in training data length beyond this value did not confer significantly better fit (lower SSE from Figure 15). Using these parameters, the FIR model was computed using the training data in an average of  $0.29 \pm 0.02$  seconds.

#### *4.2.7 Measurement of in vitro relationship between gigaseal yield and pipette-membrane distance*

The sensitivity of gigaseal formation to the distance between the membrane and the pipette tip was determined *in vitro* using HEK293T cells. The cells were visualized under 40X magnification using DIC optics. For each trial, a pipette filled with intracellular solution under 30 mbar of positive pressure was lowered near the surface of a cell and centered in X and Y above it. The pipette was then stepped forward in 200 nm steps and the resistance was measured after each step. When the pipette resistance had increased  $0.1 \text{ M}\Omega$  above the initial pipette resistance (the threshold to begin gigasealing defined in our previous HEK cell patch clamping paper (Kolb et al., 2016)), the Z position of the manipulator was defined as the “cell surface”. The pipette forward motion was halted when the pipette resistance had increased to  $0.2 \text{ M}\Omega$  above the initial pipette resistance. The pipette was then retracted  $30 \text{ }\mu\text{m}$  (to eliminate backlash) and then moved to a random Z position between  $3 \text{ }\mu\text{m}$  above the cell surface to  $7 \text{ }\mu\text{m}$  below the cell surface. The positive pressure was then immediately released and a gigaseal and break-in procedure is performed as described in Kolb et al. 2016. The success or failure of the gigaseal and subsequent whole-cell state was recorded.

#### 4.2.8 *Application of high yield autpatching techniques to an investigation of the thalamocortical pathway*

In a subset of cortical experiments (n=2 mice), I applied the techniques that have I developed over the past six years to improve *in vivo* whole-cell patch clamping towards an investigation of the mouse thalamocortical pathway. These techniques included: robotic navigation during RPL (AIM 2), motion compensation (AIM 3), and pipette cleaning using an updated cleaning chemical and procedure that I discovered (Appendix Section A.3, (Kolb et al., 2016), and an upcoming paper by Kolb et al, manuscript under review). Specifically, I collaborated with Peter Borden and Dr. Caleb Wright, PhD to investigate the role of the sensory ‘environment’ and ventral posterior medial region (VPM) projection synchrony on intracellular dynamics in the barrel cortex.

A line of transgenic mice was used that expresses the bacterial opsin ChR2 in the VPM. These neurons send excitatory projections to the barrel cortex (layer 4), which are stimulated using a blue LED. This optical stimulation was combined with whisker stimulation from a galvanometer. Peter Borden produced the transgenic line of mice used in this experiment and mapped the barrel cortex using intrinsic signal optical imaging (ISOI). Caleb Wright designed the stimulus protocol and assisted with data analysis. I performed the surgeries and the experiments and performed the data analysis.

##### 4.2.8.1 Transgenic mice

We used transgenic mice to express the light sensitive protein channelrhodopsin (ChR2) into the lemniscal thalamic projecting neurons using cre/cre-dependent knock-in breeding.

Specifically, we used the Tg(Gsat-NR133-Nsmf-Cre) mouse line to express Cre in the primary somatosensory thalamic regions of the VPM/VPL, and crossbred this mouse line with the Ai32(RCL-ChR2(H134R)/EYFP) mouse line (JAX Laboratories, Stock No#:024109). Mice were genotyped Ttransnetyx, Inc) to confirm the presence of the NR133-Nsmf, YFP, and Rosa genes.

#### 4.2.8.2 Barrel cortex mapping with intrinsic imaging

The mouse primary somatosensory cortex is responsive to physical stimuli and touch sensations on the mouse's body. A large area of representation in this region is the barrel cortex, so called for its discrete, high density cell clusters approximately 100  $\mu\text{m}$  in diameter called barrels, each representing a single whisker.

Prior to each experiment, the location of the C1 and C2 whisker barrel was determined using Intrinsic Signal Optical Imaging (ISOI). Each mouse's barrel cortex was imaged through either intact or thinned skull using a wide-field imaging system to measure cortical spatial activity (184x123 pixel CCD Camera, MiCam02HR SICMedia, Ltd). During all imaging experiments, isoflurane anesthesia levels were lowered to approximately 1%. The cortex was imaged at 10 Hz with a field of view of 4x3mm with a total of a 1.6 Magnification (48 pixels/mm). We used a green (535nm LED) excitation light projected onto the cortical surface that has a high overlap with the hemodynamic absorption spectrum. Collected light was filtered with a set of dichroic mirrors (Bandpass 475/150 nm and Longpass 495 nm, Semrock, Inc) and a bandpass emission filter between wavelengths of 520/35 nm (Semrock, Inc). The imaging system was focused at approximately 300  $\mu\text{m}$

below the cortical surface to target cortical layer 2/3. In order to evoke a cortical intrinsic response, the whisker was repetitively stimulated at 10Hz for 6 seconds.

The activity map and co-registered blood vessel map generated during the ISOI session is shifted, rotated and deformed to match it with the vasculature observed on the experiment day. The activity map indicates the region of activity for the C1 whisker and is targeted by performing a craniotomy over the location of the dark spot seen in the center of the image.

Imaging of a single barrel is performed on a plane parallel to the brain surface; however, the pipette axis is 12.5° off of this axis. To compensate for this angular difference, the pipette is brought to the surface of the brain at the center of the active region, identified by aligning the co-registered ISOI map to the vasculature (See Figure 16), and then moved approximately 89  $\mu\text{m}$  medial as shown in Figure 17.

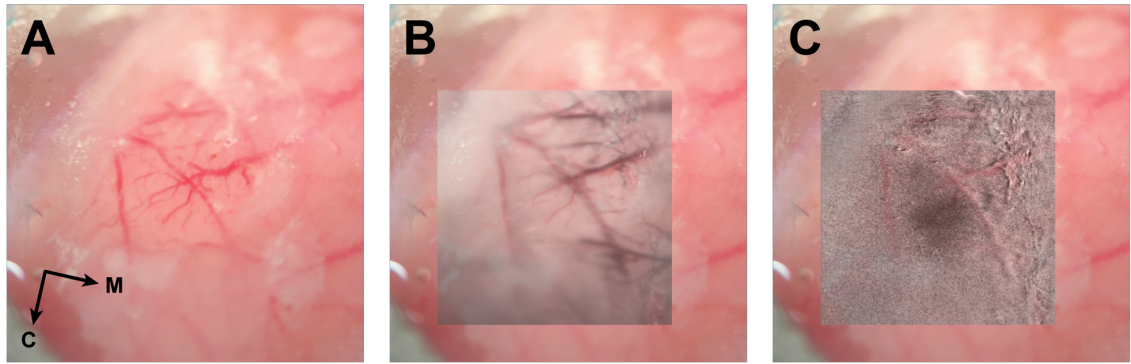


**Figure 16:** Alignment of intrinsic signal optical imaging (ISOI) signal with vasculature. Intrinsic images were captured 3 days prior to electrophysiology experiment. Here, the C1 whisker was rapidly stimulated and images were captured under red light (650 nm) before and after the stimulation and averaged over several trials. Darker regions indicate local consumption of blood oxygen, a proxy of activity. A co-registered blood vessel image is taken under 550 nm light. A) Cortical vasculature can be seen through the thinned skull preparation under perfusion of saline. B) Blood vessel map is shifted, rotated and deformed to match it with the vasculature observed on the experiment day. C) The co-registered activity map indicates the region of activity for the C1 whisker and can easily be targeted by performing a craniotomy over the location of the dark spot seen in the center of the image.



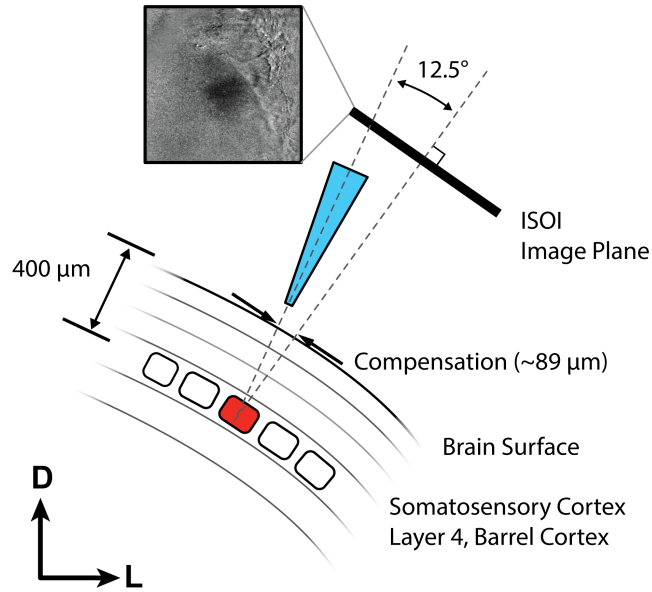


**Figure 17:** Compensation of angular difference between pipette axis and ISOI normal. The pipette axis is  $12.5^\circ$  from the axis normal to the ISOI image plane. The location of the barrel of interest is determined with respect to the pipette axis by trigonometry. The pipette (shown in blue here) is then brought to the surface of the brain in the center of the area of activity determined by the ISOI session and then moved approximately  $89 \mu\text{m}$  medial to ensure that the pipette passes through the barrel of interest (red rectangle).

#### 4.2.8.3 Optical stimulation

Axonal projections terminating in the barrel cortex were stimulated with a blue light (470 nm, M470F3, THORLABS), which was driven at 1.2 Amps with a THORLABS LEDD1B driver. The LED was coupled to a  $400 \mu\text{m}$  diameter multimodal optic fiber which was positioned using a manual micromanipulator to within  $200 \mu\text{m}$  of the pial surface above the craniotomy. The LED was triggered in TTL mode using a command signal from the cDAQ-9174.

#### 4.2.8.4 Whisker stimulation

Whisker stimulation was performed using a galvo (galvanometer optical scanner model 6210H, Cambridge Technology) with a custom milled aluminum fixture with holes to permit the reliable stimulation of a single whisker. The stimulator was placed on the right side of the mouse's face 5 mm from the whisker pad. The rotating arm of the galvo-motor was arranged such that the mean whisker position during noise stimulation was its resting point and the stimulus was delivered along the rostro-caudal axis. The galvo was controlled using an analog output signal from the cDAQ-9174 and the galvo position was recorded on the Digidata 1550 Digitizer. Whisker punctate stimuli were delivered at 1200  $\mu\text{m}$ . White noise was delivered to the whisker on half of the trials with punctate whisker stimulation and half of the trials with optogenetic stimulation.

### 4.3 Results

#### 4.3.1 *Effect of pipette-membrane distance on giga-sealing yield in vitro*

In a manuscript currently under review, we report the development of an automated patch clamping system for intracellular recording in HEK293T cells (Kolb et al, manuscript under review). In this manuscript, a pipette is stepped toward a cell in 1  $\mu\text{m}$  steps until the pipette resistance increases by at least 0.1  $\text{M}\Omega$ , at which point giga-seal formation is attempted. We report that the whole-cell yield using this procedure is 77% (n=54 whole-cell recordings, 70 attempts, 7 pipettes).

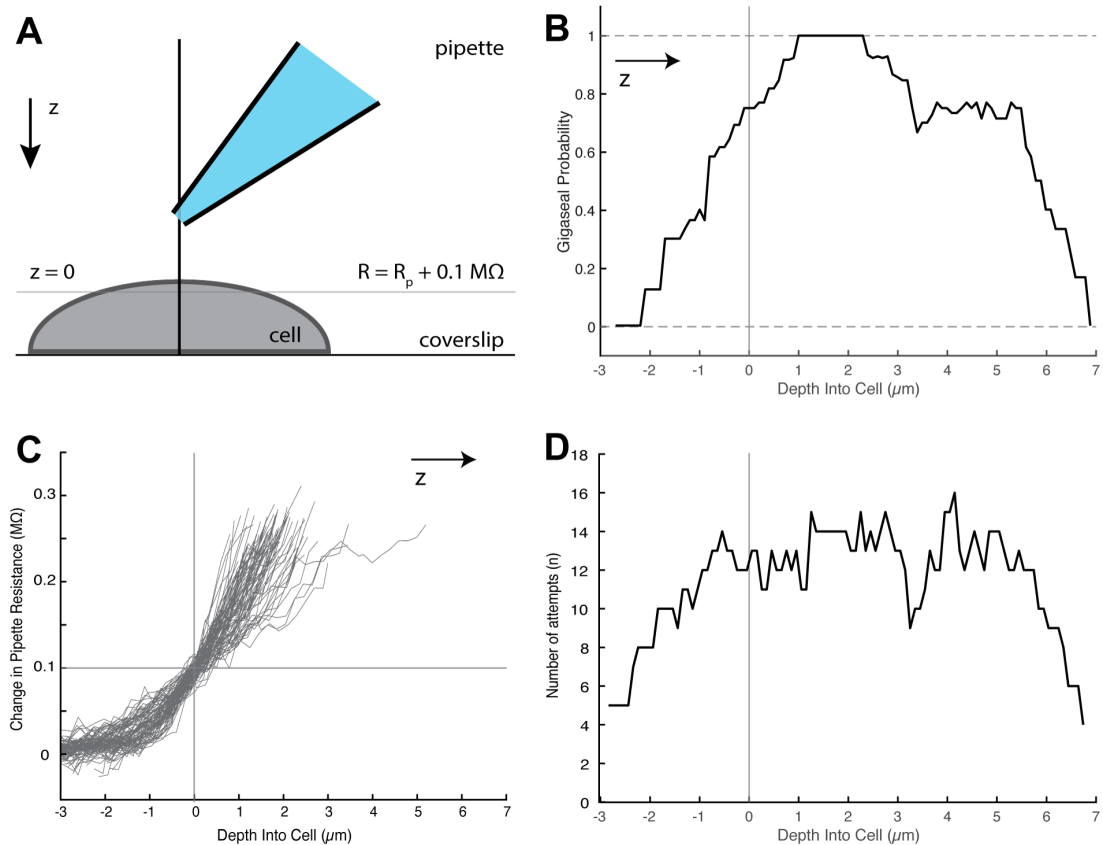


**Figure 18:** Measurement of the relationship between pipette-membrane distance and gigaseal probability. A pipette was slowly lowered vertically onto a plated HEK293T cell. At a resistance increase of  $0.1 \text{ M}\Omega$ , the pipette is determined to be at the surface of the cell. The pipette is then moved into a random position between  $3 \mu\text{m}$  above and  $7 \mu\text{m}$  below the surface of the cell and a gigaseal is attempted. A) shows a schematic of this process. B) Gigaseal yield as a function of pipette position with respect to the membrane. Yield was calculated as the number of gigaseals / total number of attempts within a sliding  $2 \mu\text{m}$  window. Pipettes  $2.5 \mu\text{m}$  or more above the cell will never form a gigaseal with the pipette. There is a clearly optimal location to perform a gigaseal attempt ( $1\text{--}2 \mu\text{m}$  below the surface of the cell). C) Pipette resistance increases as the pipette is stepped down into the cell. The cell surface is defined as the location where the pipette resistance increases  $0.1 \text{ M}\Omega$  above its initial resistance in the saline bath far above the cell. D) Number of trials at each depth (calculated with a  $2 \mu\text{m}$  sliding window).

To explore the relationship between small changes in the distance between the pipette and cell membrane and the probability of gigaseal formation, we performed an experiment in HEK293T cells. The distance between the pipette and the membrane ( $z_{pm}$ ) was varied between 3  $\mu\text{m}$  above and 7  $\mu\text{m}$  below the surface of the cell and a gigaseal was attempted on the cell ( $n=59$  attempts, 40 gigaseals, Figure 18a). The resulting yield (successful gigaseals / number of attempts) with respect to pipette-membrane distance was smoothed with a 2  $\mu\text{m}$  moving average window at 0.1  $\mu\text{m}$  intervals. There is a clear relationship between the pipette-membrane distance and the probability of gigaseal formation. At the surface of the cell, 0  $\mu\text{m}$  on Figure 18b indicated by a vertical line, the gigaseal yield is 75% ( $n=9$  gigaseals / 12 attempts). These results conform to our previous measurements of the probability of achieving a whole-cell configuration in HEK293 cells ( $p=1$ ,  $n=54/70$ , Fisher's Exact Test, Kolb et al, manuscript under review), although break-in was not attempted on the cells in this experiment. Within a 3  $\mu\text{m}$  window (2  $\mu\text{m}$  above the cell surface to 1  $\mu\text{m}$  below the cell surface), the probability of gigaseal formation increases from 0 - 100%. When the pipette was pushed further into the cell, the gigaseal rate remained at 100% between 1  $\mu\text{m}$  to 2.5  $\mu\text{m}$  below the surface. As the pipette is advanced further, up to 7  $\mu\text{m}$  below the cell surface, the gigaseal rate drops to 0%. Each probability plotted in Figure 18b was calculated as the result of at least 4 attempts as shown in Figure 18d.

#### 4.3.2 *Synchronization of pipette-membrane distance*

To evaluate the success of the feedforward system at approximating the finite impulse response of physiological sources of motion in the brain, whole-cell patch clamp trials were performed in the cortex ( $n=7$  mice, 70 trials) and in the thalamus ( $n=8$  mice, 76 trials).

Neuron hunting was performed as we published previously (Kodandaramaiah et al., 2012; Stoy et al., 2017). The forward progress of the pipette was halted when the pipette resistance increased above threshold and the peak-to-peak amplitude of the resistance fluctuations was above a user-determined threshold, indicating that the pipette was near a cell.

Once near a cell, motion compensation was attempted while measuring the pipette current in voltage clamp mode with a DC voltage applied (-65 mV). Unless otherwise stated, these results will discuss the reduction in the peak-to-peak current amplitude resulting from cardiac motion. In the thalamus, the peak-to-peak amplitude of the current fluctuations immediately prior to the motion compensation was  $0.83 \pm 0.56$  nA and was reduced to  $0.21 \pm 0.18$  nA (an average of 72.5% reduction in amplitude, when measured on a trial-by-trial basis). In the cortex, the peak-to-peak amplitude before motion compensation was  $0.67 \pm 0.41$  nA and was reduced to  $0.25 \pm 0.13$  nA (a trial-by-trial average of 57.5% reduction in amplitude). The initial peak-to-peak current amplitude was not significantly different between the thalamus and cortex (cortex:  $0.67 \pm 0.41$  nA, thalamus:  $0.83 \pm 0.56$  nA,  $p=0.326$ , Wilcoxon rank sum test). However, the average amplitude of motion compensation in the cortex and thalamus was  $1.7 \pm 1.14$   $\mu\text{m}$  and  $3.7 \pm 1.42$   $\mu\text{m}$ , respectively, and was found to be significantly different ( $p=3.622\text{e-}6$ , Wilcoxon rank sum test).

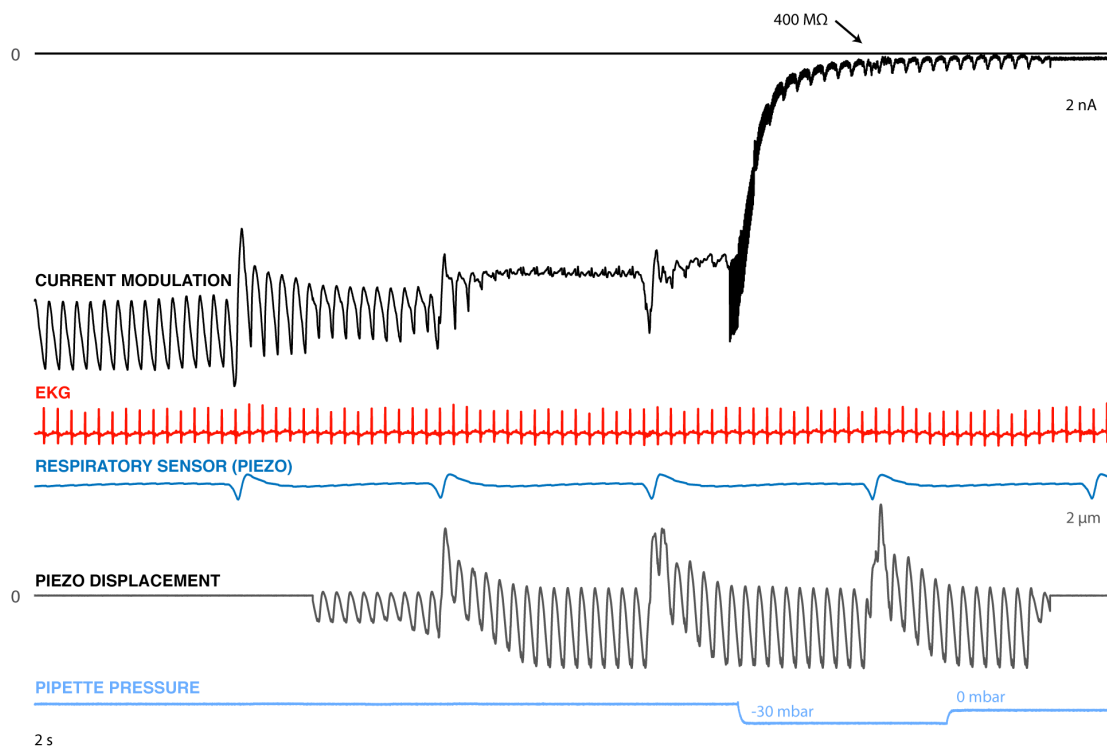


**Figure 19:** Representative result of motion compensation on current amplitude modulation. Top trace: the pipette current is a proxy for the distance to a cell. The current modulation is indicative of a nearby cell moving with respect to the pipette tip. The current signal, along with the EKG signal and respiration signals, is used as input to MATLAB's `impulseest` function, which nonparametrically computes the contribution of each cardiac and respiratory event on the current signal. The resulting impulse responses are convolved with the thresholded EKG and respiration signals and used as the command signal for the piezo stage. The user manually scales the output of the convolved signal until the current modulation is minimized and then triggers the gigasealing attempt. After the arrival of the next respiratory event (typically the largest contributor to cellular micromotion by amplitude), the system waits 0.5 s and then applies gentle suction to rapidly form a gigaseal. In this instance, the series resistance increases to approximately 400 M $\Omega$  before the arrival of the next respiratory event. At high series resistance, the seal is mechanically stable, so the motion compensation is turned off, and the break-in attempt can be performed to perforate the membrane and achieve a whole-cell configuration. Note that when the pressure is released, the resistance measurement square wave is applied.

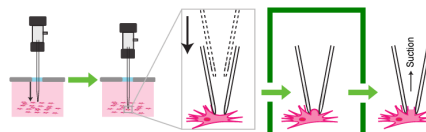
An example of this motion compensation process can be seen in Figure 19. Here, a 10 M $\Omega$  pipette is used to form a gigaseal with a thalamic cell after reduction of the cardiac and respiratory motion. The cardiac current fluctuations were reduced by 89% (1.14 to 0.13 nA) and the respiratory current fluctuations were reduced by 51% (2.35 to 1.16 nA). Following a suitable reduction in the amplitude of current fluctuations, a slight negative pressure (-30 mbar) was applied to form a gigaseal. The cell achieved a gigaseal in 3.7 s, and, importantly, achieved a series resistance of 400 M $\Omega$  before the arrival of the next respiratory event. We surmise that a large series resistance, but not necessarily a gigaseal, is critical for the mechanical stability of the seal.

Reducing the relative motion between the pipette and the cell in the thalamus resulted in an increase in gigaseal yield commensurate with our previous whole-cell patch clamping efforts in the cortex and hippocampus. Specifically, gigaseals were formed in 32/66 trials where regional pipette localization and neuron hunting were performed successfully. This is a significantly higher gigaseal yield in the thalamus than we previously reported (17/64 gigaseals, See Figure 20,  $p=0.0117$ , Fisher's exact test, Stoy et al 2017), when only the robotic navigation system was utilized. In fact, the yield is comparable to our previous study where the Autopatcher was first deployed in the cortex and hippocampus of mice (28/55 gigaseals, See Figure 20,  $p=0.8559$ , Fisher's exact test, Kodandaramaiah et al 2012).

In the cortex, trials where motion compensation was used during gigasealing and robotic navigation was used during regional pipette localization achieved whole-cell configuration at a rate similar to Kodandaramaiah et al (See Figure 20, first row,  $p=0.1706$ ), and our gigaseal yield (66%,  $n=41/62$ ) was slightly, but not significantly higher than our previous

efforts in the mouse cortex (Kodandaramaiah et al. 2012: 51%, n=28/55, p=0.1317, Fisher's exact test).

Following the formation of a gigaseal, the membrane is ruptured with one or more brief pulses of suction to form a whole-cell state. The whole-cell yield, for all pipettes inserted to a depth of 3+ mm in the thalamus using the methods described here, was 24% (n=18/76 attempts, Figure 20)



Region	Depth	Motion Compensation	RPL Method	Regional Pipette Localization (RPL)	Neuron Hunting	Gigaseal Formation	Break In	Total Yield
Cortex + Hippocampus	≤ 1.7 mm	No	Linear	81% 59/73	93% 55/59	51% 28/55	82% 23/28	31% 23/73
Cortex	≤ 1 mm	Yes	Robotic n=	93% 65/70	95% 62/65	66% 41/62	73% 30/41	43% 30/70
Thalamus	≥ 3 mm	No	Linear n=	25% 24/95	88% 21/24	10% 2/21	50% 1/2	1% 1/95
Thalamus	≥ 3 mm	No	Robotic n=	82% 72/88	89% 64/72	26% 17/64	53% 9/17	10% 9/88
Thalamus	≥ 3 mm	Yes	Robotic n=	91% 69/76	96% 66/69	48% 32/66	56% 18/32	24% 18/76

**Figure 20:** Results from whole-cell patch clamp experiments *in vivo* with various improvements. Gray rows indicate experiments conducted for this chapter. Green box indicates that the gigaseal formation stage is being optimized in this chapter. First row: Cortex and hippocampus recordings performed by Suhasa Kodandaramaiah in 2012. The remaining rows were performed by the author. As a result of the motion compensation described in this chapter and robotic navigation during RPL described in the previous chapter, thalamic whole-cell recordings can be performed with 24% yield (approximately 1 in 4 pipettes inserted into the brain will achieve a whole-cell state).



#### *4.3.3 Effect of thalamic synchrony and sensory background on barrel cortex neuronal activity*

As an animal traverses through space, it must detect properties of its environment to build a model of its surroundings. In the case of the mouse, one of its primary sensory inputs is the whiskers, large, specialized hair with numerous mechanical receptors in the follicle. The path that information takes from this follicle to the cortex is called the vibrissae pathway. Whisker deflections are mechanically transduced at the whisker follicle by the specialized ends of a neuron in the trigeminal ganglion. This ganglion neuron synapses in the Trigeminal nucleus in the brainstem. These brainstem cells then synapse onto the ventral posterior medial nucleus (VPM) of the thalamus, which in turn synapse onto Layer 4 of the primary sensory cortex, also known as the barrel cortex. At each stage, neurons, and the network in which they are embedded, modulate the information that is transmitted to the next region. The primary purpose of this pathway seems to be the encoding of “features” (edges, surfaces, movement, etc.) of the environment that are important to the animal, detected as deflections of the whiskers.

The way that these features are encoded depends on the environment, or “background” in which they are embedded. For instance, in the vibrissae pathway, repetitive background whisker stimulation that precedes the presentation of a strong, punctate, feature significantly effects the feature-evoked spiking pattern in primary somatosensory cortex (S1). Specifically, our collaborators have shown that background whisker stimulation modulates the theoretical detectability and discriminability of embedded sensory features (based on ideal observer analysis of cortical activity, (Whitmire, Waiblinger, Schwarz, & Stanley, 2016)).

My collaborator, Dr. Caleb Wright, hypothesizes that there are two mechanisms that contribute to this phenomenon. First, it has been shown that background stimulation tends to de-correlate feature-evoked firing in the thalamus, reducing the synchrony of feature-evoked inputs to S1 (Whitmire et al., 2016). In this case, we would expect background whisker stimulation to alter the amplitude and spatial extent of the subthreshold cortical feature response - more synchronous inputs corresponds to larger-amplitude, more spatially-diffuse cortical responses. Second, it has been shown that thalamocortical synapses onto inhibitory neurons are more strongly adapted than synapses onto excitatory neurons (Cohen-Kashi Malina, Jubran, Katz, & Lampl, 2013; Cruikshank, Urabe, Nurmikko, & Connors, 2010; Gabernet, Jadhav, Feldman, Carandini, & Scanziani, 2005; Heiss, Katz, Ganmor, & Lampl, 2008). This differential synaptic adaptation would then tend to elevate the ratio of feedforward excitation to inhibition, broadening the temporal "window of integration" for feature-evoked cortical spiking.

We designed an experiment to tease apart these two contributions. We obtained whole-cell patch clamp recordings in current clamp mode from neurons in L4 of S1 in the isoflurane-anesthetized mouse. In one set of trials, we presented punctate whisker "features" either in isolation or embedded in a white noise "background" whisker stimulus. We inspected for effects of the background stimulation on subthreshold activity evoked by the sensory feature. Episodic traces centered on each stimulus presentation were baseline-normalized by subtracting the most common voltage value on the trace's histogram (1 ms bins over -100 to 0 mV). The point-by-point median value of each trace was then calculated and is shown as a thick black line in Figure 22.

As expected, we found that the background stimulus tended to reduce the amplitude and increase the width of the short-latency subthreshold response (see Table 3 and Figure 22). This is consistent with the effects of both changes in thalamic synchrony and differential synaptic adaptation. We therefore devoted another set of trials to assessing the contribution of changes in synaptic strength and synchrony to this phenomenon. In particular, we replaced the sensory feature with brief (1 ms) direct optogenetic stimulation of thalamocortical terminals in L4. That is, we evoked firing in L4 neurons via the thalamocortical axonal terminals, but in "bypassing" thalamus, removed any direct influence of changes in thalamic synchrony during the post-stimulus window. In the two trials with strong optogenetic response (Cells 4 and 5, See Figure 21 and Figure 22), we observed that the background whisker stimulus had only a very small effect on both the amplitude and width of the light-evoked postsynaptic potential (See Table 2 and Figure 22).

These preliminary results suggest that background sensory stimulation modulates cortical feature responses in large part via changes in thalamic synchrony, with short-term synaptic adaptation of thalamocortical and intracortical synapses contributing to a lesser degree.

	Whisker Stimulation						Optogenetic Stimulation					
	FWHM (ms)		Time to Peak (ms)		Peak Amplitude (mV)		FWHM (ms)		Time to Peak (ms)		Peak Amplitude (mV)	
	Feature + Noise	Feature + Noise	Feature + Noise	Feature + Noise	Feature + Noise	Feature + Noise	Light Pulse Noise	Light Pulse Noise	Light Pulse Noise	Light Pulse Noise	Light Pulse Noise	Light Pulse Noise
Cell 2	17.1	24.8	21.3	27.7	18.1	12						
Cell 4	36.4	39.7	21.9	38.8	17	13.8	30.7	30.2	18.1	16.2	17.8	17.2
Cell 5	54	47.7	38	43.8	26.4	23	42.9	46.4	19.4	21.4	25.5	25.6
Cell 6	41.9	44.2	39.4	45.9	27.6	28.8						
Cell 7	30.8	45	28.6	42.9	26.4	16						

**Table 2:** Results of 5 whisker responsive whole-cells recorded in the mouse barrel cortex. Whisker and optical stimulation were performed with various conditions listed in the column headers. In all cells, the peak of the subthreshold response to the punctate whisker stimulus (“feature”) was delayed when the feature was embedded in a noise background, also known as an adapting stimulus. Additionally, as a result of the noise background, the amplitude of the response and the width of the response (here, the full-width-at-half-max (FWHM)), increased (except in Cell 5). Notably, cells that had presynaptic thalamocortical inputs that were responsive to optogenetic stimulation did not exhibit a significant shift in the time-to-peak when the light pulse was embedded in a noise background. Similarly, the width of the subthreshold response was not significantly different in either case.

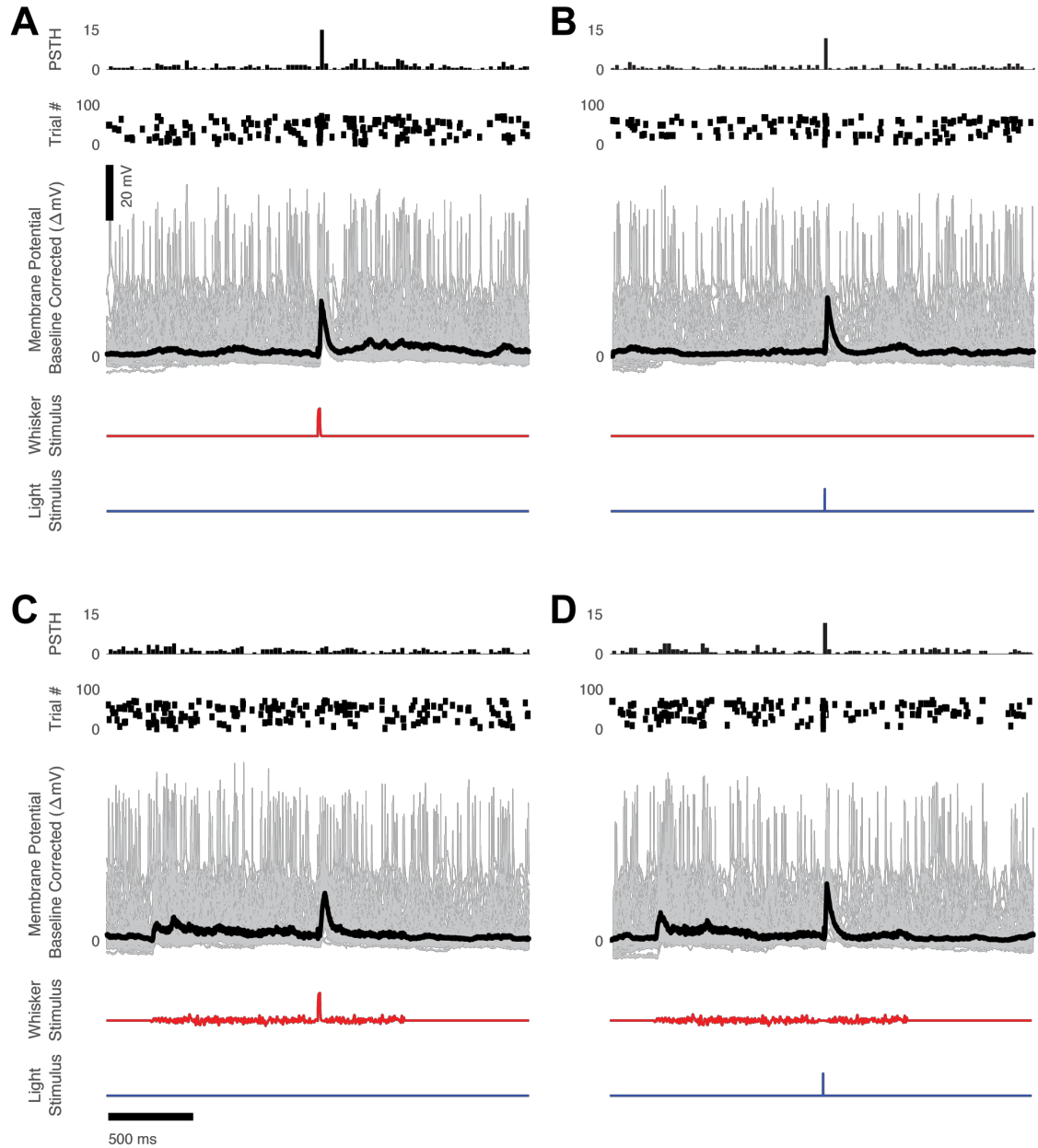


**Figure 21:** Representative data from a whole-cell recorded in the cortex demonstrating the effect of whisker stimulus and light stimulus of pre-synaptic terminals. This cell, labelled Cell 4 in this manuscript, was held for 35 mins. The resting membrane potential was -77 mV. Each sub figure contains a peri-stimulus time histogram with spike rate in spikes/s, a raster plot with square boxes indicating action potentials, baseline-corrected membrane potential fluctuations recorded in current clamp mode, and whisker and light stimulus recordings. Membrane potential was baseline corrected by calculating the histogram of voltage values for each trial and subtracting the most common value from the membrane potential for the trial. A) Punctate whisker stimulus with no whisker noise and no light stimulus. B) Light stimulus of thalamo-cortical axons in the mouse whisker

barrel cortex. No whisker stimulus delivered. C) Whisker punctate stimulus embedded in whisker noise. Note that there is a slight increase in subthreshold activity due to the whisker noise and a significant subthreshold response in response to the punctate stimulus. However, there is no increase in spike rate above baseline. D) Light stimulus embedded in whisker noise.

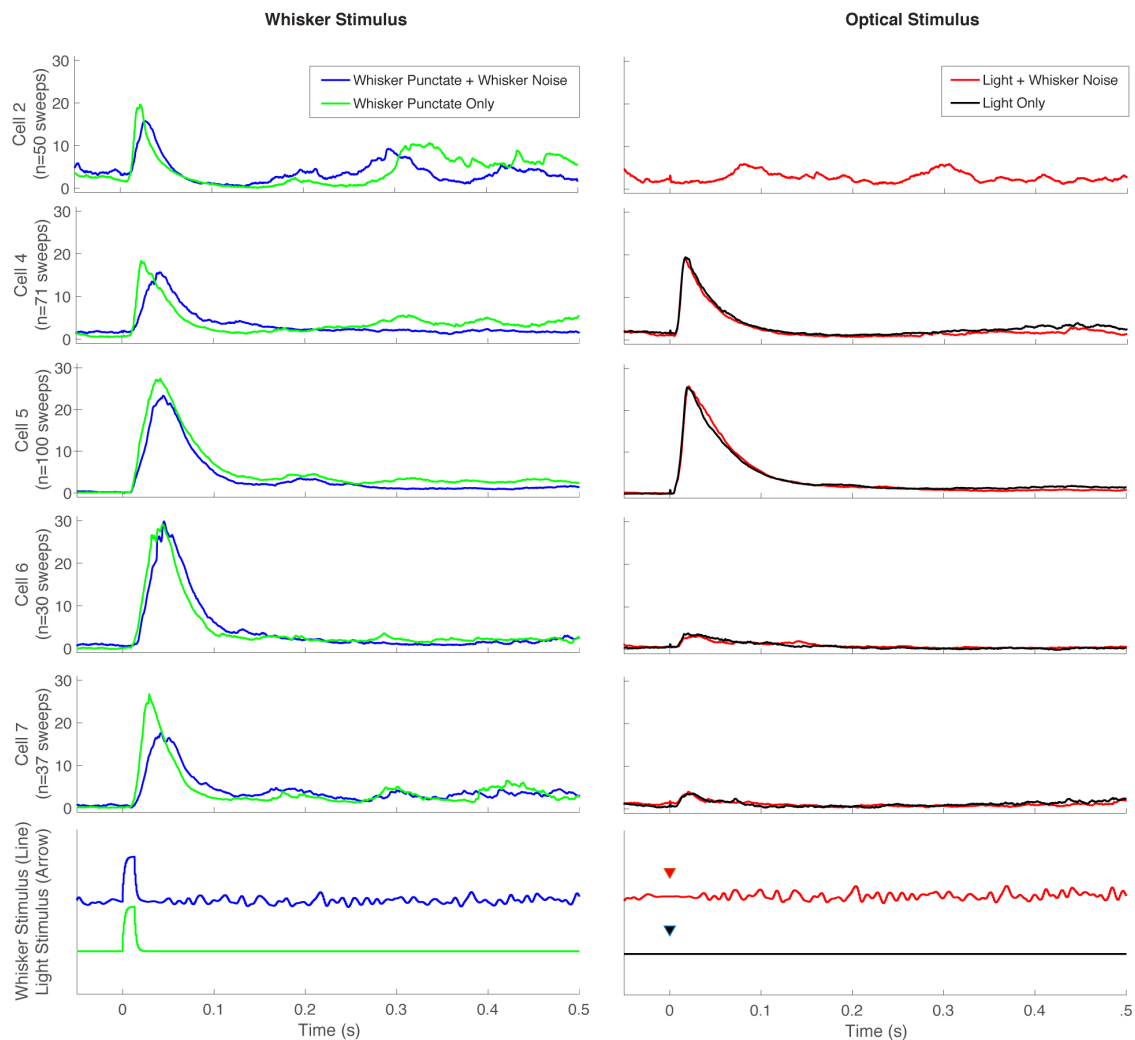


**Figure 22:** Subthreshold response to whisker and light stimuli from five whisker responsive cells in the mouse barrel cortex. Cells 4 and 5 were strongly responsive to light stimulus of presynaptic neighbors. Cells 6 and 7 were less responsive to light stimulus. In each cell, the peak of the subthreshold response to punctate whisker stimulus embedded in noise was delayed with respect to the punctate whisker stimulus alone (Cell 4: 14.7 ms, Cell 5: 6.6 ms, Cell 6: 5.4 ms, Cell 7: 18.4 ms). Cells 4 and 7 showed a concomitant reduction in amplitude of the peak response and broadening of the subthreshold response to punctate whisker stimulus when the stimulus was embedded in noise.

#### 4.4 Discussion

In this work, I have demonstrated 1) that there is a significant distance dependent relationship on the likelihood of gigaseal formation *in vitro*, 2) that the distance between the membrane and the pipette fluctuates during the gigasealing step *in vivo*, 3) that by measurement of the pipette current and physiological signals, the impulse response can be rapidly estimated, 4) that by convolution of the impulse responses with incoming physiological signals, on-line compensation of the distance between the pipette and the cell membrane can be performed, and, critically 5) that this stabilization procedure results in a significantly higher gigaseal rate in deep subcortical nuclei, such as the thalamus. Importantly, this gigaseal rate is commensurate with previously reported yields for manual and Autopatching yields *in vivo* in the cortex (Kodandaramaiah et al., 2012). This method therefore opens the door to high-yield patch clamping studies throughout the brain at yields similar to those expected in cortical patch clamping *in vivo*. With the combination of this method and the methods discussed in previous chapters (robotic navigation during RPL and automated pipette cleaning), the yield and fatigue barrier to patch clamping in the thalamus is greatly reduced.

The whole-cell recording yield is the product of the yield of the four stages of the patch algorithm (See Figure 20). We note that there is still a low rate of successful break-in (in this work, 56% in the thalamus, 68% in the cortex), with deep patching that is irrespective of localization method, linear or robotic. We suspect that further optimizing the average distance between the pipette and the cell during the break-in stage may improve the success. We hypothesize that break-in dynamics (and gigasealing dynamics for that matter) are at least partially related to the tension in the membrane (Milton & Caldwell, 1990), and



that there may be a similar optimal tension on a cell membrane for break-in. Additionally, I hypothesize that membranes may be more likely to rupture poorly when large-amplitude motion arrives during the application of a suction pulse. Further experiments can be performed investigate the relationship between respiratory event arrival times and the failure rate of break-in attempts.

Although the work of Michale Fee in his 2000 paper entitled, “Active Stabilization of Electrodes for Intracellular Recording in Awake Behaving Animals”, provides an important conceptual basis for the above method, there are a number of key differences present in the work shown here (Summarized in Table 3). Fee computed the impulse response using the Fourier transform and standard spectral analysis techniques with (approximately) the inverse Fourier transform of the transfer function. The main advantage of Fee’s method is that, computationally, it is exceptionally fast. When run on the computer used in this study, this computation took less than 1 millisecond. In contrast, we used a least-squares estimation, implemented with MATLAB’s *impulseest* function (explanation of the underlying math in Section A.4). The *impulseest* function proceeds with a recursive least-squares estimation, producing single-shot impulse responses that, when convolved with the physiological input signals, has high correlation to the measured system, as evidenced by the 71% average reduction in current fluctuation amplitude. The computation time of this recursive model is significantly longer ( $\sim 0.5$  s) than the spectral analysis techniques used by Fee. However, the result of this single-shot impulse estimation is that it takes an overall shorter time to apply the impulse response than Fee due to the reduced recording time. Fee used an iterative process to update the cardiac and respiratory impulse responses. Each computation requires 2-4 seconds and is updated at least once, sometimes up to 3 times. This results in a total recording / computation time of 8-24 seconds. Reducing

the time to apply the motion compensation is likely critical to the success of gigaseal formation and to the health of the cell following break-in. When the pipette is in proximity to a cell before gigaseal formation is attempted, it is under positive pressure. This pressure causes a net flow of intracellular fluid out of the pipette tip and alters the ionic composition of the extracellular space. Prolonged perfusion of this space with intracellular solution can damage cells, precluding successful gigaseal formation or reducing the longevity or physiological relevance of whole-cells that are achieved. Additionally, expulsion of unnecessary intracellular solution will degrade the image quality with high background fluorescence or off-target staining if the pipette contains a fluorophore or biocytin for single cell labelling.

	Impulse Response Computation Method	Total Recording / Computation Time	IRF scalar z/i Calculation	Motion Reduction
Michale Fee (2000)	Spectral Analysis $h = F^{-1} \left( \frac{F(y)}{F(x)} \right)$	8 – 24 s recording << 0.1 s computation	80 Hz sine wave (1 s)	‘80% or more’
This work	Least-Squares Estimation $y = Xh + e$ $h = yX^{-1}$	8 s recording $0.55 \pm 0.36$ s computation	Manual (1 s)	$71 \pm 13\%$ reduction

**Table 3:** Comparison of electrode-based motion compensation methods. Note: total computation time in Michale Fee’s work was determined by extrapolating from results in the text. The cardiac FIR filter is computed and then the respiratory FIR filter is computed. Each computation requires 2-4 seconds and is iteratively updated at least once, sometimes up to 3 times. This results in a total recording / computation time of 8-24 seconds.

When a cell moves with respect to a pipette, the distance between the pipette and the membrane contributes to the amplitude of the measured current. This relationship is known to be nonlinear (Rheinlaender & Schäffer, 2013). For example, when the average distance is greater than 1x the pipette diameter, no change in current will be measured. When the

distance between the cell and the pipette decreases, the flow of current to ground is impeded by the cell membrane. As the cell nears the pipette during its modulated position cycle, we expect the flow of current to decrease, and as it moves further than 1x the pipette diameter away, we expect the current to be rectified to the original pipette current. Finally, if the pipette has pressed into the cell far enough, we would again expect the pipette current to be rectified, indicating that the membrane is being pulled against the pipette (the cell is nearly impaled in this configuration). We did not notice that there was current rectification immediately prior to gigasealing on any of the trials performed in this study. Rather, the pipette current was slightly reduced (approximately 5-10% of the original current). This suggests that the pipettes were slightly indenting the surface of the cell's membranes in this study, immediately prior to gigasealing. However, this is the same decrease in current that we have used in all previous studies with the Autopatcher, both in the cortex and the thalamus (Kodandaramaiah et al., 2012; Stoy et al., 2017), yet in this study I report significantly higher gigaseal yield when motion compensation is applied. Further studies can be performed to investigate the success rate due to average membrane distance *in vivo* and *in vitro*. Specifically, a study of distance dependent gigasealing rate can be performed in neurons in slices of brain tissue to more closely reflect the deformability of the cells and their surroundings, as opposed to the cells plated on stiff substrates used in this study. I still expect that there will be an 'inverted U' shaped graph, similar to Figure 18. Regardless of preparation, pipettes at large distances from cell membranes will never form gigaseals and pipettes that are pushed too far into the cells will eventually damage the membrane. Therefore, I expect that the region of high yield gigaseal formation will be larger, but not infinitely so. Further, the long-term health of cells that have been greatly indented during gigaseal formation is of concern. Any study that seeks to establish a robust distance

dependent gigaseal rate for cells in brain slices should take this factor into account and measure the resting membrane potential and the longevity of the whole-cell recording.

One other effect of the updated Autopatching software has been the timing of the gigaseal formation. In all previous versions of the Autopatcher that have descended from the original 2012 paper (Kodandaramaiah et al., 2012), positive pressure was released without regard to the respiration of the animal. In this work, the gigasealing formation was triggered precisely 0.5 s following the detection of a breath. It is clear from our results that the largest amplitude motion contribution is due to the respiration. Therefore, I cannot currently rule out that the improvement in whole-cell patch clamping *in vivo* presented here can be at least partially attributed to the timing of positive pressure release, at least when the breathing artifact was left uncompensated. This potential improvement imparted by the timing of gigasealing formation can be expected to be reduced when the animal is under light-anesthesia or in awake preparations. In these situations, the animal's respiratory period is significantly shorter ( $< 1$  s) than in the anesthetized case presented here ( $> 2.5$  s on average). In our preparation, a seal that begins forming immediately after one breath, creating a mechanical stable bond before the arrival of the next breath. However, in lightly anesthetized preparations the membrane may not have enough time to fuse to the interior lumen of the pipette before it is dislodged by another respiratory event.

The finding that there is a significant distance dependent gigaseal yield in HEK cells *in vitro* not only helped lay the motivational foundation for this work, but also has already been incorporated into the automated HEK cell patch clamping protocols used in our lab and others. The improvements in yield are dramatic- by advancing the pipette 1  $\mu\text{m}$  further into the cell, we have shown that the whole-cell yield has improved from 71% ( $n=111/155$

whole-cells) to 88% (n=102/115 whole-cells,  $p=0.0008$ , Fisher's exact test). This improvement has implications for drug and protein screening platforms. In these situations, throughput and quality are of utmost importance, as there are often dozens to hundreds or thousands of targets or drugs that need to be assessed.

We were able to achieve numerous whole-cell recordings in the mouse cortex and record physiologically relevant signals for between 15-35 minutes. The stability and reliability of the automated system presented in this thesis enables us to plan further exciting experiments and ask questions that can only be answered with the sensitive whole-cell patch clamp method. For example, with high-yield thalamic access, it may now be possible to relate the sensory coding of single cells in the VPM to both sensory environment and the cell's resting membrane potential. Additionally, it may be interesting to continue gathering data using the same experimental method presented in this chapter. Future experiments are needed to more thoroughly measure sensory parameter space, titrate overall light levels and achieve more focal light delivery (to the principal cortical column), measure the theoretical discriminability and detectability of feature- and light-evoked responses, and obtain simultaneous recordings in VPm and S1 (to quantify thalamic synchrony and cortical responses on a trial-by-trial basis).

## CHAPTER 5. DISCUSSION

The success of the BRAIN initiative will be determined by the ability of neuroscientists to develop scalable tools to access multi-modal cell type information throughout the brain. Similarly, an understanding of the sensory system and how information flows through it and is transformed within each brain region is crucial to an understanding of the brain. It is also crucial to be able to understand the sensory system to effectively combat disease and damage to these systems. All sensory inputs (except for the olfactory input) are routed through the thalamus, and there is still significant debate about its role in sensory processing. Several big questions remain as to the sensory coding properties of cells in the thalamocortical circuit, including the role of thalamic resting membrane potential, a measurement that can only be stably obtained by whole-cell patch clamp *in vivo*. However, historically this measurement would have been difficult to make as whole-cell recordings are exceedingly difficult to obtain deep below the cortex, as evidenced by the relative lack of publications reporting whole cells below the cortex (See Section 1.5). Similarly, hippocampal tissue and tissue in deeper cortical strata such as layer 5 or 6 are currently inaccessible without removing overlying tissue or inserting invasive structures such as GRIN lenses or prisms (Helmchen & Denk, 2005; Levene, 2004).

In order to solve these problems, the field of neuroscience requires the development of high throughput machines that allow investigators to repeatably and reliably perform difficult neuroscience experiments. We have taken several approaches to the development of such tools which confers benefits for large scale investigations by single, coordinated institutions as well as tools which can be adopted by investigators that enable many, highly customizable experiments throughout the brain.

In the first aim, the automated electroporator robot was deployed to collect a test set of data for The Allen Institute for Brain Science (Li et al., 2017). While this system confers marginal benefits over manual operation for small scale studies (cell attached recording and electroporation have be performed manually (Dempsey, Turner, Le, Sun, Farah, et al., 2015; Judkewitz et al., 2009)), The Allen Institute’s goal is to sample and catalog a sizeable fraction of the cells in the visual cortex (V1 in mouse has approximately 475,000 cells, (Herculano-Houzel, Watson, & Paxinos, 2013)). Therefore, the benefit of fully automated cell-attached recording and genetic modification is likely restricted to very large-scale investigations.

The second approach that has been taken in this work is the improvement of access of subcortical tissue. Improving this access by developing new tools has a democratizing effect by allowing researchers to confidently and reliably achieve whole-cell recordings throughout the brain, even in high value preparations that may take months to develop, breed, train, or otherwise prepare for the experimental paradigm.

## **5.1 Major contributions**

The Brain Research through Advancing Innovative Neurotechnologies, (BRAIN) initiative has brought together thousands of scientists and engineers through a decade-long, multi-billion-dollar vision of advancing neuroscience through the development of new tools. In its inaugural year, I was fortunate enough to be in very good company as one those researchers. I share the belief that neuroscience must improve its tools to begin to unlock the mysteries of the brain. As such, I have focused this work on the development and

improvement of electrophysiological techniques for application in the living brain. Specifically, In this work, I

- Designed and built a robotic platform to enable the identification, recording, and labeling of single cells via a cell-attached configuration in an automated and reliable fashion.
- Significantly improved the yield of thalamic whole-cell patch clamping, thereby increasing the accessibility of the whole-cell technique to the entire brain, by:
  - Experimentally identifying that penetration of blood vessels is the cause of clogged pipettes during insertion to deep brain structures.
  - Designing an algorithm to navigate around obstructions that cause clogging during pipette localization to deep brain structures (increased whole-cell yield from 1% to 10%).
  - Quantifying the relationship between the gigaseal formation success rate and the distance from the pipette tip to the cell membrane (in plated HEK293 cells, there is an approximately 3  $\mu\text{m}$  window of high-yield gigaseal formation, measured from the surface of the cell).
  - Identifying that motion of the cell with respect to the pipette during the gigasealing stage is detrimental to the formation of a gigaseal (cells measured *in vivo* moved between approximately 2 – 4  $\mu\text{m}$  peak-to-peak).
  - Implementing a system to rapidly apply a compensatory motion to the pipette and experimentally demonstrating a significant improvement in gigaseal yield in the thalamus *in vivo* (increased whole-cell yield from 10% to 24%).



- Built the first system for unattended whole-cell patch clamp recordings from the cortex and the thalamus *in vivo* utilizing pipette cleaning.
- Greatly improved and helped commercialize the cleaning and immediate re-use of patch clamp electrodes with chemical and algorithmic improvements that enable the ultra-high throughput and indefinite reuse of glass electrodes (pipettes can now be re-used and form gigaseals indefinitely. Previous maximum was approximately 10 re-uses before failure).
- Demonstrated the unification of pipette cleaning, robotic regional pipette localization, and motion compensation into a single system and applying it to a series of high-value, high difficulty experiments to uncover functional evidence of thalamocortical synchrony and synaptic modification.

## 5.2 Future work

The automated electroporation software can be improved by automating the detection and identification of cells. At present, the detection of a cell that is not spontaneously active requires the injection of brief, high amplitude pulses of current. To prevent membrane breakdown, these excitatory pulses should be the minimum amplitude required to excite action potentials. A potential automated system for the detection and identification of cells would iteratively inject brief pulses of current and measure the resulting response to determine if the cell has been excited to threshold. If no spikes were detected within a window following the previous current injection, the amplitude of the current injection would be increased, and the process would repeat until spikes were detected or the maximum current injection was reached. Cell-attached configurations that did not exhibit

spontaneous activity or evoked activity would be bypassed and neuron hunting would be resumed. Following a successful current injection attempt, the pipette would be retracted from the brain, moved laterally, and a new trial would commence in a new location. The distance between electroporation sites would be determined in advance by the user and would permit multiple cells to be recorded in a single mouse while allowing full reconstruction of the resulting morphologies. These improvements would allow full automation of this automated electroporation process.

While the motion compensation algorithm greatly improves the success rate of gigaseal formation in the thalamus, it has several stages that require human intervention and is thus ripe for improvement by automation. The measurement and scaling of the output signal can be performed algorithmically by automatically increasing the amplitude scalar for the impulse response output convolution within a set of predefined bounds. A theoretical automated system would then measure the resultant current modulation and could perform a 1D gradient descent algorithm to optimize the amplitude of the output signal. The optimal scalar between the current oscillations and the distance output can be automatically measured using a technique similar to Fee (2000). A sinusoidal displacement of known amplitude can be applied to the pipette and the resulting peak-to-peak amplitude of the fluctuation in current can be measured. Dividing the amplitudes of these two sinusoids produces, roughly, a scalar for the impulse responses produced in following steps.

The dodging algorithm can be improved by decreasing the time required to localize the pipette to the region of interest. This is principally done by increasing the speed at which the pipette is inserted into the brain. However, this would require a simultaneous decrease in the time required to detect that an obstruction and halt the pipette. This could be

performed by measuring the pipette resistance with a higher frequency square wave, or measuring the pipette's resistance with a dc voltage step. A dc resistance measurement is susceptible to baseline drift, however it could be high-pass filtered to only detect rapid increases in resistance.

The success of patch clamping studies in subcortical nuclei hinges on the ability of the investigator to localize the pipette tip to the region of interest. Successful localization requires high accuracy and repeatability of the system, as well as a way to identify the location of the region of interest. Subcortical nuclei are often amorphous in shape and range in size from regions approximately 100  $\mu\text{m}$  in diameter to several millimeters. The precise location of these nuclei can vary drastically from animal to animal, even in preparations of the same age. Typically, these nuclei are targeted using stereotyped atlases of average brain regions, referenced to natural fiducial markings on the skull known as lambda and bregma, intersection points between sutures on the skull. However, precisely positioning electrodes within the subcortical nuclei using these average atlases is still difficult (personal communication). Future work could be devoted to systematically determining reference points to subcortical nuclei with respect to cortical features such as the location of specific barrels in the barrel cortex. Alternatively, the subcortical nucleus of interest could be mapped extracellularly prior to the experiment. This extracellular mapping may sever superficial neuronal processes radiating from the nucleus of interest and may even damage cells in the region of interest once it is encountered. Finally, the errors in the placement of the pipette caused by random error in the bearings, angular errors in the positioning of stages and fixtures, thermal drift, etc. must also be reduced with a careful analysis of the mechanical system using the tools of precision engineering.

## APPENDIX A.

### A.1 Effect of pipette angle on clogging

In vivo patch clamp pipettes are typically replaced manually following every trial. Based on previously published results (Kolb et al., 2016), we demonstrated that pipettes could be reused multiple times for automated *in vivo* patch clamping experiments, up to approximately 10 times. Whereas previous pipettes were typically used for between 5 and 20 minutes, reused pipettes could, in theory, be used for the duration of the experiment, between 4 and 6 hours. During this time, a single piece of debris, such as those shown in Figure 23 could drift down the inside of the pipette and become lodged at the tip, clogging the glass electrode. This clog would block the flow of intracellular solution out of the pipette tip under positive pressure during descent and neuron hunting, which would permit the ingress of unwanted cellular membranes into the tip, precluding later gigaseal formation. A single piece of debris larger than the pipette tip would be difficult or impossible to remove from the pipette, necessitating the replacement of the entire electrode.

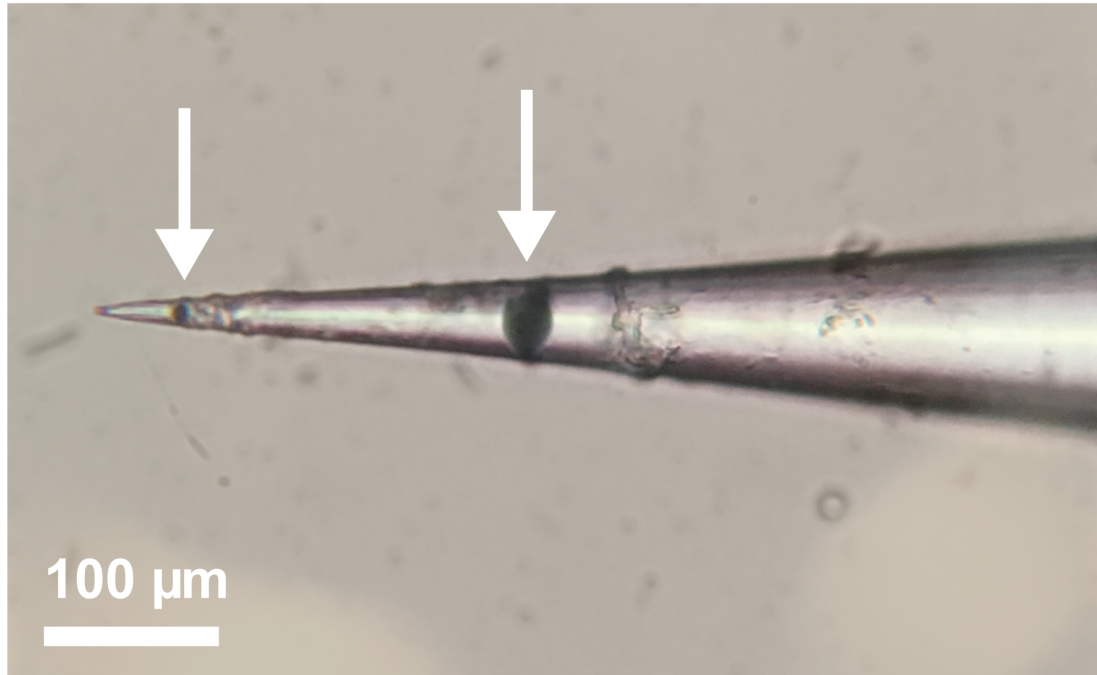


**Figure 23:** Example of debris in pipette following an *in vivo* experiment

The various possible sources of debris are enumerated in Table 4:

Step	Process	Potential debris source
1	Manufacturing of the stock glass pipette blank	Dust from the air, contamination during fire polishing of the ends, debris from DI water cleaning, debris from ‘dust free container’
2	Stock glass container is opened in lab	Dust from the lab air, especially from continuous opening and closing of container
3	Pipette is pulled	Dust from the lab air, particles from handling pipettes, particles from glass clamps
4	Pipette is filled with intracellular solution	Debris in microcentrifuge tube from manufacturing, debris conglomeration in solution post filtration, debris on reusable or disposable pipette fillers
5	Pipette is placed in the pipette holder	Electrode shavings during insertion, air flow from regulators

**Table 4:** Enumeration of debris sources for intracellular electrodes

Despite our best efforts to uncover the source of dust or prevent its ingress into the pipette, including HEPA filtering air near the pipette puller / handling station, using individually sealed pipette fillers once per pipette fill, pre-cleaning pipettes by flushing them with double deionized and filtered water and ethanol, and using pipettes from newly opened batches, we were unable to determine a single source for intra-pipette debris in patch clamp experiments. However, we did notice that pipettes used in *in vitro* experiments clogged far less often than pipettes used in *in vivo* experiments. We hypothesized that this was due to the angle the pipettes were maintained at throughout the duration of the experiment.

To test this hypothesis, we filled pipettes and held them for 20 minutes under atmospheric pressure. The angle that pipettes were held at (vertical, as in *in vivo* experiments, or at 56° from vertical as in *in vitro* experiments) was chosen randomly by flipping a coin as each pipette was filled with 8 µL of DI water that was centrifuge filtered with a 0.2 µm filter. Pipettes were then carried to an *in vitro* patch clamp rig at their initial angle and inserted on a head stage angled at 56° from the vertical, placed under high positive pressure (1000 mbar) for 10 minutes, after which they were inspected under the microscope for clogging debris.

A total of 43 pipettes were filled and tested for clogs (n=26 vertical pipettes and n=17 slanted pipettes). Ten of the vertical pipettes were found to have clogged after the treatment, and none of the slanted pipettes clogged (p=0.0028, Fisher's Exact Test). This led us to conclude that pipettes held at an angle did not clog as often as pipettes held vertically. We hypothesized that this is because gravity pulls debris in the pipette down, and that angled pipettes provide a surface for this debris to rest on, preventing them from moving to the very tip of the pipette. This finding led us to angle the pipette stage of the *in*

*vivo* rig to 45° from vertical. Concurrently, we angled the platform that the heating pad and head plate holders are fixed to 67.5° from the vertical to reduce the steepness of the angle that the mouse was subjected to during experiments. Following the adjustment of the pipette angle, no further internal clogs were detected, even after experiments lasting 4-6 hours.

## **A.2 Improvement of *in vitro* patch clamp yield**

Portions of this section are results from a manuscript currently under review (Kolb et al.)

An experiment was performed to optimize the rate of acquisition of gigaseals and whole-cells in plated HEK 293 cells *in vitro*. Following the measurement of the sensitivity of gigaseals on HEK 293 cells to the distance between the cell membrane and the pipette (performed in Section 4.2.7) a large-scale experiment was performed to implement the findings and improve gigaseal yield in this preparation. Specifically, in previous HEK patching experiments, the pipette was advanced until the tip resistance registered a 0.1 MΩ increase, halting forward movement, and releasing positive pressure. This resulted in a gigaseal 71% of the time when the cleaning solution Tergazyme was used (see Figure 24, blue trace).

We applied the results from the discovery that the optimal location to patch HEK293 cells was when the pipette indented the membrane 1 μm below the surface to a high-throughput patching experiment. During the neuron hunting stage, the pipette forward motion was halted following an increase in tip resistance of 0.1 MΩ as before and then subsequently advanced 1 μm further in a single step. The gigasealing, break in, and recording proceeded

as described in an upcoming manuscript by Kolb et al, including this author. Pipette cleaning proceeded as described previously, except that the cleaning solution was replaced with a 3% wt/vol Tergazyme solution, as described in Section A.3. We used a single pipette to patch ~100 HEK 293 cells over approximately 12 hours. Every 2 hours, the cover slip was replaced, and a new batch of cells was selected.

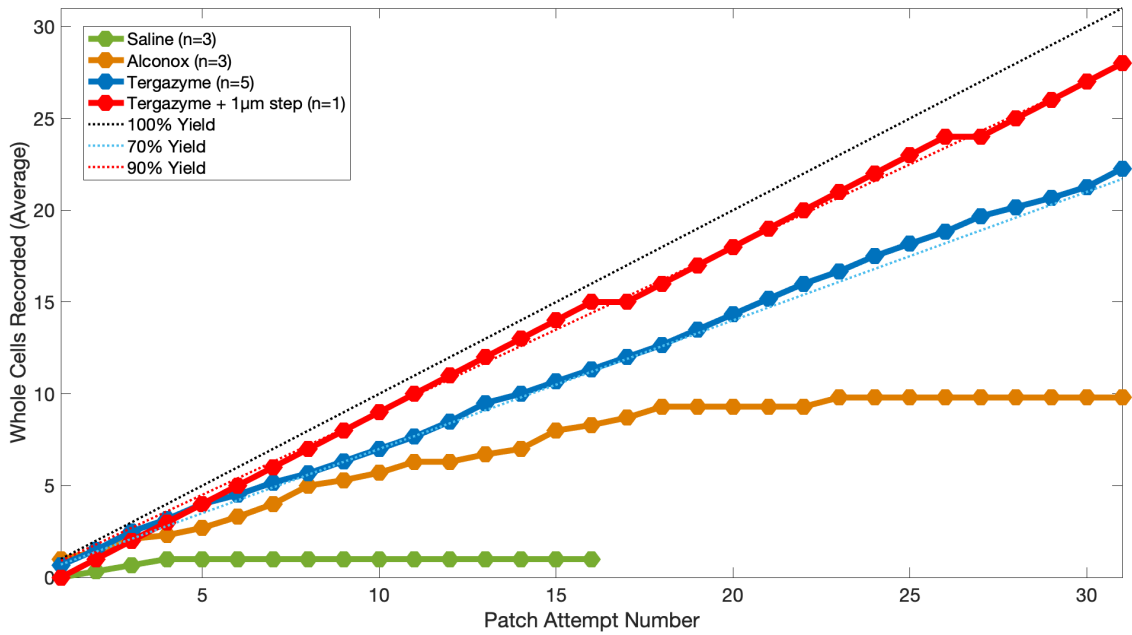


**Figure 24:** Improvement in yield of *in vitro* HEK293 patching. Each line represents the average number of whole-cells acquired after a given number of attempts. Sequential recordings were performed with the same pipette, totaling 30 or more attempts (except for Saline controls which were aborted after 15 failed attempts). Note the improvement in long-term yield when the cleaning agent changed from Alconox to Tergazyme. Note the further improvement gained by advancing the pipette 1 additional micron into the cell (application of results obtained in Chapter 4 of this work).

As shown in Figure 24, trials where the gigaseal was attempted immediately following a 0.1 MΩ increase in pipette resistance (blue trace) produced a whole-cell configuration approximately 71% of the time (n=111/155 whole-cells). When the pipettes were advanced 1µm further and gigasealing was attempted, a whole-cell configuration resulted 88% of the



time (Figure 24, red trace,  $n=102/115$  whole-cells,  $p=0.0008$ , Fisher's Exact Test). With this improvement, whole-cell yield in HEK293 cells is higher than reports of manual whole-cell yield. Further improvements in whole-cell yield are expected with a study and optimization of break-in failure modes.

### **A.3 Improvements to pipette cleaning methods**

Portions of this section are results from a manuscript currently under review (Kolb et al.)

A blinded experiment was performed to determine if the number of cleans that Autopatching robots were capable of performing could be improved. In previous efforts (Kolb et al., 2016) we determined that patch pipettes could be repeatedly re-used if they were cleaned between each trial using a commercially available detergent. A cleaning solution, composed of 3% wt/vol Alconox (Alconox Inc.), was repeatedly drawn into, and forced out of, the pipette tip using high positive and negative pressure. Whereas pipettes that were cleaned with a sham solution (ACSF), would not form gigaohm seals with cells after the first seal, pipettes cleaned with Alconox could be reused multiple times. However, we found that the yield of the gigaseal acquisition was reduced after approximately the 10<sup>th</sup> clean (Kolb et al., 2016). This indicated that cellular debris may still be accumulating on the interior of the pipette tip. We hypothesized that this debris may be protein-based because lipid-glass pipette bonds would be cleaved by the detergent, Sodium Dodecyl Benzene Sulfonate (SDBS), in the Alconox solution, and it has been shown that proteins denature and adsorb to the interior surface of glass pipettes during the gigaseal process (Suchyna, Markin, & Sachs, 2009). To test this hypothesis, we performed a series of blinded experiments on HEK293 cells using the patcherBot, an *in vitro* Autopatching

platform, each time manually selecting the coordinates of 31 cells to patch and exchanging the cleaning solution, while holding all other variables constant. Three solutions were selected at random: ACSF, Alconox, and Tergazyme, each at room temperature. Tergazyme is an inexpensive glassware detergent similar to Alconox with an additional protease enzyme Subtilisin Carlsberg (from the bacterium *Bacillus licheniformis*) which removes proteins adsorbed to glass. Following the acquisition of each whole-cell, the patcherBot cleaned the pipette in the randomized cleaning solution and attempted to patch the cell at the next set of coordinates in the list.

The detergent Tergazyme affords a dramatic improvement in pipette cleaning over Alconox. When cleaning pipettes with Alconox, the patcherBot can only patch-clamp ~10 cells without recording quality degrading (Kolb et al., 2016), which is the main bottleneck preventing even longer unsupervised operation. We suspected that residual proteins adsorbed to the pipette tip were responsible for recording quality degradation after many cleans. Demonstrating the superiority of a candidate cleaning solution over Alconox requires hundreds of recordings to reach statistical significance so we used the PatcherBot for these experiments. Tergazyme-cleaned pipettes outperformed Alconox-cleaned pipettes after 30 cleaning cycles (31 attempted cells, Figure 24). We found no relationship between the number of cleans and the patch-clamp success rate or quality parameters in Tergazyme-cleaned pipettes. With Tergazyme as the cleaning agent, the PatcherBot ran unattended for 109 - 120 minutes. Up to 115 successful whole-cell recordings have been performed with a single pipette using Tergazyme.

#### A.4 Estimation of the impulse response with the least-squares method

The least-squares method proceeds as follows:

$$y = Xh + e$$

Where  $y$  is the observation array, the current fluctuations in our case ( $n \times 1$  vector where  $n$  is the desired order of the filter),  $X$  is an  $n \times k$  matrix of  $k$  system inputs, the cardiac or respiratory impulse response train in our case.

Rearranging, we get an equation for the errors,  $e$ :

$$e = y - Xh$$

Where  $h$  is the impulse response function. The least squares method is performed by first squaring the errors:

$$S(h) = \sum e^2 = e^T e = (y - Xh)^T (y - Xh)$$

For a column vector such as  $e$ , the square operation is achieved by multiplying the original vector by its transposed vector,  $e^T$ , where  $T$  indicates the transpose operation. Distributing the above equation yields:

$$S(h) = y^T y - y^T Xh - X^T h^T y + X^T Xh^T h$$

The solution to the least squares model is at the minimum of the quadratic function. To find this point, we take the derivative of the sum of squared errors with respect to our impulse response vector and set the result equal to zero.

$$\frac{\delta S}{\delta h} = -2X^T y + 2X^T X h = 0$$

Rearranging, we arrive at an equation for the impulse response function

$$h = (X^T X)^{-1} X^T y$$

## **A.5 On the use of conscious creatures for biomedical research**

As I have sought to improve the yield of these scientifically valuable methods, throughout this study, I have always considered the welfare and ethical treatment of the research animals that were used in this study. The use of animals in science is a necessary, if unfortunate reality. The reality is that we must study systems of the body by interacting with various molecules, cells, tissues, organs, and at times, entire organisms themselves. At each level, the action and interaction of subsidiary components such as atoms, organelles, cells, tissues, and organs respectively, are not predictable from first principles. These are so-called emergent phenomena; that is, the incredible complexity of nature lends itself to seemingly novel properties at each level of detail. A common objection to the use of animals is that we ought to simply gather our knowledge into a computational model of the nervous system and study that, or that we know as much as we need to know. However, our understanding of the nervous system has been compared to a pre-Galilean understanding of physics. That is, in our knowledge of deep mysteries of neuroscience such as consciousness, we still believe the sun metaphorically revolves around the earth.

So what exactly is our current, ‘geocentric’ understanding of consciousness? In his book “The Quest for Consciousness,” Christof Koch quotes John Searle who said,

“Consciousness consists of those states of sentience, or feeling, or awareness, which begin in the morning when we awake from a dreamless sleep and continue throughout the day until we fall into a coma or die or fall asleep again or otherwise become unconscious” (Koch, 2012). This definition leaves much to be desired. First, it bases a definition of consciousness on its synonyms, sentience and awareness. Second it simply states that there is a period when we are conscious and a period when we are not. For example, unless you, the reader, are currently dreaming of this passage, we can assume you are conscious.

For our purposes, a more useable definition of subjective consciousness is presented by Giulio Tononi and others in a series of papers on Integrated Information Theory (Tononi, 2008). Although the fundamentals of this theory are outside the scope of this work, this theory attempts to axiomatically produce not just a mechanistic understanding of consciousness, but also to calculate the conscious capacity and the degree of information integration, of a theoretical network of a given size and structure. The implications of this theory are profound: namely that animals, which we know have brains of hundreds of millions to billions of neurons and have at least rudimentary sensory experiences, are potentially conscious, even in a meaningful way that we consider ourselves to be conscious by moment-by-moment experience of it.

Christoph Koch addresses specifically the consciousness of animals, saying,

*It is plausible that some species of animals-mammals, in particular-possess some, but necessarily all, of the features of consciousness; that they see, hear, smell, and otherwise experience the world. Of course, each species has its own unique sensorium, matched to its ecological niche. But I assume that these animals have feelings, have subjective states. To believe otherwise is presumptuous and flies in the face of all*

*experimental evidence for the continuity of behaviours between animals and humans.*

*We are all Nature's children.*

It is with these views that I have approached the use of animals in the experiments described in this thesis. I have taken the utmost care to reduce pain and distress in the animals that I have used and sought to maximize the scientific impact of each experiment. It is my sincere hope that the understanding I have gained through these experiments will improve the lives of humans as well as laboratory animals. By improving the techniques of neuroscience, we can test new theories of perception and understand how the complex network between our ears generates our consciousness.

## REFERENCES

- Akinlaja, J., & Sachs, F. (1998). The Breakdown of Cell Membranes by Electrical and Mechanical Stress. *Biophysical Journal*, 75(1), 247–254. [https://doi.org/10.1016/S0006-3495\(98\)77511-3](https://doi.org/10.1016/S0006-3495(98)77511-3)
- Andermann, M. L., Gilfoy, N. B., Goldey, G. J., Sachdev, R. N. S., Wölfel, M., McCormick, D. A., ... Levene, M. J. (2013). Chronic Cellular Imaging of Entire Cortical Columns in Awake Mice Using Micropisms. *Neuron*. <https://doi.org/10.1016/j.neuron.2013.07.052>
- Arkhipov, A., Berg, J., Buice, M., Gouwens, N. W., Gratiy, S., Iyer, R., ... Zhou, Z. (2016). Inferring cortical function in the mouse visual system through large-scale systems neuroscience. *Proceedings of the National Academy of Sciences*, 113(27), 7337–7344. <https://doi.org/10.1073/pnas.1512901113>
- Bargmann, C., Newsome, W., & Anderson, A. (2014). BRAIN 2025: a scientific vision. .../Science/Brain/2025/( ... Retrieved from [http://acd.od.nih.gov/presentations/BRAIN\\_working\\_Group\\_Report\\_06052014.pdf](http://acd.od.nih.gov/presentations/BRAIN_working_Group_Report_06052014.pdf)
- Bargmann, C., Newsome, W., Anderson, A., & Brown, E. (2014). *Bargmann: BRAIN 2025: A Scientific Vision. Brain...* - Google Scholar. National Institutes of Health. <https://doi.org/10.1111/jmi.12058/full>
- Bazhenov, M., Timofeev, I., Steriade, M., & Sejnowski, T. J. (1999). Self-sustained rhythmic activity in the thalamic reticular nucleus mediated by depolarizing GABA(A) receptor potentials. *Nature Neuroscience*. <https://doi.org/10.1038/5729>
- Benavides, D. R., Quinn, J. J., Zhong, P., Hawasli, A. H., DiLeone, R. J., Kansy, J. W., ... Bibb, J. A. (2007). Cdk5 modulates cocaine reward, motivation, and striatal neuron excitability. *The Journal of Neuroscience : The Official Journal of the Society for Neuroscience*, 27(47), 12967–12976. <https://doi.org/10.1523/JNEUROSCI.4061-07.2007>
- Blanton, M. G., Loturco, J. J., & Kriegstein, A. R. (1989). Whole Cell Recording From Neurons in Slices of Reptilian and Mammalian Cerebral-Cortex. *Journal of Neuroscience Methods*, 30(3), 203–210. Retrieved from <http://eutils.ncbi.nlm.nih.gov/entrez/eutils/elink.fcgi?dbfrom=pubmed&id=2607782&retmode=ref&cmd=prlinks>
- Brecht, M., & Sakmann, B. (2002). Whisker maps of neuronal subclasses of the rat ventral posterior medial thalamus, identified by whole-cell voltage recording and morphological reconstruction. *The Journal of Physiology*, 495–515. <https://doi.org/10.1013/jphysiol.2001.012334>
- Britt, R. H., & Rossi, G. T. (1982). Quantitative analysis of methods for reducing physiological brain pulsations. *Journal of Neuroscience Methods*.

[https://doi.org/10.1016/0165-0270\(82\)90085-1](https://doi.org/10.1016/0165-0270(82)90085-1)

- Cadwell, C. R., Palasantza, A., Jiang, X., Berens, P., Deng, Q., Yilmaz, M., ... Tolia, A. S. (2016). Electrophysiological, transcriptomic and morphologic profiling of single neurons using Patch-seq. *Nature Biotechnology*, 34(2), 199–203. <https://doi.org/10.1038/nbt.3445>
- Cohen-Kashi Malina, K., Jubran, M., Katz, Y., & Lampl, I. (2013). Imbalance between Excitation and Inhibition in the Somatosensory Cortex Produces Postadaptation Facilitation. *Journal of Neuroscience*. <https://doi.org/10.1523/JNEUROSCI.4845-12.2013>
- Collins, F. S., Morgan, M., & Patrinos, A. (2003). The Human Genome Project: Lessons from large-scale biology. *Science*. <https://doi.org/10.1126/science.1084564>
- Constantinople, C. M., & Bruno, R. M. (2013). Deep Cortical Layers Are Activated Directly by Thalamus. *Science*, 340(6140), 1591–1594. <https://doi.org/10.1126/science.1236425>
- Cruikshank, S. J., Urabe, H., Nurmikko, A. V., & Connors, B. W. (2010). Pathway-Specific Feedforward Circuits between Thalamus and Neocortex Revealed by Selective Optical Stimulation of Axons. *Neuron*. <https://doi.org/10.1016/j.neuron.2009.12.025>
- Dempsey, B., Turner, A. J., Le, S., Sun, Q.-J., Bou Farah, L., Allen, A. M., ... McMullan, S. (2015). Recording, labeling, and transfection of single neurons in deep brain structures. *Physiological Reports*, 3(1), e12246–e12246. <https://doi.org/10.14814/phy2.12246>
- Dempsey, B., Turner, A. J., Le, S., Sun, Q. J., Farah, L. B., Allen, A. M., ... McMullan, S. (2015). Recording, labeling, and transfection of single neurons in deep brain structures. *Physiological Reports*. <https://doi.org/10.14814/phy2.12246>
- Desai, N. S., Siegel, J. J., Taylor, W., Chitwood, R. A., & Johnston, D. (2015). MATLAB-based automated patch-clamp system for awake behaving mice. *Journal of Neurophysiology*, 114(2), 1331–1345. <https://doi.org/10.1152/jn.00025.2015>
- Diamond, M. E., von Heimendahl, M., Knutsen, P. M., Kleinfeld, D., & Ahissar, E. (2008). “Where” and “what” in the whisker sensorimotor system. *Nature Reviews Neuroscience*, 9(8), 601–612. <https://doi.org/10.1038/nrn2411>
- Fee, M. S. (2000). Active Stabilization of Electrodes for Intracellular Recording in Awake Behaving Animals. *Neuron*, 27(3), 461–468. [https://doi.org/10.1016/S0896-6273\(00\)00057-X](https://doi.org/10.1016/S0896-6273(00)00057-X)
- Finch, S. R., & Zhu, L.-Y. (2005). Searching for a Shoreline. *ArXiv.Org*. Retrieved from <https://arxiv.org/abs/math/0501123>
- Friedberg, M. H., Lee, S. M., & Ebner, F. F. (2004). The contribution of the principal and spinal trigeminal nuclei to the receptive field properties of thalamic VPM neurons in



- the rat. *Journal of Neurocytology*, 33(1), 75–85.  
<https://doi.org/10.1023/B:NEUR.0000029649.28599.a5>
- Gabernet, L., Jadhav, S. P., Feldman, D. E., Carandini, M., & Scanziani, M. (2005). Somatosensory integration controlled by dynamic thalamocortical feed-forward inhibition. *Neuron*. <https://doi.org/10.1016/j.neuron.2005.09.022>
- Gilletti, A., & Muthuswamy, J. (2006). Brain micromotion around implants in the rodent somatosensory cortex. *Journal of Neural Engineering*, 3(3), 189–195.  
<https://doi.org/10.1088/1741-2560/3/3/001>
- Gong, Y., Huang, C., Li, J. Z., Grewe, B. F., Zhang, Y., Eismann, S., & Schnitzer, M. J. (2015). High-speed recording of neural spikes in awake mice and flies with a fluorescent voltage sensor. *Science*. <https://doi.org/10.1126/science.aab0810>
- Gonzaga-Jauregui, C., Lupski, J. R., & Gibbs, R. A. (2012). Human Genome Sequencing in Health and Disease. *Annual Review of Medicine*. <https://doi.org/10.1146/annurev-med-051010-162644>
- Groh, A., Bokor, H., Mease, R. A., Plattner, V. M., Hangya, B., Stroh, A., ... Acsády, L. (2014). Convergence of cortical and sensory driver inputs on single thalamocortical cells. *Cerebral Cortex*, 24(12), 3167–3179. <https://doi.org/10.1093/cercor/bht173>
- Guo, M.-L., Xue, B., Jin, D.-Z., Liu, Z.-G., Fibuch, E. E., Mao, L.-M., & Wang, J. Q. (2012). Upregulation of Npas4 protein expression by chronic administration of amphetamine in rat nucleus accumbens *in vivo*. *Neuroscience Letters*, 528(2), 210–214. <https://doi.org/10.1016/j.neulet.2012.07.048>
- Haas, K., Sin, W.-C., Javaherian, A., Li, Z., & Cline, H. T. (2001). Single-Cell Electroporation for Gene Transfer In Vivo. *Neuron*, 29(3), 583–591.  
[https://doi.org/10.1016/S0896-6273\(01\)00235-5](https://doi.org/10.1016/S0896-6273(01)00235-5)
- Harvey, C. D., Collman, F., Dombeck, D. a, & Tank, D. W. (2009). Intracellular dynamics of hippocampal place cells during virtual navigation. *Nature*, 461(7266), 941–946.  
<https://doi.org/10.1038/nature08499>
- Heiss, J. E., Katz, Y., Ganmor, E., & Lampl, I. (2008). Shift in the Balance between Excitation and Inhibition during Sensory Adaptation of S1 Neurons. *Journal of Neuroscience*. <https://doi.org/10.1523/JNEUROSCI.2646-08.2008>
- Helmchen, F., & Denk, W. (2005). Deep tissue two-photon microscopy. *Nature Methods*. <https://doi.org/10.1038/nmeth818>
- Herculano-Houzel, S. (2009). The human brain in numbers: a linearly scaled-up primate brain. *Frontiers in Human Neuroscience*. <https://doi.org/10.3389/neuro.09.031.2009>
- Herculano-Houzel, S., Watson, C., & Paxinos, G. (2013). Distribution of neurons in functional areas of the mouse cerebral cortex reveals quantitatively different cortical zones. *Frontiers in Neuroanatomy*. <https://doi.org/10.3389/fnana.2013.00035>

- Higley, M. J., & Contreras, D. (2007). Cellular Mechanisms of Suppressive Interactions Between Somatosensory Responses In Vivo. *Journal of Neurophysiology*, 97(1), 647–658. <https://doi.org/10.1152/jn.00777.2006>
- Hu, X.-T., Nasif, F. J., Zhang, J., & Xu, M. (2008). Fos regulates neuronal activity in the nucleus accumbens. *Neuroscience Letters*, 448(1), 157–160. <https://doi.org/10.1016/j.neulet.2008.10.025>
- Joshi, S., & Hawken, M. J. (2006). Loose-patch-juxtacellular recording *in vivo*--a method for functional characterization and labeling of neurons in macaque V1. *Journal of Neuroscience Methods*, 156(1–2), 37–49. <https://doi.org/10.1016/j.jneumeth.2006.02.004>
- Judkewitz, B., Rizzi, M., Kitamura, K., & Häusser, M. (2009). Targeted single-cell electroporation of mammalian neurons *in vivo*. *Nature Protocols*. <https://doi.org/10.1038/nprot.2009.56>
- Kanjhan, R., & Vaney, D. I. (2008). Semi-loose seal Neurobiotin electroporation for combined structural and functional analysis of neurons. *Pflügers Archiv - European Journal of Physiology*, 457(2), 561–568. <https://doi.org/10.1007/s00424-008-0539-9>
- Kase, D., Inoue, T., & Imoto, K. (2012). Roles of the subthalamic nucleus and subthalamic HCN channels in absence seizures. *Journal of Neurophysiology*, 107(1), 393–406. <https://doi.org/10.1152/jn.00937.2010>
- Kelly, S. T., Kremkow, J., Jin, J., Wang, Y., Wang, Q., Alonso, J.-M., & Stanley, G. B. (2014). The Role of Thalamic Population Synchrony in the Emergence of Cortical Feature Selectivity. *PLOS Comput Biol*, 10(1), e1003418. <https://doi.org/10.1371/journal.pcbi.1003418>
- Kim, S., & McNames, J. (2007). Automatic spike detection based on adaptive template matching for extracellular neural recordings. *Journal of Neuroscience Methods*. <https://doi.org/10.1016/j.jneumeth.2007.05.033>
- Kim, U., & McCormick, D. A. (1998). The functional influence of burst and tonic firing mode on synaptic interactions in the thalamus. *Journal of Neuroscience*. <https://doi.org/10.1523/JNEUROSCI.18-22-09500.1998>
- Kitamura, K., Judkewitz, B., Kano, M., Denk, W., & Häusser, M. (2008). Targeted patch-clamp recordings and single-cell electroporation of unlabeled neurons *in vivo*. *Nature Methods*. <https://doi.org/10.1038/nmeth1150>
- Koch, C. (2012). Neuroscience: A quest for consciousness. *Nature*. <https://doi.org/10.1038/488029a>
- Kodandaramaiah, S. B., Franzesi, G. T., Chow, B. Y., Boyden, E. S., & Forest, C. R. (2012). Automated whole-cell patch-clamp electrophysiology of neurons *in vivo*. *Nature Methods*, 9(6), 585–587. <https://doi.org/10.1038/nmeth.1993>

- Kodandaramaiah, S. B., Holst, G. L., Wickersham, I. R., Singer, A. C., Franzesi, G. T., McKinnon, M. L., ... Boyden, E. S. (2016). Assembly and operation of the autopatcher for automated intracellular neural recording *in vivo*. *Nature Protocols*, 11(4), 634–654. <https://doi.org/10.1038/nprot.2016.007>
- Kolb, I., Stoy, W. A., Rousseau, E. B., Moody, O. A., Jenkins, A., & Forest, C. R. (2016). Cleaning patch-clamp pipettes for immediate reuse. *Scientific Reports*, 6. <https://doi.org/10.1038/srep35001>
- Kuisle, M., Wanaverbecq, N., Brewster, A. L., Frère, S. G. A., Pinault, D., Baram, T. Z., & Lüthi, A. (2006). Functional stabilization of weakened thalamic pacemaker channel regulation in rat absence epilepsy. *The Journal of Physiology*, 575(1), 83–100. <https://doi.org/10.1113/jphysiol.2006.110486>
- Kuo, R. I., & Wu, G. K. (2012). The Generation of Direction Selectivity in the Auditory System. *Neuron*, 73(5), 1016–1027. <https://doi.org/10.1016/j.neuron.2011.11.035>
- Kursu, O., Tuukkanen, T., Rahkonen, T., & Vähäsöyrinki, M. (2012). 3D Active Stabilization System with Sub-Micrometer Resolution. *PLoS ONE*, 7(8), e42733. <https://doi.org/10.1371/journal.pone.0042733>
- Lampl, I., Reichova, I., & Ferster, D. (1999). Synchronous membrane potential fluctuations in neurons of the cat visual cortex. *Neuron*. [https://doi.org/10.1016/S0896-6273\(00\)81096-X](https://doi.org/10.1016/S0896-6273(00)81096-X)
- Lee, A. K., Epsztein, J., & Brecht, M. (2009). Head-anchored whole-cell recordings in freely moving rats. *Nature Protocols*, 4, 385–392. Retrieved from <http://www.ncbi.nlm.nih.gov/pubmed/19247288>
- Lee, D., Shtengel, G., Osborne, J. E., & Lee, A. K. (2014). Anesthetized- and awake-patched whole-cell recordings in freely moving rats using UV-cured collar-based electrode stabilization. *Nature Protocols*, 9(12), 2784–2795. <https://doi.org/10.1038/nprot.2014.190>
- Lee, S., Courties, G., Nahrendorf, M., Weissleder, R., & Vinegoni, C. (2017). Motion characterization scheme to minimize motion artifacts in intravital microscopy. *Journal of Biomedical Optics*. <https://doi.org/10.1117/1.JBO.22.3.036005>
- Lee, S., Nakamura, Y., & Yamane, K. (2008). Image Stabilization for In Vivo Microscopy by High-Speed Visual Feedback Control. *Ieeexplore.Ieee.Org*. <https://doi.org/10.1109/TRO.2007.914847>, "publicationTitle": "IEEE
- Lee, S., Nakamura, Y., Yamane, K., Toujo, T., Takahashi, S., Tanikawa, Y., & Takahashi, H. (2008). Image stabilization for *in vivo* microscopy by high-speed visual feedback control. *IEEE Transactions on Robotics*. <https://doi.org/10.1109/TRO.2007.914847>
- Lein, E. S., Hawrylycz, M. J., Ao, N., Ayres, M., Bensinger, A., Bernard, A., ... Jones, A. R. (2007). Genome-wide atlas of gene expression in the adult mouse brain. *Nature*, 445(7124), 168–176. <https://doi.org/10.1038/nature05453>

- Leist, M., Datunashvili, M., Kanyshkova, T., Zobeiri, M., Aissaoui, A., Cerina, M., ... Budde, T. (2016). Two types of interneurons in the mouse lateral geniculate nucleus are characterized by different h-current density. *Scientific Reports*, 6, 24904. <https://doi.org/10.1038/srep24904>
- Levene, M. J. (2004). In Vivo Multiphoton Microscopy of Deep Brain Tissue. *Journal of Neurophysiology*. <https://doi.org/10.1152/jn.01007.2003>
- Lewicki, M. S. (1998). A review of methods for spike sorting: The detection and classification of neural action potentials. *Network: Computation in Neural Systems*. [https://doi.org/10.1088/0954-898X\\_9\\_4\\_001](https://doi.org/10.1088/0954-898X_9_4_001)
- Li, L., Ouellette, B., Stoy, W. A., Garren, E. J., Daigle, T. L., Forest, C. R., ... Zeng, H. (2017). A robot for high yield electrophysiology and morphology of single neurons *in vivo*. *Nature Communications*. <https://doi.org/10.1038/ncomms15604>
- Lin, M. Z., & Schnitzer, M. J. (2016). Genetically encoded indicators of neuronal activity. *Nature Neuroscience*, 19(9), 1142–1153. <https://doi.org/10.1038/nn.4359>
- Llinás, R. R., & Steriade, M. (2006). Bursting of Thalamic Neurons and States of Vigilance. *Journal of Neurophysiology*, 95(6), 3297–3308. <https://doi.org/10.1152/jn.00166.2006>
- Margrie, T. W., Brecht, M., & Sakmann, B. (2002). In vivo, low-resistance, whole-cell recordings from neurons in the anaesthetized and awake mammalian brain. *Pflügers Archiv European Journal of Physiology*, 444, 491–498. <https://doi.org/10.1007/s00424-002-0831-z>
- Margrie, T. W., Meyer, A. H., Caputi, A., Monyer, H., Hasan, M. T., Schaefer, A. T., ... Brecht, M. (2003a). Targeted whole-cell recordings in the mammalian brain *in vivo*. *Neuron*, 39, 911–918. <https://doi.org/10.1016/j.neuron.2003.08.012>
- Margrie, T. W., Meyer, A. H., Caputi, A., Monyer, H., Hasan, M. T., Schaefer, A. T., ... Brecht, M. (2003b). Targeted whole-cell recordings in the mammalian brain *in vivo*. *Neuron*. <https://doi.org/10.1016/j.neuron.2003.08.012>
- Matsumoto, N., Takahara, Y., Matsuki, N., & Ikegaya, Y. (2011). Thoracotomy reduces intrinsic brain movement caused by heartbeat and respiration: A simple method to prevent motion artifact for *in vivo* experiments. *Neuroscience Research*, 71(2), 188–191. <https://doi.org/10.1016/J.NEURES.2011.06.011>
- Mease, R. A., Sumser, A., Sakmann, B., & Groh, A. (2016a). Cortical Dependence of Whisker Responses in Posterior Medial Thalamus In Vivo. *Cerebral Cortex*, 26(8), bhw144--3543. <https://doi.org/10.1093/cercor/bhw144>
- Mease, R. A., Sumser, A., Sakmann, B., & Groh, A. (2016b). Corticothalamic Spike Transfer via the L5B-POm Pathway *in vivo*. *Cerebral Cortex*, 26(8), bhw123--3475. <https://doi.org/10.1093/cercor/bhw123>

- Milton, R. L., & Caldwell, J. H. (1990). How do patch clamp seals form? A lipid bleb model. *Pflügers Archiv*, 416(6), 758–765. <https://doi.org/10.1007/BF00370626>
- Neher, E. (1995). ..., *ION CHANNELS FOR COMMUNICATION BETWEEN AND WITHIN CELLS, DECEMBER 9, 1991 BY ERWIN NEHER AND ELEMENTARY STEPS IN ...* Nobel Lectures. Retrieved from <http://scholar.google.com#>
- Neuhoff, H., Neu, A., Liss, B., & Roeper, J. (2002). I(h) channels contribute to the different functional properties of identified dopaminergic subpopulations in the midbrain. *The Journal of Neuroscience : The Official Journal of the Society for Neuroscience*, 22(4), 1290–1302. Retrieved from <http://eutils.ncbi.nlm.nih.gov/entrez/eutils/elink.fcgi?dbfrom=pubmed&id=11850457&retmode=ref&cmd=prlinks>
- Obeid, I., & Wolf, P. D. (2004). Evaluation of spike-detection algorithms for a brain-machine interface application. *IEEE Transactions on Biomedical Engineering*. <https://doi.org/10.1109/TBME.2004.826683>
- Oberlaender, M., de Kock, C. P. J., Bruno, R. M., Ramirez, A., Meyer, H. S., Dercksen, V. J., ... Sakmann, B. (2012). Cell type-specific three-dimensional structure of thalamocortical circuits in a column of rat vibrissa cortex. *Cerebral Cortex*, 22(10), 2375–2391. <https://doi.org/10.1093/cercor/bhr317>
- Oberlaender, M., Ramirez, A., & Bruno, R. M. (2012). Sensory experience restructures thalamocortical axons during adulthood. *Neuron*, 74(4), 648–655. <https://doi.org/10.1016/j.neuron.2012.03.022>
- Oyama, K., Ohara, S., Sato, S., Karube, F., Fujiyama, F., Isomura, Y., ... Tsutsui, K.-I. (2013). Long-lasting single-neuron labeling by *in vivo* electroporation without microscopic guidance. *Journal of Neuroscience Methods*, 218(2), 139–147. <https://doi.org/10.1016/j.jneumeth.2013.06.004>
- Pakkenberg, B., Pelvig, D., Marner, L., Bundgaard, M. J., Gundersen, H. J. G., Nyengaard, J. R., & Regeur, L. (2003). Aging and the human neocortex. In *Experimental Gerontology*. [https://doi.org/10.1016/S0531-5565\(02\)00151-1](https://doi.org/10.1016/S0531-5565(02)00151-1)
- Paxinos, G., & Franklin, K. B. J. (2012). *Paxinos and Franklin's the Mouse Brain in Stereotaxic Coordinates*. Academic Press. Retrieved from [http://books.google.com/books?id=8RJZLwEACAAJ&dq=Mouse+Brain+in+Stereotaxic+Coordinates+4th+Edition&hl=&cd=2&source=gbs\\_api](http://books.google.com/books?id=8RJZLwEACAAJ&dq=Mouse+Brain+in+Stereotaxic+Coordinates+4th+Edition&hl=&cd=2&source=gbs_api)
- Petersen, R. S., Brambilla, M., Bale, M. R., Alenda, A., Panzeri, S., Montemurro, M. A., & Maravall, M. (2008). Diverse and temporally precise kinetic feature selectivity in the VPM thalamic nucleus. *Neuron*, 60(5), 890–903. <https://doi.org/10.1016/j.neuron.2008.09.041>
- Pinault, D. (1996). A novel single-cell staining procedure performed *in vivo* under electrophysiological control: morpho-functional features of juxtacellularly labeled thalamic cells and other central neurons with biocytin or Neurobiotin. *Journal of*

- Neuroscience Methods*, 65(2), 113–136. Retrieved from <http://www.ncbi.nlm.nih.gov/pubmed/8740589>
- Polack, P. O., & Charpier, S. (2006). Intracellular activity of cortical and thalamic neurones during high-voltage rhythmic spike discharge in Long-Evans rats *in vivo*. *The Journal of Physiology*, 571(2), 461–476. <https://doi.org/10.1113/jphysiol.2005.100925>
- Porcello, D. M., Ho, C. S., Joho, R. H., & Huguenard, J. R. (2002). Resilient RTN fast spiking in Kv3.1 null mice suggests redundancy in the action potential repolarization mechanism. *Journal of Neurophysiology*, 87(3), 1303–1310. Retrieved from <http://eutils.ncbi.nlm.nih.gov/entrez/eutils/elink.fcgi?dbfrom=pubmed&id=11877504&retmode=ref&cmd=prlinks>
- Rancz, E. A., Franks, K. M., Schwarz, M. K., Pichler, B., Schaefer, A. T., & Margrie, T. W. (2011). Transfection via whole-cell recording *in vivo*: bridging single-cell physiology, genetics and connectomics. *Nature Neuroscience*, 14, 527–532. Retrieved from <http://discovery.ucl.ac.uk/1298469/>
- Rheinlaender, J., & Schäffer, T. E. (2013). Mapping the mechanical stiffness of live cells with the scanning ion conductance microscope. *Soft Matter*, 9(12), 3230–3236. <https://doi.org/10.1039/C2SM27412D>
- Sánchez, D., Johnson, N., Li, C., Novak, P., Rheinlaender, J., Zhang, Y., ... Korchev, Y. E. (2008). Noncontact Measurement of the Local Mechanical Properties of Living Cells Using Pressure Applied via a Pipette. *Biophysical Journal*, 95(6), 3017–3027. <https://doi.org/10.1529/BIOPHYSJ.108.129551>
- Santisakultarm, T. P., Cornelius, N. R., Nishimura, N., Schafer, A. I., Silver, R. T., Doerschuk, P. C., ... Schaffer, C. B. (2012). In vivo two-photon excited fluorescence microscopy reveals cardiac- and respiration-dependent pulsatile blood flow in cortical blood vessels in mice. *American Journal of Physiology-Heart and Circulatory Physiology*, 302(7), H1367--H1377. <https://doi.org/10.1152/ajpheart.00417.2011>
- Sawicki, M. P., Samara, G., Hurwitz, M., & Passaro, E. (1993). Human Genome Project. *The American Journal of Surgery*. [https://doi.org/10.1016/S0002-9610\(05\)80522-7](https://doi.org/10.1016/S0002-9610(05)80522-7)
- Shalem, O., Sanjana, N. E., Hartenian, E., Shi, X., Scott, D. A., Mikkelsen, T. S., ... Zhang, F. (2014). Genome-scale CRISPR-Cas9 knockout screening in human cells. *Science*. <https://doi.org/10.1126/science.1247005>
- Sherman, S. M. (2005). The role of the thalamus in cortical function: not just a simple relay. Retrieved from <http://search.proquest.com/openview/499c5494ba1955f48e4733d8d3b5afa9/1?pq-origsite=gscholar>
- Shevchuk, A. I., Gorelik, J., Harding, S. E., Lab, M. J., Klennerman, D., & Korchev, Y. E. (2001). Simultaneous Measurement of Ca<sup>2+</sup> and Cellular Dynamics: Combined Scanning Ion Conductance and Optical Microscopy to Study Contracting Cardiac Myocytes. *Biophysical Journal*, 81(3), 1759–1764. <https://doi.org/10.1016/S0006->

- Singh, A., Zhu, H., & He, J. (2004). Improving mechanical stiffness of coated benzocyclobutene (BCB) based neural implant. *Conference Proceedings : ... Annual International Conference of the IEEE Engineering in Medicine and Biology Society. IEEE Engineering in Medicine and Biology Society. Annual Conference*, 6, 4298–4301. <https://doi.org/10.1109/IEMBS.2004.1404197>
- Sosulina, L., Graebenitz, S., & Pape, H.-C. (2010). GABAergic interneurons in the mouse lateral amygdala: a classification study. *Journal of Neurophysiology*, 104(2), 617–626. <https://doi.org/10.1152/jn.00207.2010>
- Stoy, W. A., Kolb, I., Holst, G. L., Liew, Y., Of, A. P. J., & 2017. (2017). Robotic navigation to subcortical neural tissue for intracellular electrophysiology *in vivo*. *Physiology.Org*. <https://doi.org/10.1152/jn.2017.118.issue-2;pageGroup:string:Publication>
- Stuart, G. J., Dodt, H. U., & Sakmann, B. (1993). Patch-clamp recordings from the soma and dendrites of neurons in brain slices using infrared video microscopy. *Pflügers Archiv*, 423(5–6), 511–518. <https://doi.org/10.1007/BF00374949>
- Suchyna, T. M., Markin, V. S., & Sachs, F. (2009). Biophysics and Structure of the Patch and the Gigaseal. *Biophysical Journal*, 97(3), 738–747. <https://doi.org/10.1016/j.bpj.2009.05.018>
- Suk, H. J., van Welie, I., Kodandaramaiah, S. B., Allen, B., Forest, C. R., & Boyden, E. S. (2017). Closed-Loop Real-Time Imaging Enables Fully Automated Cell-Targeted Patch-Clamp Neural Recording In Vivo. *Neuron*. <https://doi.org/10.1016/j.neuron.2017.08.011>
- Takahashi, Y., Shevchuk, A. I., Novak, P., Murakami, Y., Shiku, H., Korchev, Y. E., & Matsue, T. (2010). Simultaneous Noncontact Topography and Electrochemical Imaging by SECM/SICM Featuring Ion Current Feedback Regulation. *Journal of the American Chemical Society*, 132(29), 10118–10126. <https://doi.org/10.1021/ja1029478>
- The Human Brain Project. (2012). The Human Brain Project: a report to the European Commission. *The HBP-PS Consortium*.
- Tognoni, E., Baschieri, P., Ascoli, C., Pellegrini, M., & Pellegrino, M. (2016). Characterization of tip size and geometry of the pipettes used in scanning ion conductance microscopy. *Micron*, 83, 11–18. <https://doi.org/10.1016/J.MICRON.2016.01.002>
- Tononi, G. (2008). Consciousness as integrated information: A provisional manifesto. *Biological Bulletin*. <https://doi.org/10.2307/25470707>
- Vähäsöyrinki, M., Tuukkanen, T., Sorvoja, H., & Pudas, M. (2009). A minimally invasive displacement sensor for measuring brain micromotion in 3D with nanometer scale

- resolution. *Journal of Neuroscience Methods*, 180(2), 290–295. <https://doi.org/10.1016/J.JNEUMETH.2009.04.004>
- Vélez-Fort, M., Rousseau, C. V., Niedworok, C. J., Wickersham, I. R., Rancz, E. A., Brown, A. P. Y., ... Margrie, T. W. (2014). The Stimulus Selectivity and Connectivity of Layer Six Principal Cells Reveals Cortical Microcircuits Underlying Visual Processing. *Neuron*, 83(6), 1431–1443. <https://doi.org/10.1016/j.neuron.2014.08.001>
- Wang, Q., Webber, R. M., & Stanley, G. B. (2010). Thalamic synchrony and the adaptive gating of information flow to cortex. *Nature Neuroscience*, 13(12), 1534–1541. <https://doi.org/10.1038/nn.2670>
- Wang, X., Vaingankar, V., Sanchez, C. S., Sommer, F. T., & Hirsch, J. A. (2011). Thalamic interneurons and relay cells use complementary synaptic mechanisms for visual processing. *Nature Neuroscience*, 14(2), 224–231. <https://doi.org/10.1038/nn.2707>
- Wang, X., Wei, Y., Vaingankar, V., Wang, Q., Koepsell, K., Sommer, F. T., & Hirsch, J. A. (2007). Feedforward excitation and inhibition evoke dual modes of firing in the cat's visual thalamus during naturalistic viewing. *Neuron*, 55(3), 465–478. <https://doi.org/10.1016/j.neuron.2007.06.039>
- Wang, X., Yu, G., Hou, X., Zhou, J., Yang, B., & Zhang, L. (2010). Rebound bursts in GABAergic neurons of the thalamic reticular nucleus in postnatal mice. Retrieved from <http://search.proquest.com/openview/8ecc89b28bf369dea2bd2fd3a0adf252/1?pq-origsite=gscholar&cbl=29462>
- Wetterstrand, K. (2017). DNA Sequencing Costs: Data from the NHGRI Genome Sequencing Program (GSP).
- Whitmire, C. J., Waiblinger, C., Schwarz, C., & Stanley, G. B. (2016). Information Coding through Adaptive Gating of Synchronized Thalamic Bursting. *Cell Reports*, 14(4), 795–807. <https://doi.org/10.1016/j.celrep.2015.12.068>
- Wu 吴秋雨, Q., Kolb, I., Callahan, B. M., Su, Z., Stoy, W., Kodandaramaiah, S. B., ... Chubykin, A. A. (2016). Integration of autopatching with automated pipette and cell detection *in vitro*. *Journal of Neurophysiology*, 116(4), 1564–1578. <https://doi.org/10.1152/jn.00386.2016>
- Ylinen, A., Soltész, I., Bragin, A., Penttonen, M., Sik, A., & Buzsáki, G. (1995). Intracellular correlates of hippocampal theta rhythm in identified pyramidal cells, granule cells, and basket cells. *Hippocampus*. <https://doi.org/10.1002/hipo.450050110>
- Yu, Y.-Q., Xiong, Y., Chan, Y.-S., & He, J. (2004a). Corticofugal gating of auditory information in the thalamus: an *in vivo* intracellular recording study. *The Journal of Neuroscience: The Official Journal of the Society for Neuroscience*, 24(12), 3060–3069. <https://doi.org/10.1523/JNEUROSCI.4897-03.2004>



Yu, Y.-Q., Xiong, Y., Chan, Y.-S., & He, J. (2004b). Corticofugal Gating of Auditory Information in the Thalamus: An In Vivo Intracellular Recording Study. *Journal of Neuroscience*, 24(12), 3060–3069. <https://doi.org/10.1523/JNEUROSCI.4897-03.2004>